International Journal for Multiscale Computational Engineering, 19(3):1–80 (2021)

MULTISCALE MODELING FOR THE SCIENCE AND ENGINEERING OF MATERIALS

Jing Bi,[1] Felix Hanke,[2] Huidi Ji,[1] Ross McLendon,[1] Stephen Todd,[2]
Tod Dalrymple,[3] Rafael Salazar-Tio,[4] Martin Persson,[2]
Eugenio Chiavaccini,[5] James Wescott,[2] Stefan Dietz,[6] Martin Schulze,[6]
Johannes Schwöbel,[7] Jiang Yao,[1] Victor Milman,[2] Pierre Yves Mechin,[8]
Chris Wohlever,[1] Juan Hurtado,[1] & Victor Oancea[1,]*

[1]*Dassault Systèmes, Johnston, Rhode Island, USA*
[2]*Dassault Systèmes, Cambridge, United Kingdom*
[3]*Dassault Systèmes, Dearborn, Michigan, USA*
[4]*Dassault Systèmes, San Francisco, California, USA*
[5]*Dassault Systèmes, Darmstadt, Germany*
[6]*Dassault Systèmes, Gilching, Germany*
[7]*Dassault Systèmes, Cologne, Germany*
[8]*Dassault Systèmes, Vélizy-Villacoublay, France*

*Address all correspondence to: Victor Oancea, 1301 Atwood Ave #101w, Johnston, RI 02919, USA,
E-mail: Victor.OANCEA@3ds.com

Original Manuscript Submitted: 8/13/2021; Final Draft Received: 8/14/2021

Material discovery and development drives innovation and is a key component for almost all cutting edge technologies today. With progress in computing power and numerical methods, multiscale modeling has been a rapidly growing requirement in the science and engineering of materials. However, unresolved challenges in true multiscale modeling have thus far prevented engineers and scientists from realizing its full potential and, as a result, its success in production applications is not widespread. Particularly difficult challenges to multiscale simulations are the vastly different physics at different scales among different materials manufactured with different procedures and used in different applications with different performance indicators. To help address these challenges Dassault Systèmes has brought together the power of multiple software brands to combine the expertise in multiphysics simulations from quantum and molecular to continuum and system scale with a purpose to promote the production usage of multiscale modeling to design, develop, and validate sustainable and programmable materials. In this paper, the key multiscale modeling and simulation technologies from Dassault Systèmes will be introduced with a focus on the realistic industrial applications via an end-to-end digital thread on the ***3D****EXPERIENCE Platform. Our goal is to provide a fundamental and general framework to allow engineers to construct microscale models, and deduce the macroscale laws and the constitutive relations by proper homogenization, with seamless integration to our native material modeling capabilities, for quantitative, rigorous analysis of the overall response and failure modes of advanced multiphase materials.*

KEY WORDS: *multiscale, mean field homogenization, representative volume element, FE^2, micromechanics informed, coarse graining, phase field, periodic boundary condition*

1. INTRODUCTION

Over the past 50 years, tremendous progress had been made by the scientific and engineering communities in the field of computer simulation of physical systems at the macro, or visible, scale. This progress is due to a number

1543–1649/21/$35.00 © 2021 by Begell House, Inc. www.begellhouse.com

of factors including advancements in our understanding of the underlying physics, improved modeling techniques, development of robust numerical methods for solving relevant field equations, and of course the exponential increase in computing power and memory. As a result, the available commercial software tools for product design simulation based upon the finite element method and computational fluid dynamics are well developed for many industries.

Part of the value of virtualization of structures is to reduce the time and cost associated with physical testing, but there is a far greater value in the insight that engineers can gain into how a component or subsystem behaves (upper right of Fig. 1). For the simulation of structures at the macroscale (FEA/FEM) there have been decades of development of phenomenological material modeling, based on testing and observation of material behavior.

Over roughly the same time period, the field of computational chemistry has been developed to study materials at their most basic electronic, atomistic, and molecular levels (lower left of Fig. 1). From an industrial perspective, the software tools of computational chemistry can help the chemist and material scientist gain insight into fundamental material behavior in an effort to design and create new and improved materials. The related field of computational metallurgy helps the metallurgist and material scientist develop better metal alloys. A common idea in metallurgy and materials science is understanding the *process-structure-property* (PSP) relationship. It is fairly easy to grasp that the manufacturing process of a metal alloy affects its microstructure (grain size, etc.) and this microstructure will affect the overall mechanical properties (stress-strain curve, yielding, failure, etc.).

Traditionally, these two domains of engineering (product design) and materials science (material design) have worked independently, communicating needs/requirements and availabilities. These two domains work at extremely different length and time scales. Significant advances have been made as the engineering domain looked at smaller scales in order to better understand the microstructure of materials and the materials science domain looked at larger scales to better understand a material's macro behavior. In recent years, the concept of ICME, integrated computational materials engineering, has gained considerable traction, especially at the research level and within academic programs. The goal of ICME is to advance the computational knowledge and infrastructure so that scientists and engineers can work together, across all length and time scales to develop better materials and thus better products. In the USA, the Materials Genome Initiative was launched in 2011 to speed the discovery and use of advanced materials across industries. This is just one example of the stated importance of advanced materials, all the way from chemistry and materials science to their engineering use in design.

At Dassault Systèmes, we have brought together brands and technologies that play key roles in product design, CATIA; simulation for design, SIMULIA; and computational chemistry and materials science, BIOVIA. The Dassault Systèmes vision is to bring together all the required physics of simulation, across all scales, for use in innovation in product, nature, and life. Dassault Systèmes is uniquely positioned to deliver these technologies in a single-business environment, the **3D**EXPERIENCE Platform. By working within a single, integrated platform, we can integrate the

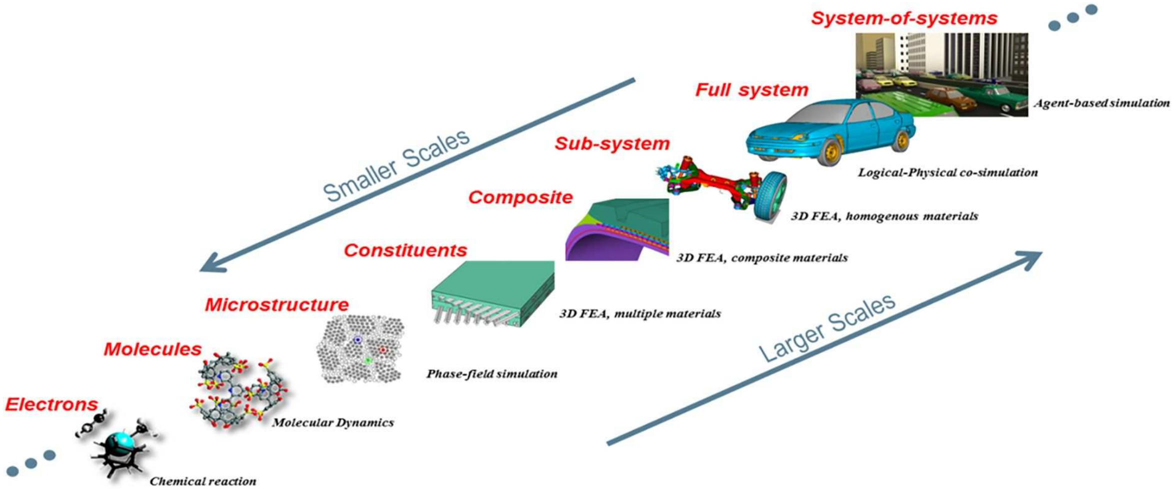

FIG. 1: Computational modeling or simulation at various scales: a tire/auto example

tools that materials scientists use to develop new and improved materials, along with all the tools that engineering communities use to develop new and improved products. As depicted in Fig. 2, the goal is to bring together and integrate all of the technologies for the creation of new materials and the innovation of new products based on advanced material modeling.

2. MATERIAL MULTISCALE METHODS IN DASSAULT SYSTÈMES

The virtual design and simulation is done according to modeling assumptions needed to reduce the complexity of the system. These assumptions aim to solve for different levels of detail of an equivalent system. In the case of material, significantly different levels of detail may be obtained depending on the modeling assumption: a metallic material can be assumed as a uniform homogenized volume with a global behavior measured from physical tests, or as an aggregate of microstructural constituents (grains, particles, combination of multiple phases), with local constituent behavior tested physically or calibrated numerically. This lower scale modeling provides a higher level of detail (for example, the ability to identify which component is leading first to plasticity or failure). To ensure the lower scale model is representative of the global behavior, the right volume must be considered and defined. Such volume is named the representative volume element (RVE). RVE depends on the microstructure of the material or the size of the substructure to consider. As an example, in the case of composite materials, dependent on mechanical properties of the fiber-matrix combination, including a greater number of fibers in the volume will generate a more representative response of the aggregate. Therefore minimum RVE size needs to be determined to ensure the computed properties are representative for macroscale response.

RVE in itself corresponds to the smallest size scale meaningful at continuum scales. Its size, however, is gigantic in comparison to the atomistic scale which is used for molecular modeling in BIOVIA applications. The two scales can be connected at the level of microstructure description: phase-field modeling is used in BIOVIA tools to simulate microstructure based on the fundamental properties of the material (mainly thermodynamic properties and elastic coefficients). Such material characteristics are inferred from atomistic simulations using a selection of tools from the molecular modeling toolbox. The choice of simulation techniques is determined by a number of factors: which properties are of interest, what are the accuracy requirements, what are the computational resources available.

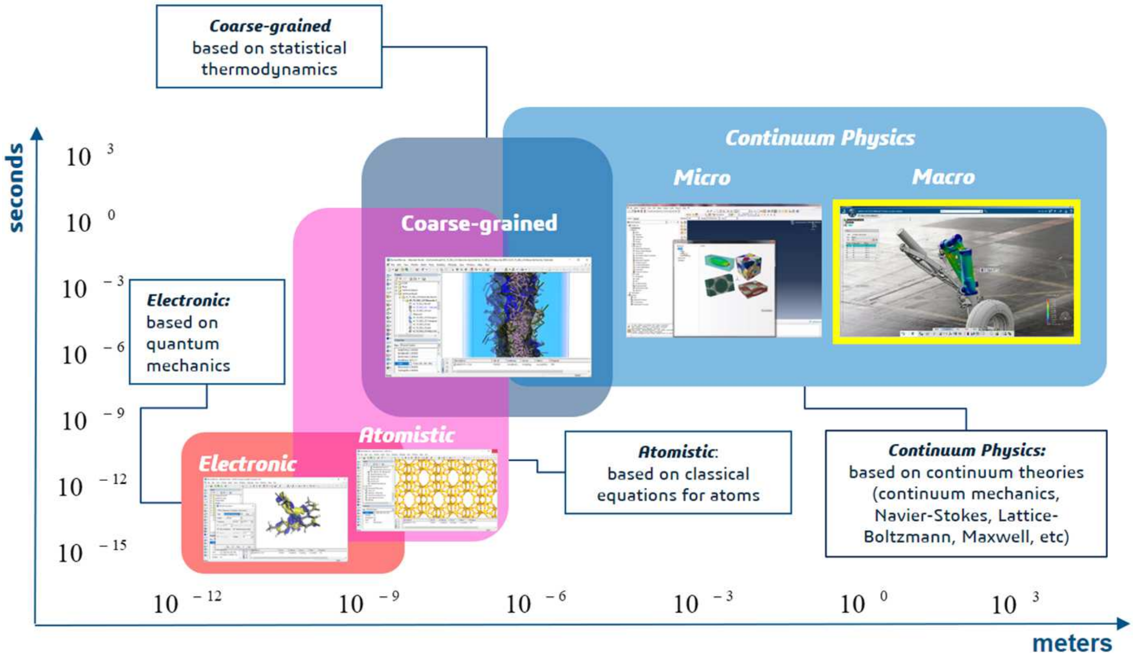
Coarse-grained based on statistical thermodynamics
seconds
10^{3}
10^{0}
10^{-3}
10^{-6}
10^{-9}
10^{-12}
10^{-15}
Electronic: based on quantum mechanics
Continuum Physics
Micro
Macro
Coarse-grained
Atomistic
Electronic
Atomistic: based on classical equations for atoms
Continuum Physics: based on continuum theories (continuum mechanics, Navier-Stokes, Lattice-Boltzmann, Maxwell, etc)
10^{-12}
10^{-9}
10^{-6}
10^{-3}
10^{0}
10^{3}
meters

FIG. 2: The science and engineering of material from quantum scale to system scale

The most detailed representation of materials is based on a quantum mechanical description of the ensemble of interacting electrons and ions. This is the necessary level of theory when material properties of interest are determined by electrons in crystal: e.g., optical properties, semiconductor properties, and electron transfer reactions. Computational effort required for quantum mechanical simulations typically scales with the number of atoms as N^3, or at best $N^2 \log N$. Rare implementations that offer linear scaling have a very high crossover point relative to the typical N^3 codes, so realistic applications of these techniques are limited by hundreds, at most thousands, of atoms. This translates into volume elements with linear dimensions of a few nanometers, far below the RVE size scale. Similarly simulations of time-dependent processes using quantum mechanics do not cover more than 10–100 ps.

The size of the system and simulation time can be increased by orders of magnitude by using a potentially less accurate description of interatomic interactions. This is implemented in classical simulations where atoms are treated as particles that interact using predefined force fields; force field parameters are often derived so as to reproduce properties computed with quantum mechanics. The next level of abstraction brings us to mesoscale modeling, where atoms are no longer treated individually but instead are grouped into interacting beads with their own force fields.

The subsections below give a brief overview of the technologies/software products available at the various scales in Dassault Systèmes.

2.1 Quantum Mechanics: Density Functional Theory (DFT) Descriptions of Atoms and Electrons

The prediction of molecular orbitals and electronic states of matter is the smallest-scale problem that can be addressed in a multiscale modeling framework for engineering applications. The goal of such calculations in a multiscale framework is to analyze intrinsic material behavior such as crystal elasticity, the in-depth description of molecules in their surroundings, or chemical reactions.

In small molecules, electronic orbitals typically extend over the entire molecule. In metals they can be completely delocalized waves. In both cases we need to model the electron's behavior by solving an approximation to the quantum mechanical Schrödinger equation. As additional complication, the Pauli exclusion principle requires that no two electrons can occupy the same quantum state, which means that all electrons in a material are aware of each other. For macroscopic crystals with $\sim 10^{23}$ atoms, it is not possible to treat each electron individually.

This challenge is solved by noting that one can describe all electrons in terms of their total density (Hohenberg and Kohn, 1964). The corresponding Kohn-Sham (KS) equations (1965) provide a practical way to solve for the density and are the foundation of the density functional theory (DFT) approach to electronic structure theory. We do not cover DFT in depth, but aim to give a high level overview of what calculations look like from a practitioner's point of view and introduce the basic terminology required to understand multiscale simulation workflows. Readers interested in having a deeper understanding of electronic structure theory should consult some of the excellent texts, for example, Martin (2012). The Swiss army knife for DFT calculations is Materials Studio, which provides access to a number of different implementations—each with their own set of advantages and application areas.

The main approximation in DFT introduced in the KS equation is that the correct description of the electron-electron interaction requires a potential that can account for the exchange effects (e.g., the Pauli principle) and electronic correlation. An entire hierarchy of these *exchange correlation (XC) functionals* has been developed, as summarized by Burke (2012). This topic remains an active area of research. The suitable specification of the XC functional is an essential ingredient in a DFT calculation.

In solid systems, we typically assume that crystals are infinite and symmetric and apply periodic boundary conditions. Depending on the lattice symmetry, we might get away with modeling only a few atoms per asymmetric unit, also called the *unit cell*. The price for this change in perspective is that we need to sample the entire Fourier space of the crystal lattice waves (called the Brillouin zone, sometimes also *k*-space), and we need to solve the KS equation at each of the points. The *k-space sampling* is a numerical choice, which should be converged explicitly and needs specification in any periodic DFT calculation.

The third major ingredient is the choice of the basis on which to represent the Hilbert space accessible by the electrons. Implicit in the choice of basis set is a selection of an implementation of DFT. A few common choices for basis sets, their advantages, and their respective implementations in the BIOVIA software portfolio are the following:

1. Plane waves, as implemented in CASTEP (Clark et al., 2005). Here the electronic density is represented by Fourier waves with a specified *cutoff energy*, which determines the quality of the basis. Plane waves are ideally suited for simulating periodic lattices of materials such as metals, semiconductors, and other crystals. They are frequently used to study surfaces and heterogeneous catalysts.
2. Numeric atomic orbitals are centered on nuclear positions and describe the electrons in similar terms to the single-atom *s*, *p*, *d* atoms that are well known in high school chemistry. They are well suited to study molecules, larger crystals, and reaction rates, and are used in heterogeneous catalysis applications. The DMol^3 module (Delley, 1990, 2000) in Materials Studio provides a robust and scalable implementation of numeric atomic orbitals.
3. Gaussian basis functions are also centered on atoms and model electrons as superpositions of analytic functions. This implementation is suitable for the highly accurate calculation of molecular and solvation properties, as a lot of integrations involving the Gaussian orbitals can be achieved analytically. Gaussian basis sets are implemented in TURBOMOLE (TURBOMOLE, 2020; Balasubramani et al., 2020).
4. Nonorthogonal generalized Wannier functions (NGWF) provide a way to overcome the unfavorable scaling with the system size that is implicit in the basis set choices discussed above (Skylaris et al., 2002). Their implementation in the ONETEP module (Skylaris et al., 2002) in Materials Studio is particularly suited for studying the electronic structure in systems of many thousands of atoms, which can easily become out of reach for commonly available computational resources in other methods.

A final choice, often made together with the basis set, is a selection of a suitable *pseudopotential*. These are often used to describe the core electrons of heavier atoms, thereby reducing the computational cost.

To sum up, a practitioner needs to focus on three things: (1) a sufficient theoretical description of the electrons via a suitable exchange correlation functional and a representation of nuclear core electrons, (2) a suitable basis to describe the electrons at a single *k*-point, and (3) sufficient *k*-space sampling for periodic crystals. The pseudopotentials and basis convergence depend on the actual implementation of DFT, with multiple different options available for different purposes.

As described so far, DFT can compute the total energy of an atomic system with known nuclear positions and unit cell. Forces on the nuclei are available and are used in semiclassical equations of motion where electrons are treated quantum mechanically and nuclei are point particles. Following the forces to find energy minima and saddle points enables the simulation of stable structures and reactions, respectively. A large number of property calculations are possible to understand materials and drive product design decisions. These include basic thermodynamic properties, molecular and lattice vibrations, elastic coefficients, solvation properties, and chemical reaction rates, as well as a wide variety of spectroscopic data. Materials Studio provides a straightforward tool to run and manage DFT calculations across the entire spectrum of materials science applications, to analyze them correctly, and to build workflows on top of individual calculations.

In practice, a DFT calculation proceeds as follows. First, set up the molecule or lattice with atoms in approximately the correct position. Next, select an implementation of DFT, and suitable computational settings as described above. The calculation will proceed by self-consistently determining the electronic structure of each set of lattice coordinates and then typically follow the atomic forces to find the point where the energy is minimized. This structure is the basis for computing physical properties as discussed above. One can build workflows by successive calculations on different lattices and molecules in a high throughput fashion, for example, to obtain phase diagrams directly from quantum mechanical calculations.

2.2 Molecular Dynamics

While being able to predict the electronic states of matter gives a very accurate representation of a molecule or of a crystal, the limitations in terms of system size require alternative methods that can still capture the chemistry of a system. Simulations based on classical potentials remove the complexity of interactions of electronic states and replace them by a model where the atoms are treated as spheres. Atoms can interact with other atoms by a bonded, or valence term, if they are connected, or a nonbonded interaction, if they are not directly connected, or a mixture of the two interactions. By simplifying the interaction between atoms, classical potentials enable the simulation of much larger system sizes, up to millions of atoms, thus incorporating more chemical complexity than is possible with DFT. Through molecular dynamics, the use of classical potentials also enables the simulation of longer time scales than DFT and the incorporation of the effect of temperature into a simulation.

In order to predict the properties of a system using classical potentials, a set of parameters which describe how the atoms interact is required. This parameter set is known as a force field and there are many different force fields available in the literature. Generally, force fields are developed to model a specific problem. For example, if a user wanted to develop a new drug, they might use the CHARMm (Huang and MacKerell, 2013) force field. The CHARMm force field includes different elements for organic molecules but has been parameterized focusing on ligand-protein interactions and cannot be used to model a metal alloy where a user may choose a very specific force field that has been parameterized for the elements of interest.

The interactions between atoms of the same element are also dependent on the local environment of the atom. For example, a carbon atom in a hydrocarbon chain will not have the same bond length distance to an adjacent carbon as it would if it was attached to a benzene ring. To solve this, force field types are used to differentiate between the same elements in different chemical environments. Force fields for modeling a wide range of systems can be very large and complex and extending them requires significant effort. The COMPASS III force field (Akkermans et al., 2020), provided in Materials Studio, uses equivalencing rules to minimize the number of force field types but still contains 281 different types.

Force fields also vary in terms of the interactions that are included. COMPASS III is known as a class 2 force field and includes simple valence terms to represent bond stretches, angles, torsions, and advanced cross terms to capture relationships between the simple valence terms. It also includes explicit terms for nonbonded interactions, capturing van der Waals and electrostatic forces.

A force field on its own is just a set of parameters and must be coupled with another method to enable investigation of material behavior. The most popular methods are simple energy calculations, used to evaluate the energy of a system; molecular dynamics, used to model the temporal evolution of a molecule or crystal; or Monte Carlo methods, used to calculate specific properties or build models of materials (Akkermans et al., 2013).

In Materials Studio, the two main solvers that use classical potentials for molecular dynamics are Forcite and GULP (Gale and Rohl, 2003). Forcite, coupled with the COMPASS III force field, is used to study properties of a wide range of condensed phase systems. For example, COMPASS III has been applied to predict properties of polymers and resins such as glass-transition temperature, coefficient of thermal expansion, diffusion of penetrant molecules, and mechanical properties. GULP includes many specialized force fields and is focused on the prediction of properties of solid state materials. Classical potentials are also used in several Monte Carlo based solvers in Materials Studio. For a review of these, please see Akkermans et al. (2013).

In a molecular dynamics simulation, different ensembles are used depending on the type of simulation required. The microcanonical, or NVE, ensemble, where system volume and energy are conserved, can be used to calculate properties where thermal fluctuations are important, such as diffusivity. The canonical, or NVT, ensemble where volume and temperature are conserved by use of a thermostat is often used during property prediction. The isobaric-isothermal, or NPT, ensemble, where pressure and temperature are conserved by use of both a barostat and thermostat closely resembles experimental conditions. In reality, prediction of a property such as yield stress requires numerous chained simulations with different ensembles. Initially, the system is equilibrated using a long NPT dynamics simulation. This is followed by multiple cycles of NVT (to relax after a strain has been applied), NPT (to equilibrate to the new density), and production NVT (to calculate the new stress). In BIOVIA software, these complex workflows are automated in the BIOVIA Materials Studio Collection in BIOVIA Pipeline Pilot (2021), a workflow automation and data science tool.

2.3 Coarse-Grain Molecular Dynamics

Access to today’s high performance super computers allows simulations using representation of matter at the explicit atom level to be performed for potentially millions of atoms. In fact, Jung et al. (2019) recently reported the first billion atom simulation utilizing over 100,000 cores. Even at more moderate atom counts there are challenges with the volumes of data produced, for visualization and analysis, and systems are not always suitable. For instance, in simulation of dilute solvated systems it would make little sense to spend so much effort in the calculation of many explicit solvent molecules. For the study of soft matter condensed phases such as polymer phase separation or surfactant self-assembly, representation at a coarser level is a pragmatic choice that provides convenient access to insights and property predictions at scales of 1–1000 nm with smaller demands on the computer. This is often referred to as the mesoscale regime (though the term mesoscale is also used within engineering scales to mean something much larger, which can cause confusion).

Coarse-graining approaches have long been used to simplify and reduce computational requirements of molecular dynamics simulations. Early representations of polymers often used united atoms (UA), since the fluctuations of hydrogen atoms are of secondary interest and are neglected. As well as substantially reducing the number of particles in the simulation box, the time steps used to progress atom positions can usually be doubled from 1 to 2 fs. Despite the approximation UA simulations have been reasonably successful in reproducing nondynamical properties (Chen et al., 2006) when compared to atomistic models.

Another strategy for simulation at the mesoscale is to use a continuous field representation describing the spatial distribution of species. Materials Studio MesoDyn employs dynamic density functional theory to evolve the fields with constraints that capture the random chain nature of polymers and drivers of phase separation between unlike chemical species. MesoDyn is particularly suited for exploring ordered phases in block copolymers and a connection with Flory-Huggins polymer theory is key in connecting these simulations to experimental characterization of the component materials. Groot and Warren (1997) also identified Chi parameters as a simple route to parameterizing another coarse-grained approach, Dissipative Particle Dynamics (DPD).

DPD is a soft-particle based approach with overlapping discrete interaction sites, associated with the position of particles, or beads, representing groups of atoms in the atomistic system. A DPD bead can also be interpreted as a region of fluid rather than a distinct particle and, as such, DPD beads can overlap and indeed pass through each other. Consequently, mixtures of several components show very fast reorganization to the thermodynamic equilibrium configuration on the nanometer scale compared to all-atom or united atom simulations. However, the trade-off for fast structural equilibration disconnects from physical kinetics, and this limits the properties that DPD can be expected to reproduce reasonably.

An increasingly popular approach is a compromise between the UA and DPD methods, known as coarse-grained molecular dynamics (CG-MD) which retains a relatively coarse representation (several atoms to a bead). CG-MD uses force fields (usually including Lennard-Jones, Coulomb, bonds, angle terms, and sometimes dihedrals). Several specific parameter sets for treating material types have emerged but undoubtedly one of the most popular has been the approach of Marrink et al. (2004), known as the Martini force field. Martini uses a reasonably small set of interaction sites to represent a full range of chemistry (polar, intermediately polar, apolar, and charged species with subtypes for electron donors, acceptors, both, or none) and it has enabled a wide range of materials to be studied with a limited amount of time-consuming re-parameterization. Parameterization of the beads is primarily achieved through matching with experimental octanol/water and alkane/water partitioning free energy values. This successfully provides the necessary driving forces for aggregation, partitioning, and self-assembly processes. Though initially derived for biomolecular simulations, Martini has been shown to be transferable to a diverse set of systems in soft materials science. Nevertheless, as the materials science applications have grown, the introduction of special cases and terms to provide better agreement with experimental data has been needed. The authors have recently taken the opportunity to revisit the parameterization of the interaction matrix and have introduced Martini3 (Souza et al., 2021). Martini3 is expected to better capture relative miscibility, self-assembly, and aggregation propensities, and is set to become even more widely adopted. While CG-MD is increasing in popularity, it is worth pointing out that in common with other mesoscale methods dynamic properties are not so easily recovered. This is explained in terms of a smoothing of the potential energy surfaces in a coarse-grained representation allowing molecules to move more easily past each other. In the four atoms to one bead representation of the Martini approach, an approximate acceleration of bead dynamics of four times compared to all-atom simulations is observed due to this effect. In fact, this increases the time scales accessible to a CG-MD simulation, but also makes it more difficult to make predictions for properties such as diffusivity and viscosity.

2.4 Phase Field

Theoretical modeling and prediction of microstructures in hard materials is dominated by the phase-field method. Phase-field models, sometimes also called diffuse interface models, are characterized by the use of a diffuse interface between different phase regions. The phase-field variable or state function which distinguishes between the different phase regions is made to vary rapidly but continuously, avoiding any discontinuities. The system can then be solved as a set of partial differential equations avoiding explicit treatment of the boundary conditions at the interface (Fig. 3). The BIOVIA multiphase-field tools are based on the OpenPhase Core library provided by OpenPhase (OpenPhase, 2021).

In the multiphase-field implementation each grain is attributed its own phase-field variable ϕ_m. The governing equations for the evolution of the phase fields and the concentration are given below:

$$\dot{\phi}_k = \sum_{l=1}^{N} \frac{\mu_{kl}}{N} \left\{ \sum_{m=1}^{N} \left[\sigma_{lm} - \sigma_{km}\right] I_m + \frac{\pi^2}{8\eta} h' \Delta g_{kl} \right\}, \tag{1}$$

$$I_m = \nabla^2 \phi + \frac{\pi^2}{\eta^2} \phi_m, \tag{2}$$

$$\dot{c} = \nabla \left\{ \sum_{k=1}^{N} \phi_k \left[\boldsymbol{D}_k \nabla c_k\right] + \sum_{k,l=1}^{N} j_{kl} \right\}. \tag{3}$$

Here k, l, and m are the phase-field indexes, μ_{kl} is the interface mobility, and N is the number of nonvanishing phase-field parameters at a given point. η is the interface thickness, h is the shape function related to the phase-field contour, and Δg_{kl} is the thermodynamic driving force. I is the generalized curvature term. $\boldsymbol{D}_k$ is the diffusion matrix in phase k, and j_{kl} is the anti-trapping current. For further details about the method, see Steinbach and Apel (2006).

Other effects such as latent heat, heat diffusion, and mechanical strain can be included in the simulations. The time evolution of the problem is solved by integrating the set of partial differential equations on a regular grid starting from a defined starting condition and including appropriate boundary conditions. Calculations can be performed using a 2D or 3D grid. Naturally the 2D setup allows for larger lateral size and a longer simulated time range. To speed up the calculations the code is parallelized using OpenMP.

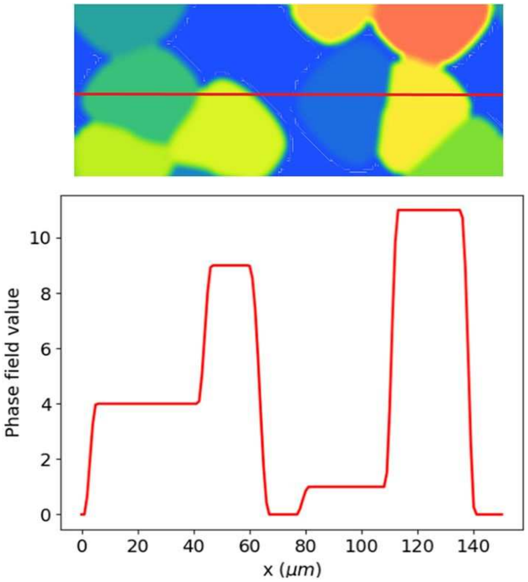

FIG. 3: Example plot of phase-field values along the red horizontal line in the above simulated microstructure

Grains can be specified as part of the initial starting condition or nucleated from a set of nucleation seeds during the cooling of the system. Phase-field simulations require a large set of input parameters. Some of the parameters can be found in the literature or material databases, while others such as interface energy, interface mobility, and diffusion can be harder to find or are found to have large errors attached to them. For qualitative or phenomenological studies accurate values for the latter parameters might not be needed, while if quantitative predictive studies of a specific materials system are desired, accurate values are required; values can sometimes be improved by fitting to known experimental results.

2.5 Solvation Chemistry: COSMO-RS

The conductor-like screening model for realistic solvation (COSMO-RS) is a predictive, generally applicable, and efficient computational model to handle fluid phase properties (Klamt et al., 1998). In short, COSMO-RS combines quantum chemical information with macroscopic thermodynamic properties via an efficient statistical thermodynamics approach. In this context, COSMO-RS might be considered as a multiscale model on its own: solving problems which have important features at both the atomistic scale (quantum chemical properties) and macroscopic scale (thermodynamic properties) at the same time. In several blind prediction challenges and benchmark studies, COSMO-RS has been proven to be one of the most accurate tools for the prediction of the free energies of molecules in solution (Bannan et al., 2016; Zhang et al., 2015), and thus for all equilibrium distribution properties, such as partition coefficients, solubilities, vapor pressures, reaction equilibrium constants, *p*Ka values, phase diagrams, and related properties.

COSMO-RS is a combination of the dielectric continuum solvation model COSMO (Klamt and Schüürmann, 1993) with an efficient statistical thermodynamic model of pairwise molecular surface interactions. For the quantification of the surface interactions, it uses the surface polarization charge densities σ of each solute arising from quantum chemical COSMO calculations. As most important molecular interaction modes, electrostatics and hydrogen bonding are taken into account in this way. The less specific dispersive interactions are described to first order based on element-specific surface energies. The statistical thermodynamics itself is performed using a coupled set of nonlinear equations for the activity coefficients of the surface segments, the so-called COSMOSPACE equations (Klamt et al., 2002). This results in a solvent-specific free energy response function $\mu_S(\sigma)$, called the σ-potential, which gives the chemical potential of a surface segment of polarity σ in a particular solvent. Finally, the chemical potentials of the compounds μ_S^X in a pure or mixed solvent are calculated by summation of the σ-potentials of the surface segments in a compound, and corrected by a combinatorial term.

An extension to the COSMO-RS bulk phase method is the COSMOperm model for the prediction of partition coefficients and permeabilities in complex inhomogeneous systems, e.g., biomembranes (Schwöbel and Klamt, 2019). It uses information about the structure of the system in order to represent it as a layered liquid of varying composition with respect to the COSMO polarization charge densities σ. Free energies of solutes in such a layered liquid system are calculated by sampling over all relevant positions, orientations, and conformations of the solute in this system (Klamt et al., 2008). Biomembrane to water partition coefficients of neutral and ionic species are predicted with an accuracy of about 0.7 logarithmic units (Bittermann et al., 2014) with the inclusion of a membrane potential. Diffusion coefficients are calculated via COSMO-RS based parameters from entropic and enthalpic contributions. More specifically, the entropy is gained by placing the permeant into a specific solvent system—here a membrane layer—which is responsible for the diffusive pattern in a viscous environment. Interactions in the solvent environment provide a resistance opposing diffusive molecular motions via COSMO-RS electrostatic, hydrogen bond, or van der Waals interaction enthalpies.

The extended model COSMOplex allows one to generate and simulate these complex inhomogeneous systems in a fully self-consistent way (Klamt et al., 2019), only requiring COSMO information as input. This method extends the application range to the prediction of micellar structures and critical micelle concentrations, finite loading effects, interfacial tensions, and surface tensions, plus free energies and structures of liquid interfaces, surfaces, and microemulsions.

Generally, statistical thermodynamics COSMO-RS bulk phase calculations are very efficient with typical calculation times of a few seconds, being predictive and mechanistic at the same time because of its quantum chemical fundamentals and physical interaction terms. Similarly, COSMOperm simulations are performed within a few minutes, and self-consistent, iterative COSMOplex calculations within a few hours per CPU core.

The methods COSMO-RS, COSMOperm, and COSMOplex are implemented in the BIOVIA COSMOtherm software (BIOVIA COSMOtherm, 2012). Workflows can be automated via the BIOVIA Solvation Chemistry Collection for BIOVIA Pipeline Pilot.

2.6 Semianalytical Approaches—Mean Field Homogenization

Mean-field homogenization (MFH) is a semianalytical homogenization approach for composite material modeling. It can be used to model composites with one matrix phase and one or multiple inclusion phases with uniform properties for each phase. It is based on Eshelby's solution of a single-inclusion problem and only requires partial information of the microstructure such as inclusion volume fraction, aspect ratio, and orientation. Multiple inclusion shapes are supported such as prolate, oblate, penny, sphere, cylinder, and elliptic cylinder. Custom shapes are normally approximated by multiple families of ellipsoids with different shapes and alignments. Such as in the case of weaves and braids, we use multiple elliptical cylinders to represent the weft and warp. As the name suggests, MFH gives prediction of volume-averaged fields per constituent and the representation of the microstructure is much cruder compared to FE-RVE.

MFH is computationally efficient and can often be used in concurrent nonlinear analyses through a linearization process. MFH can capture complex behaviors in composite materials that otherwise cannot be properly represented by existing phenomenological models. MFH also allows us to explore the material state at the matrix and inclusion level to further understand behaviors leading to damage and failure. It can be used in parts modeled with both solid and shell elements. The fundamentals of MFH are described in Fig. 4.

Alternatively, the FE-RVE computed concentration tensor can be defined by the user to specify customized strain partitioning (Section 2.9.1). In a high volume fraction composite example, MFH give more accurate results using the RVE obtained concentration tensor directly. The RVE-obtained concentration tensor can also be used for modeling microstructure damage. We can obtain different concentration tensors for different damage statuses and define a damage variable-dependent concentration tensor for material failure modeling. Proper formulation and isotropization for homogenization in MFH can be determined and validated with FE-RVE (Section 2.9.1). For example, using isotropic projection to compute the Eshelby tensor gives better results after onset of plasticity in the matrix compared to general isotropization.

The implementation of MFH in structural applications uses total formulation to partition the elastic strain for linear composites and incremental formulation to partition strain increment for nonlinear composites (Ji et al., 2017).

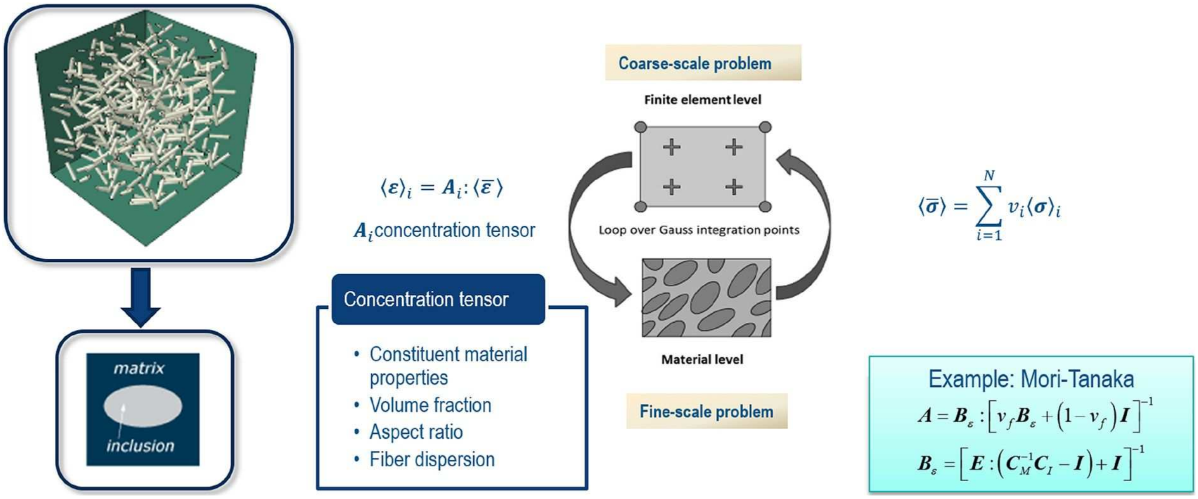
matrix
inclusion
$\langle \boldsymbol{\varepsilon} \rangle_i = \boldsymbol{A}_i : \langle \bar{\boldsymbol{\varepsilon}} \rangle$
$\boldsymbol{A}_i$ concentration tensor
Concentration tensor
• Constituent material properties
• Volume fraction
• Aspect ratio
• Fiber dispersion
Coarse-scale problem
Finite element level
Loop over Gauss integration points
Material level
Fine-scale problem
$\langle \bar{\boldsymbol{\sigma}} \rangle = \sum_{i=1}^{N} v_i \langle \boldsymbol{\sigma} \rangle_i$
Example: Mori-Tanaka
$\boldsymbol{A} = \boldsymbol{B}_\varepsilon : \left[v_f \boldsymbol{B}_\varepsilon + \left(1 - v_f\right) \boldsymbol{I} \right]^{-1}$
$\boldsymbol{B}_\varepsilon = \left[\boldsymbol{E} : \left(\boldsymbol{C}_M^{-1} \boldsymbol{C}_I - \boldsymbol{I} \right) + \boldsymbol{I} \right]^{-1}$

FIG. 4: Fundamentals of mean field homogenization

Although the MFH gives good prediction for composites with linear behavior, for nonlinear composite materials it is often required that the model be validated or calibrated against FE-RVE results or experimental results before it can be used with confidence in a full-size FE analysis. The calibration of constituent properties can be achieved with the calibration app in the **3D**EXPERIENCE Platform with standard test data performed at the composite level.

The implementation of MFH is native to the Abaqus solver, which optimizes the performance. When using MFH we can use most of the material models already implemented in Abaqus as the constituent material. Microlevel damage can be modeled with constituent level damage criteria. Any existing Abaqus damage model can be used to model damage in each constituent. In addition, macrolevel damage can be modeled by querying the constituent material state through a utility included in the Abaqus solver. Damage evolution at the macro level can be captured through homogenization using the damage response at the constituent level. These capabilities allow the user to customize the damage criteria both at the micro and macro level to capture the damage behavior of the composite more accurately.

Another important application of MFH is to model chopped fiber reinforced composites manufactured through the injection molding process. As shown in Fig. 5, fiber orientation calculated with an injection molding simulation can be imported into the subsequent structural analysis and used to specify the microstructure of the composites modeled with MFH.

MFH material is available in the **3D**EXPERIENCE Platform, which allows it to be seamlessly connected to our composite design and manufacture simulation tools, thus providing end-to-end solution.

Next we present two examples with MFH. In the first example a 16-layer laminate under tension is modeled with MFH. In the MFH material model, tensile, compressive, and shear failure criteria are specified in the matrix, and tensile and compressive failure criteria are specified in the fiber. For comparison the Hashin model is also used. Figure 6 shows good agreement between the MFH results and those computed using the Hashin model.

The second example is a boss part manufactured through the injection molding process and subjected to a rigid body load through the middle in the subsequent structural analysis. First, the injection molding analysis is performed with the plastic app in the **3D**EXPERIENCE Platform. Figure 7 shows the fiber orientation results at six different gate locations. Next, a rigid body is driven through the middle of the boss in the structural analysis. MFH material is used to model the chopped fiber reinforced composites. Fiber orientation is imported and used as part of the MFH material specifications. Ductile damage is specified in the matrix material. Figure 8 shows the matrix damage clearly influenced by the manufacturing process (gate locations). We will further discuss the mapping of the fiber orientation in Section 3.4 and the end-to-end solution workflow in Section 7.

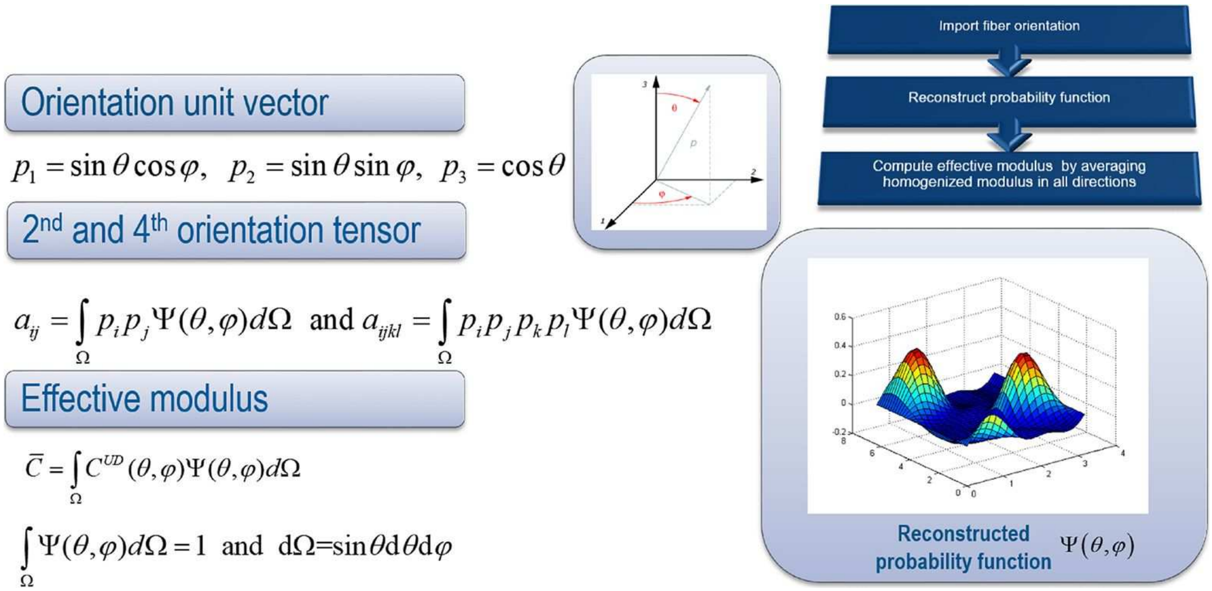
Orientation unit vector
$p_1 = \sin\theta\cos\varphi,\quad p_2 = \sin\theta\sin\varphi,\quad p_3 = \cos\theta$
2nd and 4th orientation tensor
$a_{ij} = \int_\Omega p_i p_j \Psi(\theta,\varphi)d\Omega$ and $a_{ijkl} = \int_\Omega p_i p_j p_k p_l \Psi(\theta,\varphi)d\Omega$
Effective modulus
$\overline{C} = \int_\Omega C^{UD}(\theta,\varphi)\Psi(\theta,\varphi)d\Omega$
$\int_\Omega \Psi(\theta,\varphi)d\Omega = 1$ and $d\Omega = \sin\theta d\theta d\varphi$
3
2
1
θ
φ
p
Import fiber orientation
Reconstruct probability function
Compute effective modulus by averaging homogenized modulus in all directions
0.6
0.4
0.2
0
-0.2
8
6
4
2
0
0
1
2
3
4
Reconstructed probability function $\Psi(\theta,\varphi)$

FIG. 5: Fiber orientation modeling with mean field homogenization

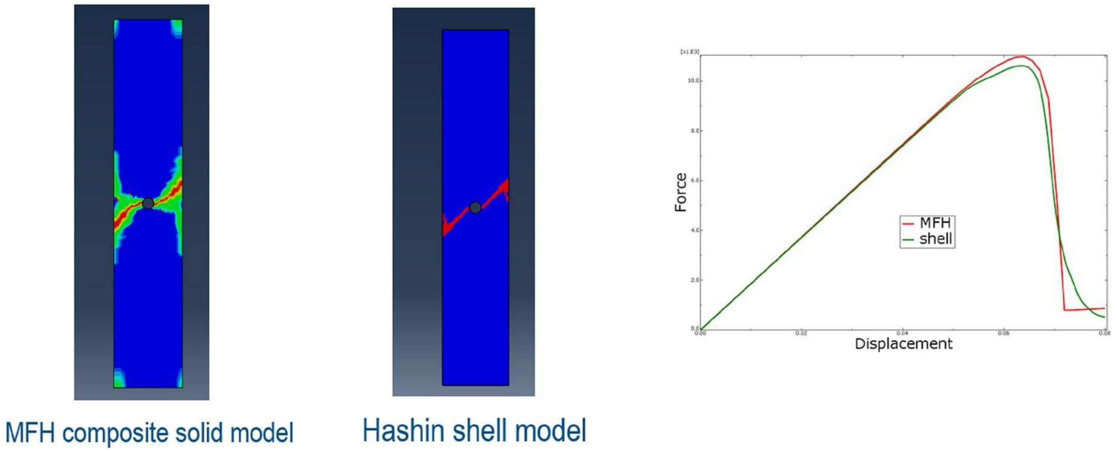

FIG. 6: Comparison of damage results between MFH and Hashin model (left: fiber failure; right: reaction force)

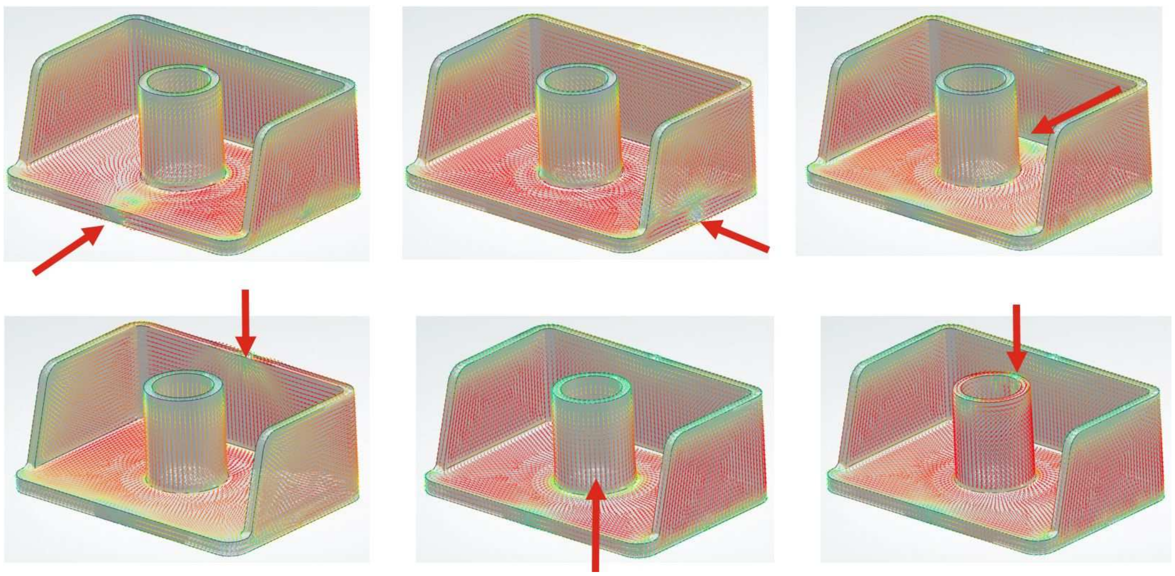

FIG. 7: Fiber orientation computed with different gate locations

2.7 Homogenization Methods for Porous Flow

Porous media (PM) properties related to single-phase and multiphase fluid flow are critical to understanding many macroscopic transport phenomena. Simulated fluid flow properties of interest are (1) permeability, the proportionality constant between single-phase fluid flow rate and pressure gradient; (2) capillary pressure, the sequence of pair values of pressure and saturation (fraction of wetting fluid in pore) obtained when nonwetting/wetting fluid displaces wetting/nonwetting fluid, named drainage/imbibition, respectively; (3) relative permeability, the fraction of the permeability archived for each of the fluids (wetting/nonwetting) when both flow simultaneously at a given saturation. See Fig. 9 for an illustration.

These properties represent effective macroscopic constitutive relationships for flow, which directly depend on the internal pore structure, as illustrated in Fig. 10. No single property model is good for all PM types, thus the need of laboratory measurements or simulation on the actual 3D image of the particular PM. Samples that belong to one PM type will share similar constitutive relationships. This is the reasoning behind PM sampling per rock type in subsurface rock studies.

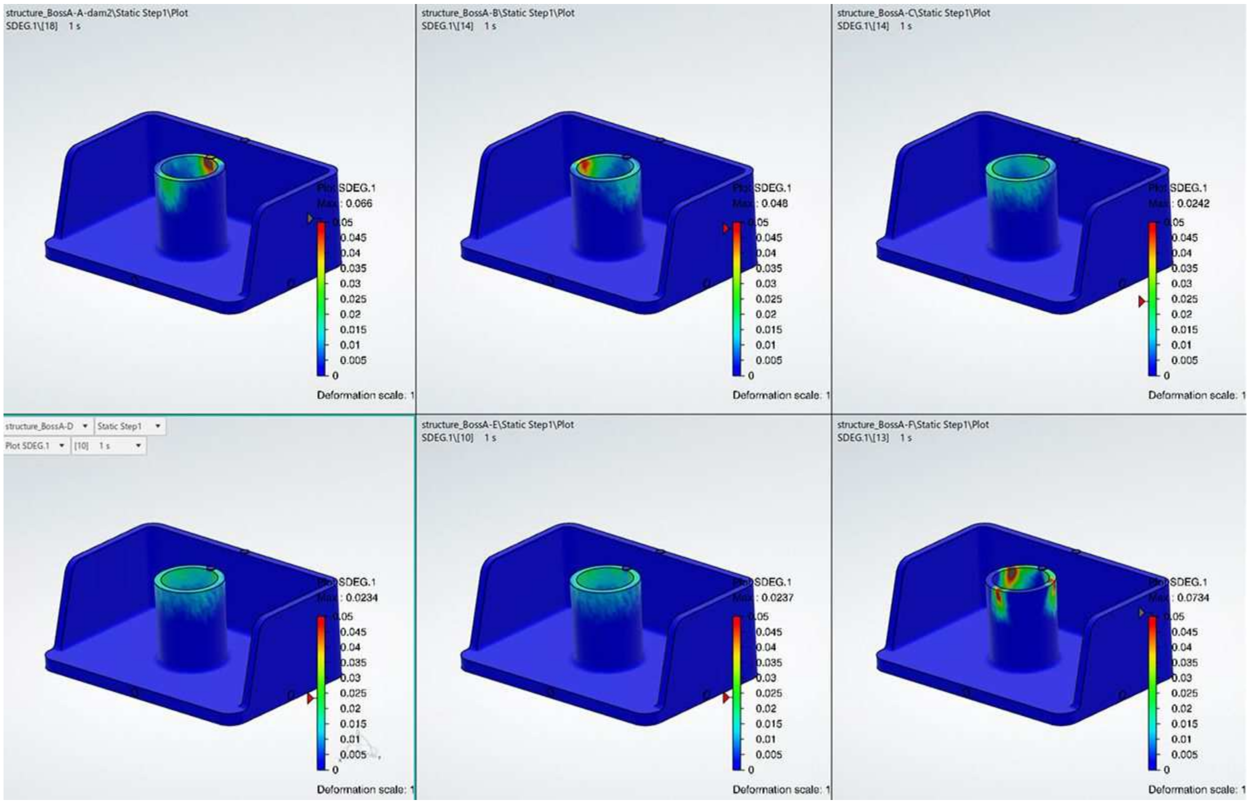
structure_BossA-A-dam2\Static Step1\Plot
SDEG.1\[18] 1 s
Plot SDEG.1
Max : 0.066
0.05
0.045
0.04
0.035
0.03
0.025
0.02
0.015
0.01
0.005
0
Deformation scale: 1
structure_BossA-B\Static Step1\Plot
SDEG.1\[14] 1 s
Plot SDEG.1
Max : 0.048
structure_BossA-C\Static Step1\Plot
SDEG.1\[14] 1 s
Plot SDEG.1
Max : 0.0242
structure_BossA-D
Static Step1
Plot SDEG.1
[10]
1 s
Plot SDEG.1
Max : 0.0234
structure_BossA-E\Static Step1\Plot
SDEG.1\[10] 1 s
Plot SDEG.1
Max : 0.0237
structure_BossA-F\Static Step1\Plot
SDEG.1\[13] 1 s
Plot SDEG.1
Max : 0.0734

FIG. 8: Matrix damage results in the part manufactured with different gate locations

In some of the challenging applications of fluid flow simulation in natural and manufactured materials, the trade-off between model resolution and representative elemental volume is too extreme for a single-scale model to capture the minimum requirements for both aspects. For instance, carbonate reservoir rocks fall into this category, where large pores are connected by microporous structures that have an order of magnitude smaller pores, as illustrated in Fig. 11 (left). In these cases a multiscale digital rock approach is needed. A recently developed lattice Boltzmann method (LBM) extension introduces numerical models for flow in under-resolved PM regions (Otomo et al., 2021). This approach allows for local variability of porosity and saturation in under-resolved PM regions, while fluid forces are applied locally satisfying the constitutive relationships of the corresponding under-resolved PM rock type. Some representative PM rock type samples can be imaged at high resolution, then simulated and constitutive relationships collected systematically into an under-resolved PM library. A segmented image (pore/PM/solid) and a local porosity image can be estimated from an X-ray microtomography 3D image. The standard LBM approach is used in the pore regions, while the new extension is applied to the PM regions. These two images can be sufficient input for a complete description of flow behavior of the PM pixels; assuming that a PM library of constitutive relationship curves is accessible for the LBM solver to fetch the corresponding flow response of each PM pixel given its pair values of PM rock type and subresolution porosity. This multiscale fluid flow workflow is illustrated in Fig. 11.

2.8 Homogenization Methods in Electromagnetic Applications

2.8.1 From Atomic Interaction to Macroscopic Model

Macroscopic volumetric material properties describe how the $\overrightarrow{E}$ and $\overrightarrow{H}$ fields (electromagnetic fields) interact with the $\overrightarrow{D}$ and $\overrightarrow{B}$ fields (electromagnetic displacements). The functional relationship we support is quite general and can be described as

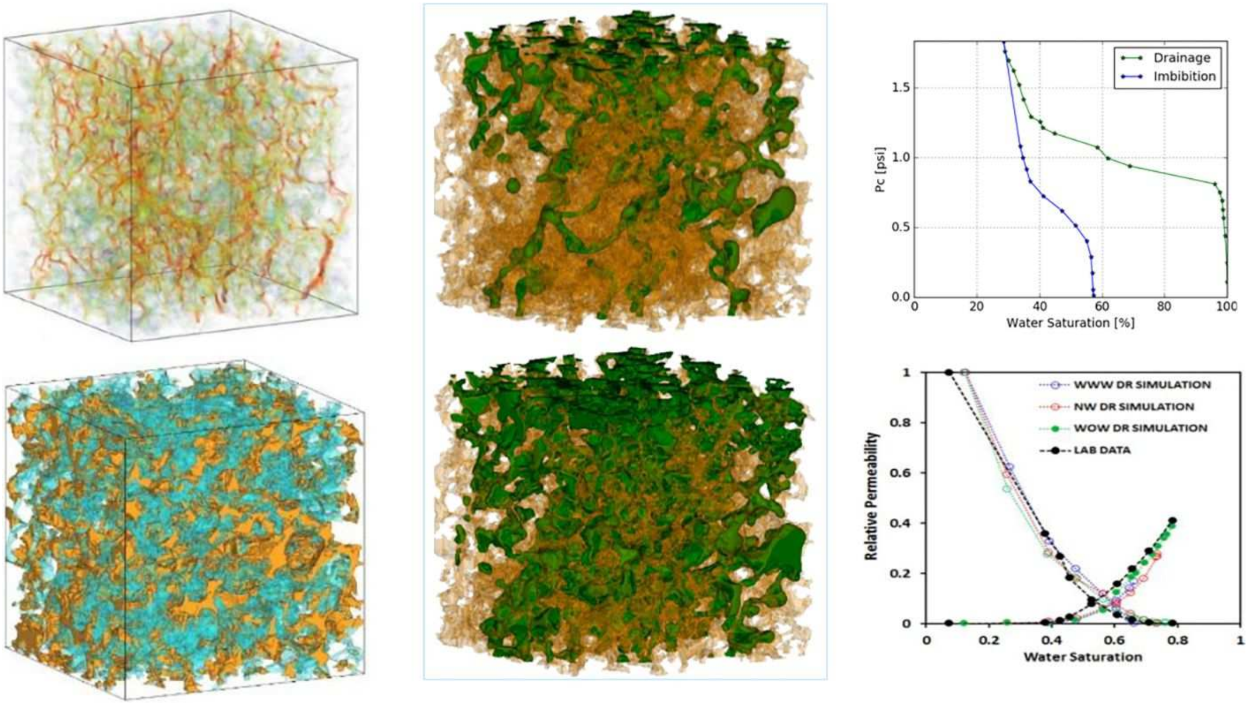

FIG. 9: 3D porous model flow simulations: single-phase velocity path (top left), multiphase wetting/nonwetting fluid saturation (bottom left), and displacement of wetting fluid by nonwetting fluid (middle). Simulated properties: capillary pressure and relative permeability (right).

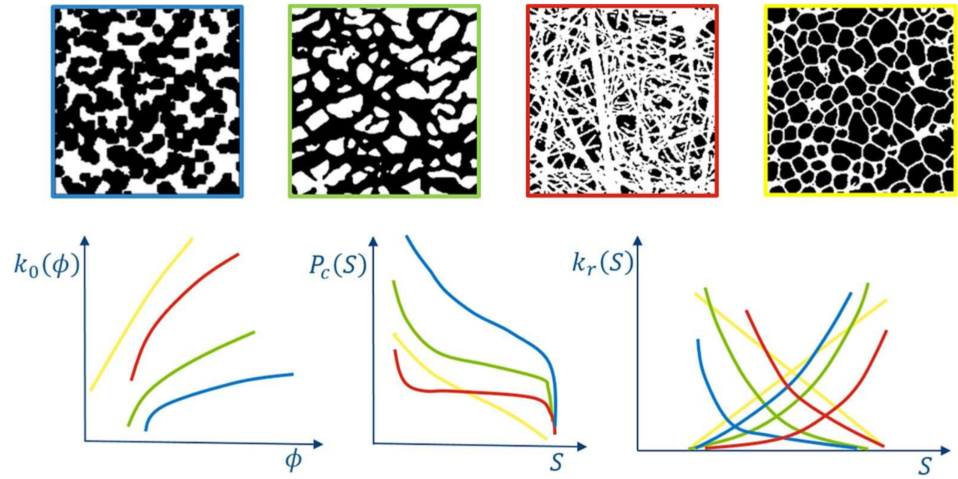

FIG. 10: Example of different PM types (top) and corresponding constitutive relationships (bottom): permeability vs. porosity, capillary pressure vs. saturation, relative permeability vs. saturation

$$\overrightarrow{D} = F_{\varepsilon}\left(\omega, \overrightarrow{k}, \overrightarrow{E}, \overrightarrow{r}, t, T(\overrightarrow{r})\right), \quad \overrightarrow{B} = F_{\mu}\left(\omega, \overrightarrow{k}, \overrightarrow{H}, \overrightarrow{r}, t, T(\overrightarrow{r})\right), \tag{4}$$

which encompasses a dependency on

- ω frequency, to describe the spectrum dispersion;
- $\overrightarrow{k}$ wave vector, dependency on the $\overrightarrow{E}$ propagation direction and other nonreciprocity effects;

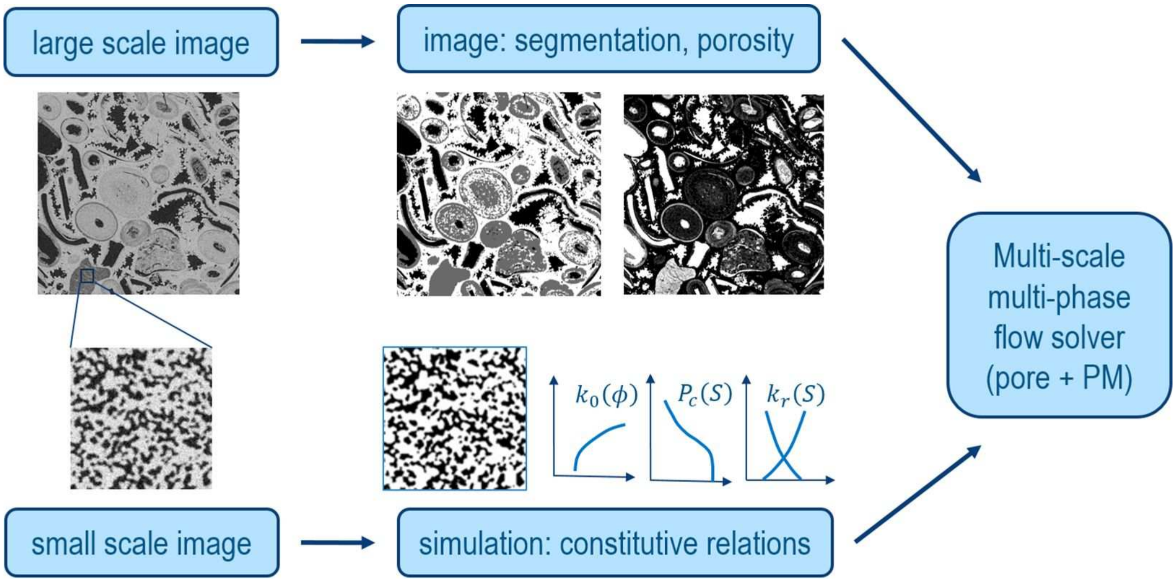
large scale image
image: segmentation, porosity
Multi-scale multi-phase flow solver (pore + PM)
small scale image
simulation: constitutive relations
$k_0(\phi)$
$P_c(S)$
$k_r(S)$

FIG. 11: Multiscale fluid flow workflow

- $\overrightarrow{E}$ ($\overrightarrow{H}$, respectively) field, to account for anisotropy (i.e., polarization) and for nonlinearity (i.e., second and third harmonics, Kerr and Raman effects) (Glahn et al., 2011);
- $\overrightarrow{r}$ point in space, t time and $T(\overrightarrow{r})$ temperature.

The functional relationship in Eq. (4) offers a macroscopic view of the material properties and a *homogenization* of the underlying stochastic interaction of the electromagnetic field with matter at the molecular or atomic level.

Under some ideal simplifying assumptions analytical solutions can be derived, for instance, for the dispersion properties. This leads to a macroscopic description with a reduced set of parameters such as relaxation time (Debye first and second order), resonance (Lorentz), and plasma/collision frequency (Drude). Further models we support are the gyrotropic model and the Kerr and Raman nonlinear model. For magnetostatic and quasistatic calculations we also provide nonlinear soft (e.g., electrical sheets) and hard (i.e., permanent magnets) temperature-dependent magnetic materials.

An additional nonlinear and hysteresis based Drude material model is used in the simulation of plasma reactors (Fig. 12).

However, for all the above described material models, only in rare cases is an analytical approach applicable, as the material data stem from data sheets or, at best, from in-house measurements. For such cases, we provide signal processing tools to perform data smoothing (to filter measurement noise) and vector fitting of the data,

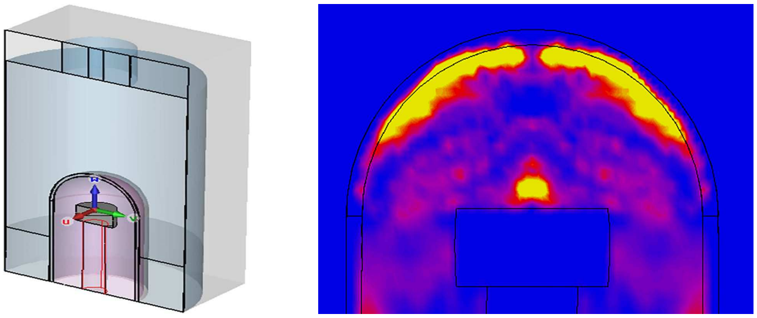

FIG. 12: Geometry and electromagnetic field of plasma chamber

$$\varepsilon(\omega) = \varepsilon_\infty + \sum_{n=1}^{N} \frac{\beta_{0,n}}{\alpha_{0,n} + j\omega} + \sum_{n=1}^{M} \frac{\gamma_{0,n} + j\omega\gamma_{1,n}}{\delta_{0,n} + j\omega\delta_{1,n} - \omega^2}, \tag{5}$$

leading to a robust reduced order model which enforces passivity, causality, and the Kramers–Kronig relationships.

The decomposition in Eq. (5) not only allows an efficient simulation (in the sense of computational memory and time) but also an additional insight into the material properties which can be further utilized during the design process. This is especially true for optical materials and the selection of their transparent/blocking region and their resonance frequencies (Fig. 13).

Available (even if partly) *a priori* information can still be used for a better model calibration and more accurate results. To this category belong, for instance,

- The Djorjevic Sarkar model (Svensson and Dermer, 2001; Djordjevic et al., 2001) and an optimized logarithmic pole expansion for the constant $\tan\delta = \varepsilon''/\varepsilon'$ of lossy dielectrics such as FR4.
- The graphene plasmonic models for optical resonators (Fig. 14), lenses, and optical waveguides.
- Cole-Cole relaxation models and other human and biological models for magnetic resonance imaging simulation and related specific absorption rate measurements.

A final mention is required for the metamaterial family, which finds application in the field of antenna radomes, frequency selective surfaces, cloaking devices, and radar cross section reduction. These *ad hoc* (random or periodic) assemblies of 3D structures made, e.g., of microstrips, metal loops, and dipoles (Fig. 15) can be treated in our simulations by an equivalent volumetric material.

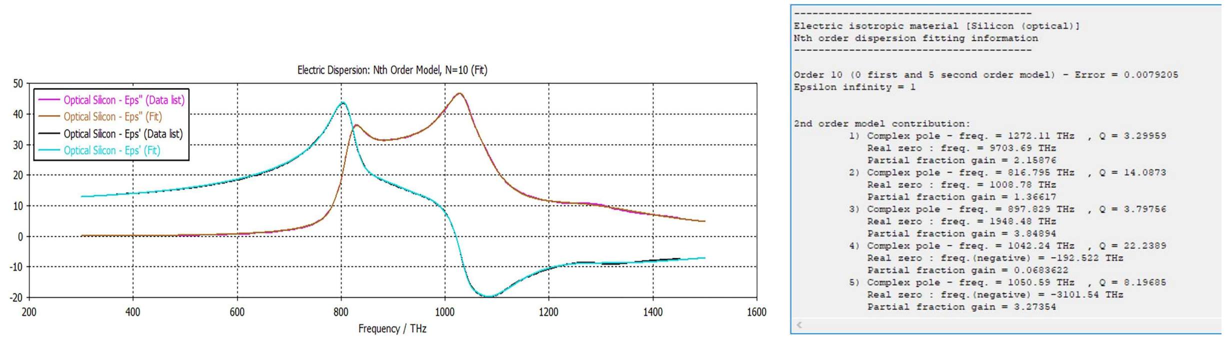

```
--------------------------------------
Electric isotropic material [Silicon (optical)]
Nth order dispersion fitting information
--------------------------------------

Order 10 (0 first and 5 second order model) - Error = 0.0079205
Epsilon infinity = 1


2nd order model contribution:
         1) Complex pole - freq. = 1272.11 THz  , Q = 3.29959
            Real zero : freq. = 9703.69 THz
            Partial fraction gain = 2.15876
         2) Complex pole - freq. = 816.795 THz  , Q = 14.0873
            Real zero : freq. = 1008.78 THz
            Partial fraction gain = 1.36617
         3) Complex pole - freq. = 897.829 THz  , Q = 3.79756
            Real zero : freq. = 1948.48 THz
            Partial fraction gain = 3.84894
         4) Complex pole - freq. = 1042.24 THz  , Q = 22.2389
            Real zero : freq.(negative) = -192.522 THz
            Partial fraction gain = 0.0683622
         5) Complex pole - freq. = 1050.59 THz  , Q = 8.19685
            Real zero : freq.(negative) = -3101.54 THz
            Partial fraction gain = 3.27354
```

(a) (b)

FIG. 13: (a) Silicon permittivity in optical range (300–1500 THz) and (b) identified resonance frequencies

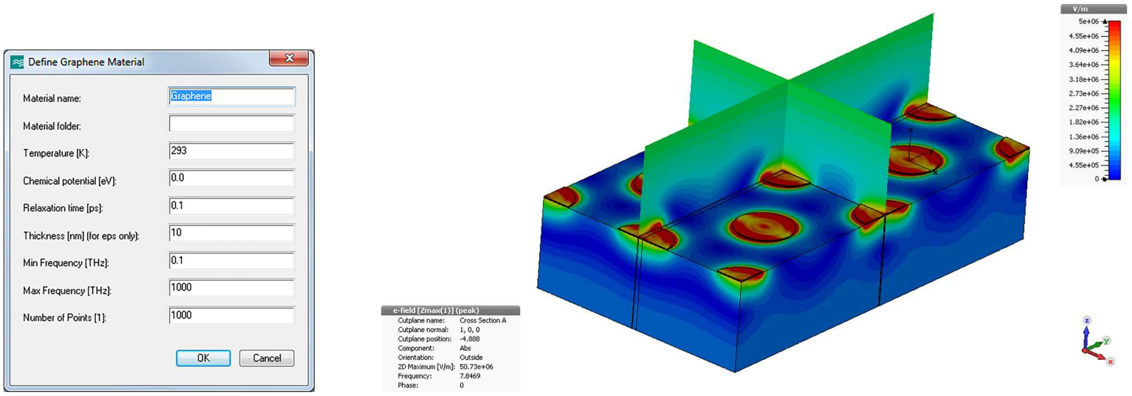

Material name:	Graphene
Material folder:	
Temperature [K]:	293
Chemical potential [eV]:	0.0
Relaxation time [ps]:	0.1
Thickness [nm] (for eps only):	10
Min Frequency [THz]:	0.1
Max Frequency [THz]:	1000
Number of Points [1]:	1000

e-field [Zmax(1)] (peak)

Cutplane name:	Cross Section A
Cutplane normal:	1, 0, 0
Cutplane position:	-4.888
Component:	Abs
Orientation:	Outside
2D Maximum [V/m]:	50.73e+06
Frequency:	7.8469
Phase:	0

FIG. 14: Graphene-plasmonic resonator at 7.8 THz (based on Yan et al., 2012)

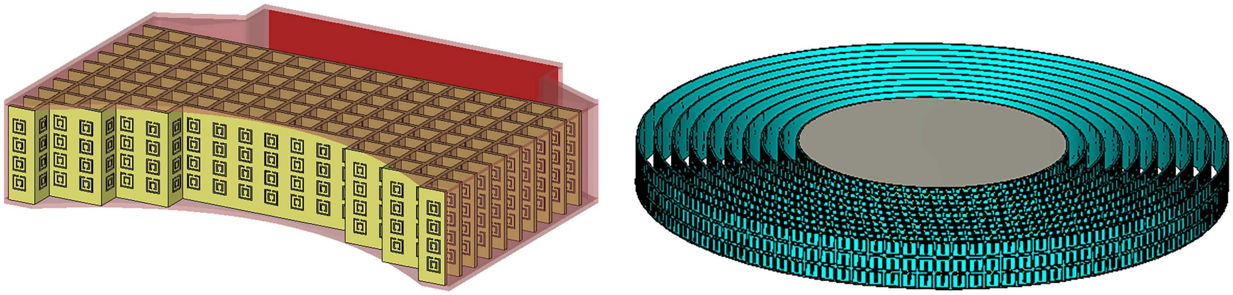

FIG. 15: Example of metamaterial layout and assembly—compact horn and cloaking device

We propose a three-step procedure (Fig. 16), which *a posteriori*, due to its generality, is not limited to the metamaterial class only.

Step 1. Perform a simulation of 3D metamaterial structure only—as either a whole or as a periodic unit cell (Fig. 17) with the Floquet modes. This simulation provides the reflection/transmission property of the material, e.g., in the form of S-parameters.

Step 2. Apply via VBA macro reverse engineering and vector fitting of the S-parameters to extract the complex permittivity $\varepsilon_{\mathrm{eff}}$ and permeability μ_{eff} to define the equivalent volumetric material (Fig. 18). Alternatively, the S-parameters can be used to generate a compact model (see Section 2.8.2).

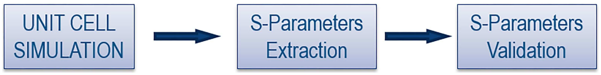

FIG. 16: Metamaterial modeling workflow

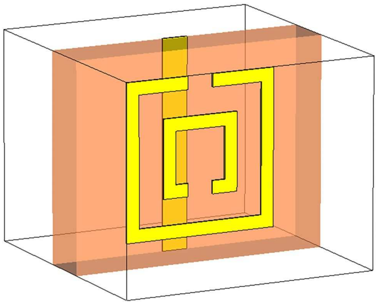

FIG. 17: Definition of resonator unit cell

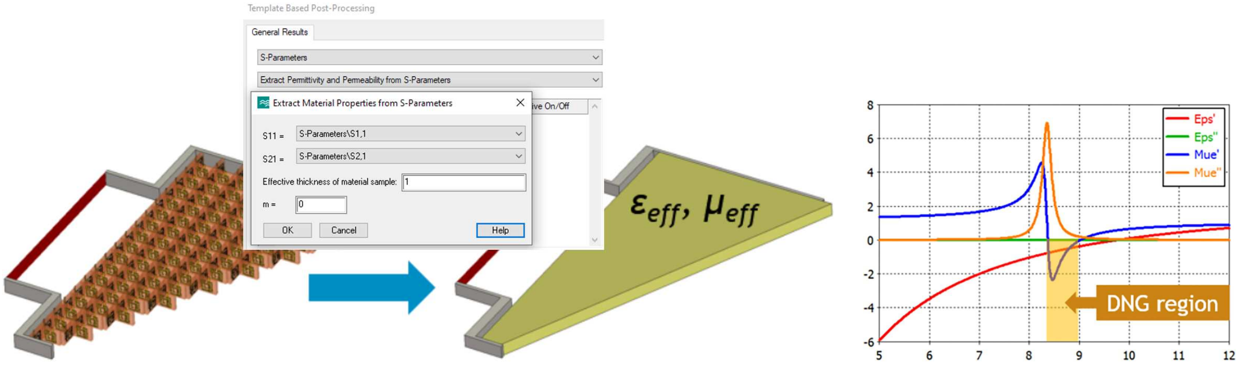

S-Parameters

Extract Permittivity and Permeability from S-Parameters

S11 = S-Parameters\S1,1

S21 = S-Parameters\S2,1

Effective thickness of material sample: 1

m = 0

FIG. 18: Modeling of double-negative metamaterial as 3D equivalent volumetric material

Step 3. Validate the obtained model with measurements, if available. Apply the material to the geometry and perform the complete simulation (Fig. 19).

Most of the mentioned models can also be enriched, according to Eq. (4), with an additional temperature, space, and time dependency by means of the following:

- an *indirect* mapping, i.e., describing the function $\varepsilon(T)$, $\mu(T)$ and importing a temperature field $T(\overrightarrow{r})$ from our thermal solver or from Abaqus;
- a *direct* mapping, i.e., importing the entire $\varepsilon(\omega, \overrightarrow{r}, t)$ and $\mu(\omega, \overrightarrow{r}, t)$ field. This field can be either generated by other modules in our suite, e.g., by a low frequency/static solver or imported from external tools.

This allows multiphysics and coupled simulations in which thermal, mechanical, and electromagnetic solvers jointly run iteratively up to a steady-state solution.

2.8.2 Transparencies and Multilayer Model

Nowadays, thanks to the massive increase in computational power, to evaluate the antenna field propagation inside a car or the radar signature in the K_u–K_a band of an entire airplane (Fig. 20) is not exceptional anymore. Still, the huge differences in scale between the entire model and some of its details—e.g., layered composites, gaps between panels, paint coating—represent a challenge to the simulation, especially for the CAD design and for the mesh generation.

The goal of an efficient and robust modeling is to replace such complex multiscale-multilayer structures with surface materials that are equivalent in terms of the exterior field behavior. To this purpose, we introduced the so-called compact model material. This enforces an electromagnetic field discontinuity, even if attached to a zero-thickness sheet geometry, and accounts for both reflection (e.g., for radar applications) and field transmission through the layers (for electromagnetic compatibility applications).

- If each layer material is known by its electromagnetic properties, a stack-up definition is generated by assigning a thickness to each layer and, in the case of anisotropy, a local coordinate rotation angle. Our material module determines the scattering properties for electromagnetic waves impinging on the material by computing the theoretical S-parameters and a reduced order model through vector fitting.
- If the multilayer material is only available through data sheet or measurements, the S-parameters can then be imported into our tool as a function of frequency, according to several different formats, e.g., CSV or

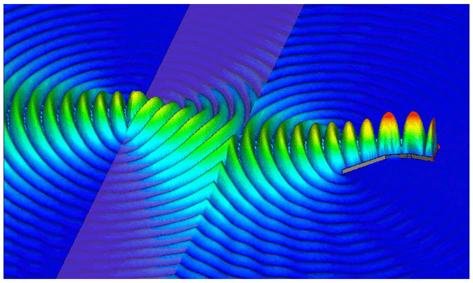

FIG. 19: Electric field in double-negative metamaterial slab in front of a horn antenna

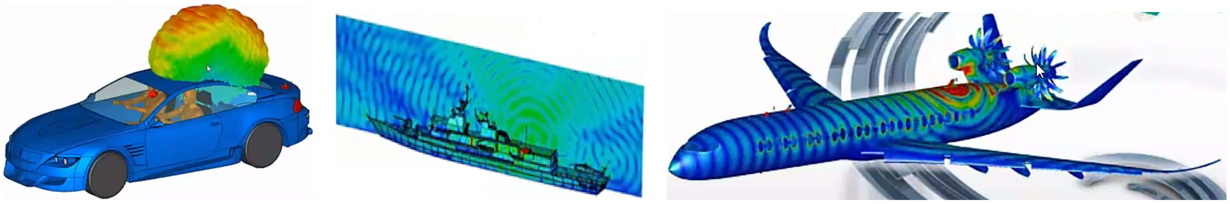

FIG. 20: GPS far field from car at 1.5 GHz. Radiated field from antenna on ship and on aircraft.

Touchstone (Fig. 21). Isotropic and anisotropic materials are both supported and additional unsymmetrical setups can be further exploited. For ray tracing or very high frequency (geometrical optics) applications a dependency on the propagation angle or wave polarization can be specified.

The original data can be used as directly imported. However, in practice, we recommend a preprocessing step to filter out measurement noise, to smoothen and fit the data (as for the volumetric materials, see Section 2.8.1) and to ensure causality and passivity of the final model.

The generated material model can be then applied to the geometry to perform the complete simulation (Fig. 22).

The very same approach can be applied when the material input data are not measured but are given as the result of a previous numerical simulation. This multiscale/multidomain approach enables a deeper insight into the building blocks, first considered as independent and then as interconnected, and results in a more efficient design with faster optimization cycles.

2.9 Numerical Approach—Representative Volume Element Modeling and Simulation

Representative volume element (RVE) modeling with finite elements (FE-RVE) encompasses the use of specialized constraints to subject a finite element model of a representative volume of material to an "average" field history to determine the local fields that arise in the RVE.

2.9.1 RVE Definition and Modeling

The characteristic length scale of an RVE has a broad range, from submicron resolution of nanocomposite inclusions to millimeter-scale structures such as additively manufactured lattices, honeycomb core panels, or textile tows, and potentially even larger. The distinguishing characteristic is that there is generally an orders-of-magnitude difference between the length scale of features in the RVE and the length scale of the larger-scale engineering structures for which the "average" field in the RVE corresponds to a local field value.

FE-RVE modeling can be applied in a variety of ways to multiscale simulation. These are a few examples of workflows in which FE-RVE simulation plays a part:

1. Predicting an RVE's linear volume-average response under particular average deformations and thermal loadings to obtain its fully anisotropic elastic stiffness and thermal expansion behavior.

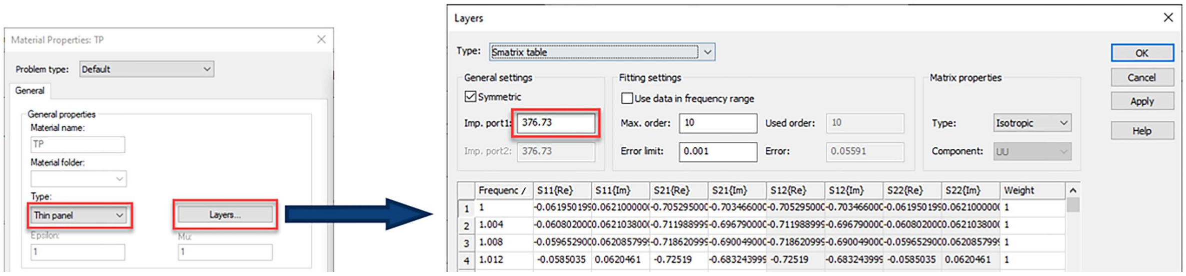
Material Properties: TP

Problem type: Default

Material name: TP

Material folder:

Type: Thin panel

Epsilon: 1

Mu: 1

Layers

Type: Smatrix table

☑ Symmetric

Imp. port1: 376.73

Imp. port2: 376.73

☐ Use data in frequency range

Max. order: 10

Used order: 10

Error limit: 0.001

Error: 0.05591

Type: Isotropic

Component: UU

	Frequenc /	S11{Re}	S11{Im}	S21{Re}	S21{Im}	S12{Re}	S12{Im}	S22{Re}	S22{Im}	Weight
1	1	-0.06195019	0.062100000	-0.70529500	-0.70346600	-0.70529500	-0.70346600	-0.06195019	0.062100000	1
2	1.004	-0.06080200	0.062103800	-0.71198899	-0.69679000	-0.71198899	-0.69679000	-0.06080200	0.062103800	1
3	1.008	-0.05965290	0.06208579	-0.71862099	-0.69004900	-0.71862099	-0.69004900	-0.05965290	0.06208579	1
4	1.012	-0.0585035	0.0620461	-0.72519	-0.68324399	-0.72519	-0.68324399	-0.0585035	0.0620461	1

FIG. 21: Multilayer definition dialog—general import assembly

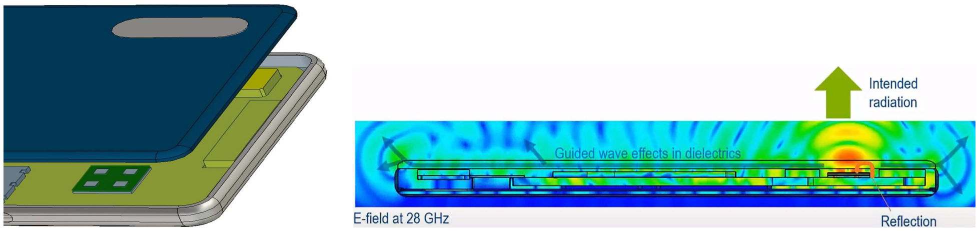

FIG. 22: Radiated field of phone device at 28 GHz with radome

2. Subjecting an RVE to a particular volume-average deformation history and calculating its average nonlinear stress response, including many kinds of complex nonlinear phenomena at the scale of the RVE (self-contact of voids, microbuckling, fluid cavities, microscale plasticity, and damage, fracture, etc.) (McLendon et al., 2019).
3. Predicting failure initiation in engineering-scale structures based on the relationship between the average field in the RVE and the resulting local field solution (McLendon and Whitcomb, 2013).
4. Determining *in situ* constituent material properties through a calibration exercise in which the properties of an RVE's constituents are optimized to cause the RVE to yield a response matching tests of a composite. In this way, properties which may not be tractable to directly measure (e.g., transverse properties of carbon fibers) can be inferred through simulation (Fish and Ghouli, 2001; Oskay and Fish, 2008; Ballard et al., 2014; McLendon and Whitcomb, 2016).
5. Determining relationships between designable material parameters (e.g., volume fraction in a composite or void fraction in an additively manufactured lattice) and the effective response of the resulting materials (McLendon et al., 2017).
6. Predicting effective section behavior of complex shell-type structures such as corrugated and honeycomb panels.
7. Evaluating the accuracy of the assumptions in mean field homogenization for a given material system based on the uniformity of the local fields in each constituent.
8. Calculating the mean strain concentration tensors for each constituent in a composite for use in linear mean field homogenization material models.
9. Developing reduced order homogenization models (Oskay and Fish, 2007) or surrogate models to facilitate nonlinear multiscale analyses.

The advanced design capabilities of CATIA (including Generative Shape Design, Part Design, xGenerative Design, etc.) provide users the ability to model complex shaped microstructures, taking into account the variability of the microstructure, which is a result of the manufacturing process variability. This need to accurately model the microstructure is due to the level of detail expected to be considered. This complex modeling remains particularly significant for composites application with a real fiber arrangement or the weaving of fiber tows. The minimum distance between fibers or the tow profile can massively change the stress concentration distribution. Porous materials can be modeled also with a random distribution of pores over the RVE. One of the key challenges of RVE modeling is the ability to generate periodic morphologies. To satisfy that requirement a combination of geometric constructs and specialized periodic boundary conditions is employed.

2.9.2 RVE Boundaries and Loads for Multiscale Analysis

The SIMULIA Abaqus finite element solver has long included the technology required to perform FE-RVE analysis. However, the correct imposition of constraints and load histories, and performing homogenization and post-processing is a tedious process. To aid in this, in 2016 the Micromechanics Plugin (Fig. 23) was created for Abaqus/CAE to automate many of the more challenging aspects of FE-RVE modeling (McLendon, 2017).

The plugin allows the user to create their own FE-RVE model and begin in the *Loading* screen to impose constraints and loads. The plugin also offers functionality to parametrically create FE-RVE models of a number of common geometries, including hexagonal arrays of unidirectional fibers, arrays of ellipsoids, and various lattice geometries (Fig. 24).

One of the key aspects the plugin handles is the definition of constraints on the RVE. A number of different constraints are possible for FE-RVE modeling as shown in Fig. 25. Among the simplest is the so-called Taylor or Voigt constraint (Taylor, 1938) in which the RVE is subjected to uniform deformation throughout its entire volume.

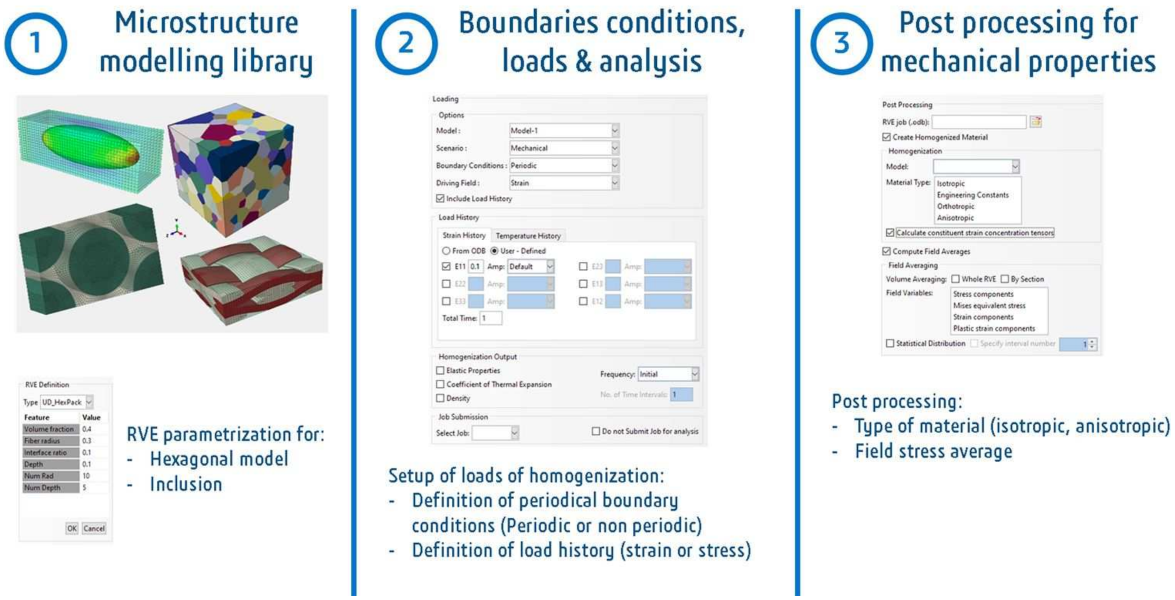

① Microstructure modelling library

RVE Definition

Type: UD_HexPack

Feature	Value
Volume fraction	0.4
Fiber radius	0.3
Interface ratio	0.1
Depth	0.1
Num Rad	10
Num Depth	5

RVE parametrization for:
- Hexagonal model
- Inclusion

② Boundaries conditions, loads & analysis

Loading

Options

Model : Model-1

Scenario : Mechanical

Boundary Conditions : Periodic

Driving Field : Strain

☑ Include Load History

Load History

Strain History | Temperature History

○ From ODB ● User - Defined

☑ E11 0.1 Amp: Default

☐ E22 Amp:

☐ E33 Amp:

☐ E23 Amp:

☐ E13 Amp:

☐ E12 Amp:

Total Time: 1

Homogenization Output

☐ Elastic Properties

☐ Coefficient of Thermal Expansion

☐ Density

Frequency: Initial

No. of Time Intervals: 1

Job Submission

Select Job:

☐ Do not Submit Job for analysis

Setup of loads of homogenization:
- Definition of periodical boundary conditions (Periodic or non periodic)
- Definition of load history (strain or stress)

③ Post processing for mechanical properties

Post Processing

RVE job (.odb):

☑ Create Homogenized Material

Homogenization

Model:

Material Type: Isotropic, Engineering Constants, Orthotropic, Anisotropic

☑ Calculate constituent strain concentration tensors

☑ Compute Field Averages

Field Averaging

Volume Averaging: ☐ Whole RVE ☐ By Section

Field Variables: Stress components, Mises equivalent stress, Strain components, Plastic strain components

☐ Statistical Distribution ☐ Specify interval number 1

Post processing:
- Type of material (isotropic, anisotropic)
- Field stress average

FIG. 23: Steps for the RVE definition through the user interface of FE-RVE Abaqus plugin

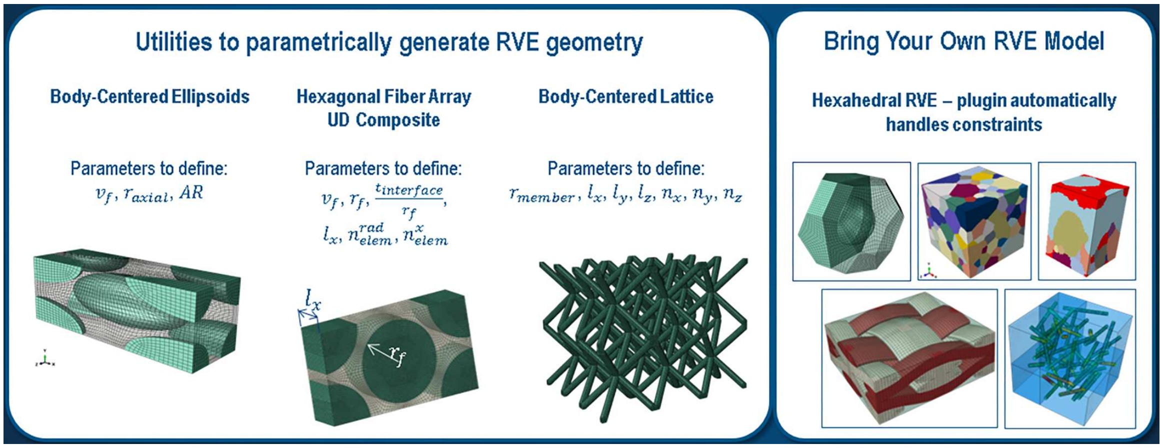

Utilities to parametrically generate RVE geometry

Body-Centered Ellipsoids

Parameters to define:
v_f, r_{axial}, AR

Hexagonal Fiber Array UD Composite

Parameters to define:
$v_f, r_f, \frac{t_{interface}}{r_f}, l_x, n_{elem}^{rad}, n_{elem}^{x}$

Body-Centered Lattice

Parameters to define:
$r_{member}, l_x, l_y, l_z, n_x, n_y, n_z$

Bring Your Own RVE Model

Hexahedral RVE – plugin automatically handles constraints

FIG. 24: FE-RVE geometries

A somewhat less restrictive option is to constrain the displacements of only the FE-RVE boundary to conform to the "average" deformation field. This is referred to as the *Uniform Surface Gradient* constraint in the plugin, although various names are used in the literature such as *Linear* (Nguyen et al., 2011), *Uniform Displacement* (Geers et al., 2017), *Rigid* (Mesarovic and Padbidri, 2005), *Linear Displacement* (Saeb et al., 2016), and *Essential* (Fish, 2014). Both this and the *Taylor*/Voigt type constraint can be imposed using the plugin (the *Taylor*/Voigt type by manually specifying that all the nodes in the model be constrained). An additional type of constraint that can be applied is the *Uniform Surface Flux* (also commonly called *Neumann* or *Natural*) type boundary condition in which the average flux field (stress or heat) is uniformly applied to the RVE boundary as a traction or surface flux. The plugin supports this constraint only for certain types of geometries and with a number of limitations compared to constraints based on displacement or temperature. One benefit of all the aforementioned constraints is that they are appropriate for nonperiodic RVE models, such as those originating from 3D scans of actual material microstructures. All RVE boundary conditions provided by the plugin assume that the solution gradient considered at larger scales (e.g., the far-field solution gradient) is uniform, making this a first-order homogenization method.

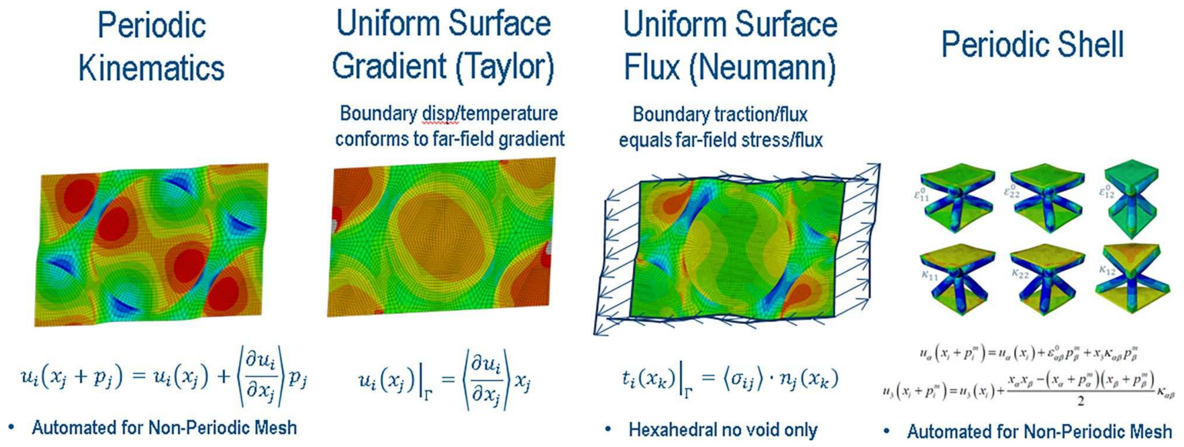
Periodic Kinematics
Uniform Surface Gradient (Taylor)
Boundary disp/temperature conforms to far-field gradient
Uniform Surface Flux (Neumann)
Boundary traction/flux equals far-field stress/flux
Periodic Shell
ε_{11}^0
ε_{22}^0
ε_{12}^0
κ_{11}
κ_{22}
κ_{12}
$u_i(x_j + p_j) = u_i(x_j) + \left\langle \frac{\partial u_i}{\partial x_j} \right\rangle p_j$
$u_i(x_j)\big|_\Gamma = \left\langle \frac{\partial u_i}{\partial x_j} \right\rangle x_j$
$t_i(x_k)\big|_\Gamma = \langle \sigma_{ij} \rangle \cdot n_j(x_k)$
$u_\alpha(x_i + p_i^m) = u_\alpha(x_i) + \varepsilon_{\alpha\beta}^0 p_\beta^m + x_3 \kappa_{\alpha\beta} p_\beta^m$
$u_3(x_i + p_i^m) = u_3(x_i) + \frac{x_\alpha x_\beta - (x_\alpha + p_\alpha^m)(x_\beta + p_\beta^m)}{2} \kappa_{\alpha\beta}$
• Automated for Non-Periodic Mesh
• Hexahedral no void only
• Automated for Non-Periodic Mesh

FIG. 25: Overview of RVE constraints available in plugin

For the case of RVEs exhibiting repeating patterns, *periodic* constraints allow the recovery of the response of an infinite array of repeating unit cells through the analysis of a single unit cell by assuming the solution field in the RVE varies in a periodic manner according to the following equation:

$$u_i(X_k + p_k) = u_i(X_k) + \left\langle \frac{\partial u_i}{\partial X_k} \right\rangle p_k, \tag{6}$$

where u_i is the field assumed to vary in a periodic manner (in force-displacement simulations, this is displacement), X_k is the reference coordinate in the RVE, and p_k is a vector of periodicity that runs between equivalent points in adjacent unit cells. The term in angle brackets $\langle \partial u_i / \partial X_k \rangle$ is the volume-average gradient of the solution field in the unit cell corresponding to the uniform field gradient considered at larger scales. In the case of force-displacement simulation, this is the volume-average displacement gradient. This constraint is imposed using linear equation constraints applied to the unit cell boundary and global degrees of freedom (DOFs) corresponding to the components of the average solution field gradient for the RVE. Volume-average loading is applied to the FE-RVE through these global DOFs. For periodic FE-RVEs with a hexahedral unit-cell shape and faces that are flat and aligned with the global axes, the plugin automatically identifies the nodes to constrain and imposes the constraints. For models that are not hexahedra (such as hexagonal prisms, truncated octahedra, or any other shape that translationally tessellates in 3-space), the user can manually identify the pairs of faces that are related by a vector of periodicity for the unit cell. For models that exhibit periodic geometry but not periodic node positions (perhaps due to the use of a free tetrahedral mesher), the plugin uses a novel approach leveraging the tie constraint functionality in the Abaqus solver to impose the periodic constraints.

In addition to constraints for RVEs embedded in a theoretically infinite medium, the plugin provides so-called *solid-to-shell* periodic constraints that are applicable to structures with finite thickness and in-plane periodicity (such as corrugated or honeycomb panels). Such constraints, described in detail in work by Karkkainen et al. (2007) subject the RVE to an average shell-type deformation and permit the determination of shell section stiffness properties (i.e., the so-called *ABD* matrix) relating shell resultant forces and moments with membrane strains and curvature based on an assumption of in-plane periodicity rather than in-plane uniformity inherent in laminated plate theory, permitting these complex structures to be accurately modeled using simple shell elements in engineering-scale analyses.

In addition to automation of constraint creation, the plugin also automates the creation of analysis steps and loads required to impose the average field history and perform homogenization as requested by the user. Field histories can be defined manually or can come from history data at some location of a prior analysis. Finally, the plugin provides functionality to post-process RVE simulations. The plugin calculates homogenized material properties such as elastic stiffness, shell section stiffness, thermal expansion, and thermal conductivity, and writes these to new material definitions or general shell section definitions in Abaqus/CAE. The plugin also calculates average field histories (e.g., volume-average strain and stress) in each constituent and for the whole RVE, and calculates histograms of field quantities within constituents and the whole RVE at particular times. Displacement, steady-state heat transfer, and coupled temperature-displacement analyses are supported. An overview of the capabilities is shown in Fig. 26.

2.10 Material Multiscale at Larger Scales

To take full advantage of the micro- and mesoscale characterizations it is critical to have efficient and scalable macromodeling features that incorporate small-scale responses and behaviors in component sized (macroscale) models. SIMULIA offers a complete range of efficient and complementary macromodeling features.

2.10.1 Materials

SIMULIA offers a wide range of advanced material modeling options for applications across many industries. Most SIMULIA constitutive models support a full range of element technologies and dimensional domains including 1D, 2D (plane stress, plane strain), axisymmetric, 3D, and structural elements (trusses, beams, and shells). In addition, many of the Abaqus material models are “micromechanics informed” which means they can capture some microscale behaviors at the macroscale and have special output variables that can provide valuable insight into the microscale responses. “Micromechanics informed” materials are discussed more in Section 2.11.

The SIMULIA concrete damage plasticity is an excellent example of an advanced “micromechanics informed” material model. Designed for modeling concrete and other quasibrittle materials it supports separate damage mechanisms for both tensile cracking and compressive crushing, rate dependence, tension stiffening for modeling rebar reinforcement, stiffness recovery under cyclic loading, and failure. It also supports a set of material-specific output variables, that among other things, allows you to visualize cracking patterns in the concrete.

2.10.2 Element Technology

SIMULIA has an extensive element library (Fig. 27) to provide a powerful set of tools for solving many different problems.

In addition to a full set of conventional continuum and structural elements, SIMULIA supports a wide range of special elements and functionality specifically designed to support the modeling of small-scale phenomenon in large-scale modeling features.

- *Composite solids and shells*. Composite elements allow for economical modeling of complex layered materials. They inherently support both bottom-up (upscaling) and bottom-down (downscaling) approaches (Fig. 28).

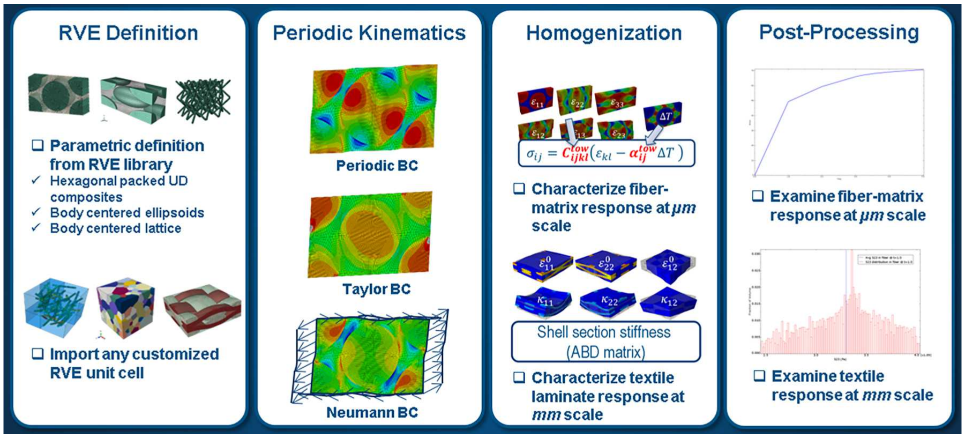
RVE Definition
❑ Parametric definition from RVE library
✓ Hexagonal packed UD composites
✓ Body centered ellipsoids
✓ Body centered lattice
❑ Import any customized RVE unit cell
Periodic Kinematics
Periodic BC
Taylor BC
Neumann BC
Homogenization
ε_{11} ε_{22} ε_{33} ε_{12} ε_{13} ε_{23} ΔT
$\sigma_{ij} = C^{tow}_{ijkl}(\varepsilon_{kl} - \alpha^{tow}_{ij}\Delta T)$
❑ Characterize fiber-matrix response at μm scale
ε^0_{11} ε^0_{22} ε^0_{12} κ_{11} κ_{22} κ_{12}
Shell section stiffness (ABD matrix)
❑ Characterize textile laminate response at mm scale
Post-Processing
❑ Examine fiber-matrix response at μm scale
❑ Examine textile response at mm scale

FIG. 26: Overview of micromechanics plugin capabilities

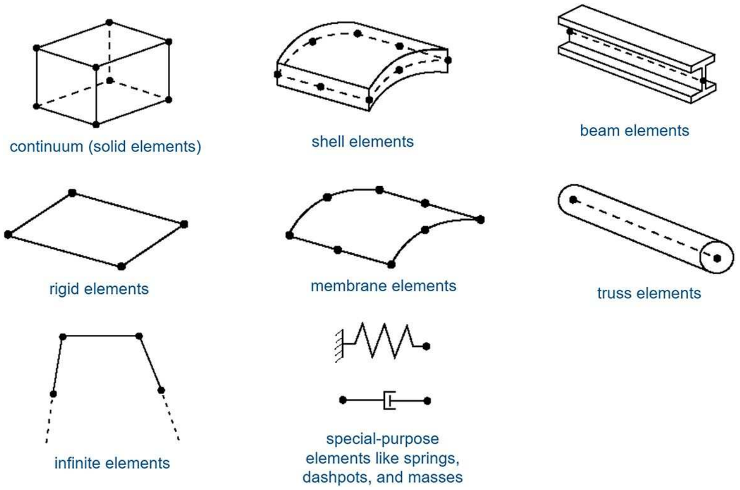
continuum (solid elements)
shell elements
beam elements
rigid elements
membrane elements
truss elements
infinite elements
special-purpose elements like springs, dashpots, and masses

FIG. 27: Basic Abaqus element families

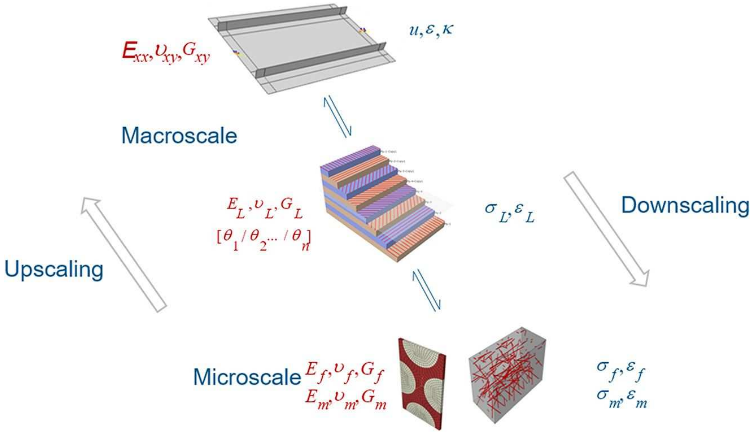
$E_{xx}, \upsilon_{xy}, G_{xy}$
u, ε, κ
Macroscale
E_L, υ_L, G_L
$[\theta_1/\theta_2 \ldots /\theta_n]$
σ_L, ε_L
Downscaling
Upscaling
Microscale
E_f, υ_f, G_f
E_m, υ_m, G_m
σ_f, ε_f
σ_m, ε_m

FIG. 28: Upscaling and downscaling schematic for composite finite elements

SIMULIA composite elements include 3D continuum, shell, and beam elements. The SIMULIA shell elements support two modeling options: pre-integrated material responses and material responses that are integrated during the simulation. The pre-integrated shells offer a very economical approach for composite modeling when linear elastic behavior is acceptable. For simulations that require nonlinear material response, including plasticity and failure within the composite layers, integrating the shell material response during the simulation is required.

- *Meshed beams*. The response of some structures is beamlike, yet the beam cross-section geometry or the multimaterial makeup of the cross section does not permit the use of a predefined library beam cross section, e.g., Fig. 29. In these cases, a meshed cross section can be used to model the beam cross section and to generate beam cross-section properties appropriate for subsequent use in a 1D-beam analysis.
  SIMULIA supports 3-DOF warping elements to model a meshed composite beam cross section. These elements capture the effect of in-plane warping on the stiffness properties of a composite beam element using this cross section. The warping elements can be used with all of the existing three-dimensional linear elastic material laws, for example, to generate realistic models for all kinds of laminates in a wind turbine rotor blade. In addition, you can recover the full three-dimensional strain and stress in the cross-section planes given the beam element deformations from subsequent analyses.

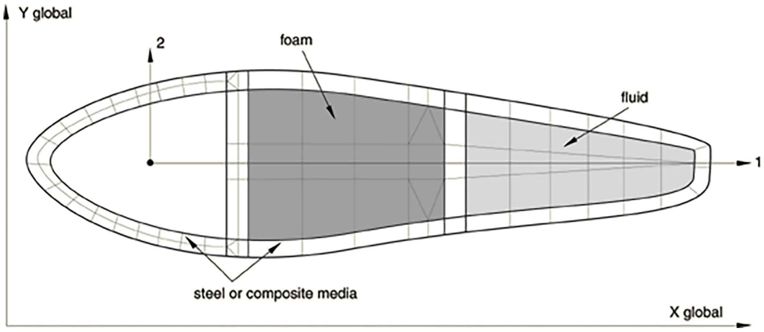

FIG. 29: Sample composite beam cross section

Meshed beam cross sections can be used in both Abaqus finite element simulations or Simpack multibody simulations (see Section 5.2).

- *Rebar and embedded elements*. Many important engineering structures are constructed using reinforced bulk matrix materials. For example, in civil engineering structures, the high tensile strength of steel rebar complements the high compressive strength of concrete. In pneumatic tires, the good wear and handling characteristics of the rubber are supported by radial plies and belts which supply tensile strength (see Section 5.1).
  The rebar layer and embedded element technology in Abaqus provide an efficient means for including the small-scale details of many types of reinforcement in large-scale simulations.
  Rebar layers are used to define layers of uniaxial reinforcement in membrane, shell, and surface elements (such layers are treated as a smeared layer with a constant thickness equal to the area of each reinforcing bar divided by the reinforcing bar spacing). Solid elements are reinforced using embedded element constraints in which either shell, membrane, or surface elements reinforced with rebar layers are embedded in the host matrix comprised of solid elements.

- *Fracture technology and interface behavior*. Fracture is inherently a small-scale phenomenon. At the microscale forces are pulling or laterally moving two molecules apart; as soon as they reach a certain distance the molecules are separated, and have consumed a certain energy resulting in a “micro” crack, or in metals, a void. There are millions of molecules active in the formation of an observable crack; all of them have a statistical variation in their bonding strength, and thus also in the energy needed to break them. Solving the micromechanical problem directly, however, is very hard. Depending on this and other processes that happen at the microscopic scale, and how they become observable on the macro scale, we “see” plasticity, cracking, or possibly nothing directly at all and call the long term repetitive fracturing behavior, fatigue. The goal of fracture mechanics is to relate observable macroscopic continuum quantities to when and how fracture occurs.
  SIMULIA offers a wide selection of macromodeling fracture technologies for ductile, brittle, and fatigue fracture. The features include continuum damage models, XFEM, VCCT (Fig. 30), cohesive elements, cohesive contact (Fig. 31), and fatigue. Recent research also provides alternative technologies that do not require cohesive technology to model intra- and interlayer damage (Yuan and Fish, 2016) and may be used with Abaqus via the user element subroutine interface.
  Fourteen research teams (from academia, labs, and industry) took part in a fracture challenge organized by Sandia National Labs (Boyce et al., 2016). In a clear testament to the value of our failure and fracture capabilities, nine out of the 14 participating teams used SIMULIA simulation technology—some of whom leveraged the openness that our user subroutines offer to include their own material and element technologies.

2.11 Micromechanics Informed Material Models

The analysis of large-scale structures with FEA requires a fine balance between solution accuracy and performance. At this level, it is usually impractical to perform a full monolithic multiscale analysis due to time and computational

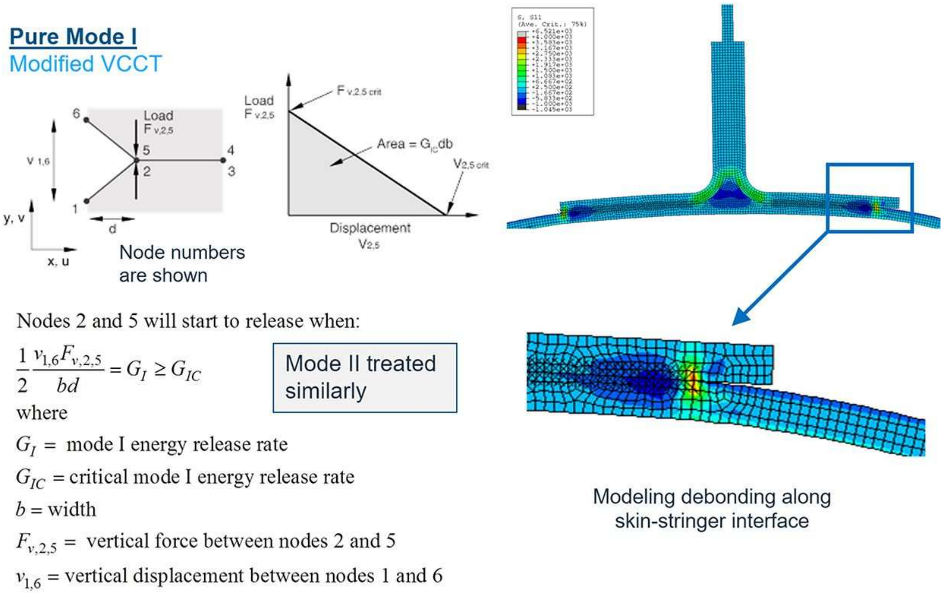
Pure Mode I
Modified VCCT
Load
$F_{v,2,5}$
6
5
2
4
3
1
$v_{1,6}$
y, v
x, u
d
Node numbers are shown
Load $F_{v,2,5}$
$F_{v,2,5\,crit}$
Area = $G_{IC}db$
$V_{2,5\,crit}$
Displacement $V_{2,5}$
Nodes 2 and 5 will start to release when:
$\frac{1}{2}\frac{v_{1,6}F_{v,2,5}}{bd} = G_I \geq G_{IC}$
where
G_I = mode I energy release rate
G_{IC} = critical mode I energy release rate
b = width
$F_{v,2,5}$ = vertical force between nodes 2 and 5
$v_{1,6}$ = vertical displacement between nodes 1 and 6
Mode II treated similarly
Modeling debonding along skin-stringer interface

FIG. 30: Summary of SIMULIA VCCT technology and an example simulation

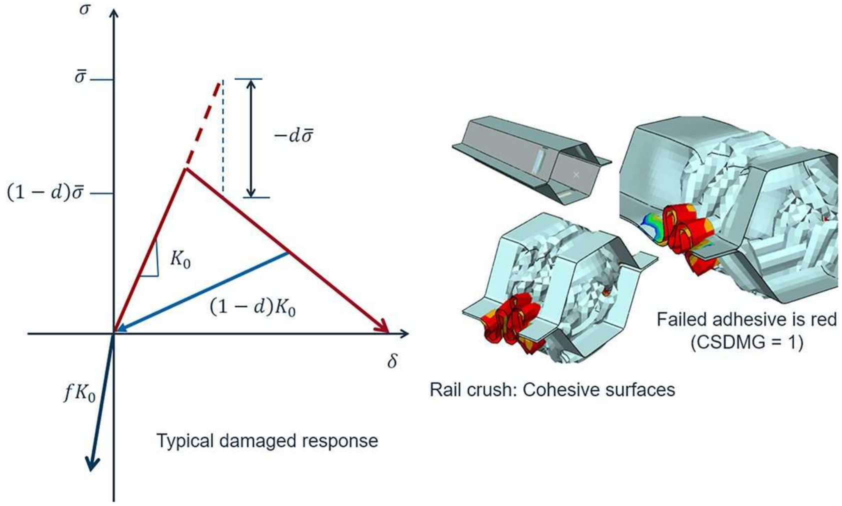
σ
$\bar{\sigma}$
$-d\bar{\sigma}$
$(1-d)\bar{\sigma}$
K_0
$(1-d)K_0$
δ
fK_0
Typical damaged response
Failed adhesive is red (CSDMG = 1)
Rail crush: Cohesive surfaces

FIG. 31: Typical damage behavior for SIMULIA cohesive technology and an example simulation

constraints. Instead, it is common to use a mathematical model, or *constitutive law*, to describe the macroscopic response of the material in an efficient way. These material laws can be purely phenomenological (or data-driven), or they can be microstructurally informed, meaning that the model formulation and parameters reflect on the microstructural characteristics of the material. This latter class of material models, usually called *structural constitutive models*, is the focus of discussion in this section.

Many types of structural models have emerged during the last two decades and have experienced a significant level of adoption in commercial simulation packages. For example, many structural models have been proposed to describe the strong anisotropy that composites materials and biological tissues exhibit when loaded along different directions. Most of these models introduce in their formulation the concept of structure tensors to represent the anisotropy of the material. (The structure tensor is usually defined as $\mathbf{M} = \mathbf{A}_0 \otimes \mathbf{A}_0$, where $\mathbf{A}_0$ represents the preferred direction of fibers in the material).

The development of structural models has gained significant traction in the field of biomedical applications. For instance, the nonlinear anisotropic model of Holzapfel et al. (2000) and Gasser et al. (2006) is a structure-based model suitable for computational simulation of arterial walls and other biological tissues. The model accounts for collagen fiber orientations as well as dispersions. Similarly, the model of Holzapfel and Ogden (2009) has gained wide adoption for the simulation of the passive response of cardiac tissue. Today this model is a key component of SIMULIA's Living Heart Project (Baillargeon et al., 2014).

More advanced tissue models include the Lanir and Sacks (Lanir, 1983; Sacks, 2003; see Section 4.5.1) microstructural model, which introduces fiber-recruitment and fiber-orientation distribution functions characterized from statistical analysis of histological sections of the tissue.

All these models make computational analysis and simulation of biological systems a reality, and they are readily available in Abaqus as part of SIMULIA's portfolio of solutions for large-scale simulations.

In the field of composite damage modeling, many failure criteria have been proposed using invariant formulations based on structural tensors. For instance, the ply-fabric model for woven composites in Abaqus (Johnson, 2001; Sokolinsky et al., 2011) includes a set of structural failure criteria to differentiate between fiber tension/compression failure, as well as matrix shear failure. Such models have proved to be very successful for the analysis of large-scale aerospace structures, providing a high degree of predictability. An example of a simulation of a bird strike impact on the leading edge of an airplane wing structure is shown in Figs. 32 and 33 (Al-Khalil et al., 2015). The J-Nose panel is constructed from carbon-woven fabric with a honeycomb core. The ply fabric damage criterion in Abaqus is used to model the woven fabric composite. The simulation accounts for nonlinear shear plasticity effects. As discussed in the reference, the model captures the appropriate amount of energy absorption during the impact event. Figure 33 also shows that the methodology is able to predict the onset of damage and penetration of the J-Nose structure. Overall, the simulation results correlate well with the physical test results, demonstrating the predictive capabilities of the model.

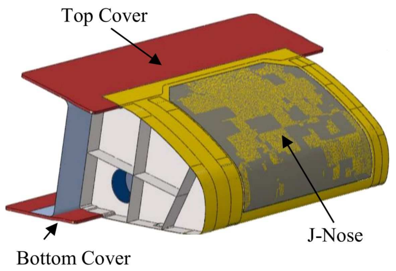

FIG. 32: A composite sandwich wing structure with a fixed leading edge

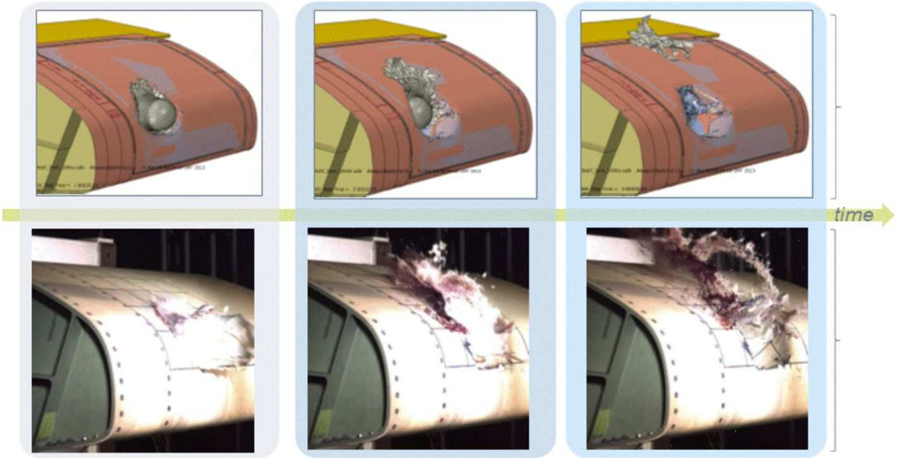

1.8 ms 3 ms 4.8 ms

FIG. 33: Damage to J-Nose with bird penetration (top: Abaqus results; bottom: test results)

In addition to the applications for composite materials and biological tissues discussed above, in recent years there has also been a widespread development of advanced micromechanics informed constitutive models for the analysis of cross-linked polymers. Cross-linked polymers are widely used across many industries (automotive, consumer products, medical devices, etc.), and have gained a significant level of attention from a modeling perspective. These materials consist of a three-dimensional network of randomly oriented molecular chains that can tangle and cross-link (resulting in elastomeric or hyperelastic properties) and can exhibit a time-dependent nonlinear viscoelastic response often associated with the relaxation of dangling chains in the network. The addition of fillers can lead to stress softening (Mullins effect) as well as permanent set. A number of models have been proposed inspired by the physical response of the polymer microstructure, usually introducing the concept of multiple networks connected in parallel. Examples include the three-network model of Bergstrom and Bischoff (2010) and the parallel rheological framework (PRF) model in Abaqus (Hurtado et al., 2013). These models provide more physically accurate predictions than traditional phenomenological models. For instance, the PRF model has been used successfully for the analysis of filled elastomeric materials that exhibit permanent set, Mullins effect, and nonlinear viscous behavior under large deformation (Govindarajan et al., 2008). An example of the PRF model can also be found in Section 4.2.1.4 (Oancea et al., 2017) in the context of multiscale modeling of a polyurea copolymer melt.

2.12 All: From *Ab Initio* to Continuum-Linked Scales

The vision of multiscale modeling is to use information generated at one scale to provide knowledge that improves a simulation at a different scale. There are three main ways of providing this connection:

- Structure—at its simplest level, this means being able to use a structure generated at one scale directly in a different scale. For example, a polymer may consist of both soft and hard blocks. This can be represented through coarse-grained molecular dynamics or another mesoscale dynamics method. However, at the mesoscale, it is not easy to calculate the overall mechanical properties of such a system. If the structure can be passed to an RVE model, and the mechanical properties of the soft and hard blocks are known, then the overall mechanical properties can be calculated. Materials Studio enables the creation of an Abaqus input file containing structures generated using coarse-grained simulations that can be modeled using the RVE method in Abaqus.
- Property—nanoscale models are used to estimate the properties of some materials. These are used to help calibrate material models for larger scale simulations. Connecting by property has the advantage that multiple scales can be bridged in a single connection (e.g., from nanoscale to FEA). However, challenges remain in the overall accuracy of the nanoscale calculations as the time scales used in nanoscale simulations are orders of magnitude faster compared with real experimental data. Researchers are using different approaches to work around this time-temperature superposition limitation, such as elevated temperatures (Park et al., 2018) or machine learning (Park et al., 2021).
- Cosimulation—execution of different simulations consecutively or simultaneously where information from one directly links to another. This has most successfully been applied when coupling different domains at similar size scale; for example, coupling structure-based finite element solvers with computational fluid dynamics solvers.

Choosing the most appropriate methods for solving a multiscale problem will depend on the modeled material and the property being predicted. There is no “silver bullet” solution to the general multiscale challenge and Dassault Systèmes provides a tool box of solvers that are all becoming available on the **3D**EXPERIENCE Platform. For specific problems, out of the box multiscale solutions are available and they will be discussed in further examples in this paper.

2.13 Uncertainty Quantification in Multiscale Modeling

Computational developments that culminate in the ICME approach have multiple goals, two of which are discussed here. On one hand, there is the traditional approach of improving qualitative understanding of material properties and processes, generating trends, and focusing on screening of the best candidates. On the other hand, ICME promises a quantitative contribution as well, so that more decisions in development and optimization of materials can be informed by computations in addition to experiments. This quantitative claim often requires a deeper understanding of the uncertainty of calculated results than current methods can provide; an additional problem in the multiscale picture is that uncertainties propagate from one scale to another and ultimately generate distribution of answers rather than a single result.

What are the main sources of errors? Atomistic simulations of materials that are based on quantum mechanics usually employ DFT, and this generates an inherent uncertainty—exchange-correlation effects are described only approximately, using one of the steps of Jacob's ladder (Perdew and Schmidt, 2001). It is well known that the simplest formulation, the local density approximation (LDA), overestimates the strength of interatomic bonds, while the next level up in terms of accuracy, the generalized gradient approximation (GGA), underestimates it. More accurate schemes such as meta-GGA often get intermediate answers between these two extremes. The bottom line is that LDA and GGA tend to, respectively, under- and overestimate material density by 3–5%, and over- and underestimate compressibility by 10–2%. Those errors become even more pronounced for the individual components of the elastic coefficients tensor for crystals. On top of this, DFT calculations typically describe the zero-temperature state of the system, and hence are difficult to compare to experiment; calculations that include thermal effects can be orders of magnitude more expensive. There are numerous other sources of errors that are related to DFT and can be partially corrected by introducing additional approximations: for example, lack of description of dispersion interactions between atoms and inaccurate representation of systems with localized electrons (compounds of *d*- and especially *f*-shell elements).

Molecular modeling with interatomic potentials, such as COMPASS III, relies on the transferability of potential functions. When those potentials are fitted to DFT databases, the DFT errors mentioned above propagate to the empirical functions. The finite size effect is present in both quantum and classical simulations—computational models mostly use periodic boundary conditions to describe crystals and polymers, so they include unphysical interactions between periodic images of atoms and defects. The time scale of simulations is also limited, so that, for example, the deformation rate or a cooling rate in either atomistic or phase-field simulation can be significantly higher than in experiments.

Certain material properties are derived from atomistic simulations using empirical models, which introduces an uncontrolled error. One example is the estimation of hardness and of fracture toughness based on elastic coefficients and on information about ionicity and metallicity of interatomic bonds (see Mazhnik and Oganov, 2019). We show our DFT results obtained with the Materials Studio CASTEP module, using the hardness model from Tian et al. (2012) and the fracture toughness model from Mazhnik and Oganov (2019). These data for ~ 60 inorganic materials illustrate typical scatter of calculated results relative to the measured properties; see Fig. 34. Uncertainty introduced by the use of empirical models does not show the same systematic trends as, for example, DFT uncertainty (LDA vs. GGA), which reduces the predictive power of the calculations.

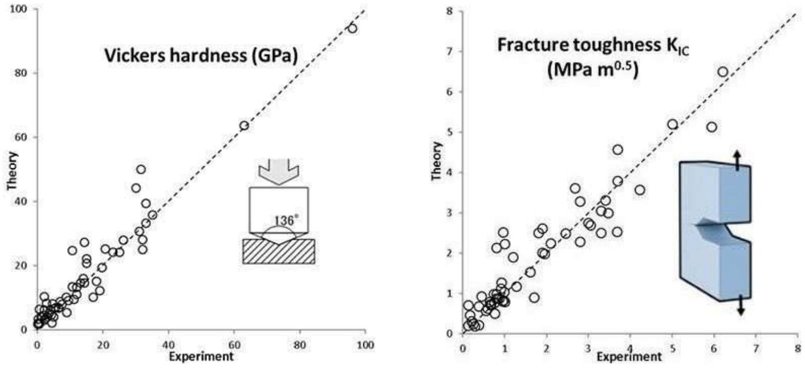

FIG. 34: Correlation between calculated (CASTEP, GGA exchange-correlation functional PBESOL) and experimental mechanical properties of inorganic materials

Uncertainty in macroscale simulations has both technical sources (approximations and assumption used by finite elements or phase-field solvers) and physical origins. For example, porosity in solids or random distribution of phases can be simulated by using random fields; the homogenization approach to simplify simulations of polycrystalline assembly of grains is popular, but does represent a source of uncertainty.

Propagation of uncertainty between length and time scales is an essential part of multiscale modeling and it is its major challenge; an excellent review of the topic is provided in Wang and McDowell (2020). We currently do not address uncertainty quantification in cross-scale computational studies. There is a clear need to improve this situation by using probabilistic methods, sensitivity analysis, etc. Further progress requires a combination of experimental and calculated data to build better models and to direct design of experiment using computations.

3. CRITICAL TECHNOLOGIES FOR THE PRACTITIONER

While material multiscale technologies as outlined in the previous section can be considered as critical building blocks for ICME, in practice material scientists/engineers often rely on additional technologies to advance their work. Microstructure parametric modeling, calibration, upscaling, and results mapping techniques are almost always required techniques to accomplish a tool chain despite not being technologies associated exclusively with the ICME practice. Microstructure parametric modeling allows parameterized modeling of microstructure characteristics such as grain morphology, porosity and inclusion shape and distribution, and the study of their effects on the material properties. Calibration often makes the connection between virtual methods and physical testing; aggregated materials are no exception. Upscaling technologies, such as coarse graining, are sometime mandatory in order to assess RVEs of meaningful size. Mapping techniques often make the connection with manufacturing process simulations. In this section we review briefly a few of these techniques.

3.1 Microstructure Parametric Modeling

Exploration of various material microstructures (through microscopic images) demonstrated the complexity of such microstructures (Bargmann et al., 2018). Moreover, those are dependent on the manufacturing process. For example, composites have an inhomogeneous distribution of the fibers in the resin, regarding the curing process. In the case of metallic structure, the way the material is cooled down leads to significant change in the microstructure. It remains massively complex to predict the shape of the microstructure according to the manufacturing process (due to the material state change). Therefore, it is more relevant to trade off on a parametric modeling of the microstructure to measure the effect of slight variations on the mechanical properties.

The challenge is to be able to model and parameterize a large range of microstructures for the various materials. A few key microstructures can be highlighted (see Fig. 35):

- Grain structure, which is observed in metallic (steel, aluminum) or ceramic materials;
- Porous structure, which is relevant for resin with defect (void) or porous foam;
- Long fiber random microstructure with a variable amount of fibers into space.

All those microstructure are defined via a reduced number of parameters for efficient trade-off studies. Moreover, the chosen parameters should be defined with a range identified to ensure that the trade-off delivers realistic microstructures. In the case of composite materials, the volume fraction of fibers in various applications varies from 50% to 60%. Such high volume fraction of fibers is challenging to ensure a sufficient compaction of fibers in the RVE. On the **3D**EXPERIENCE Platform, microstructure parametric modeling enhances the realism of produced microstructures including constraints for symmetry and periodicity.

3.2 Material Calibration

A key ingredient to an accurate finite element solution of structures is the mathematical model of the material. One of the earliest, and simplest, successful material models in solid mechanics is linear elasticity. A linear elastic material

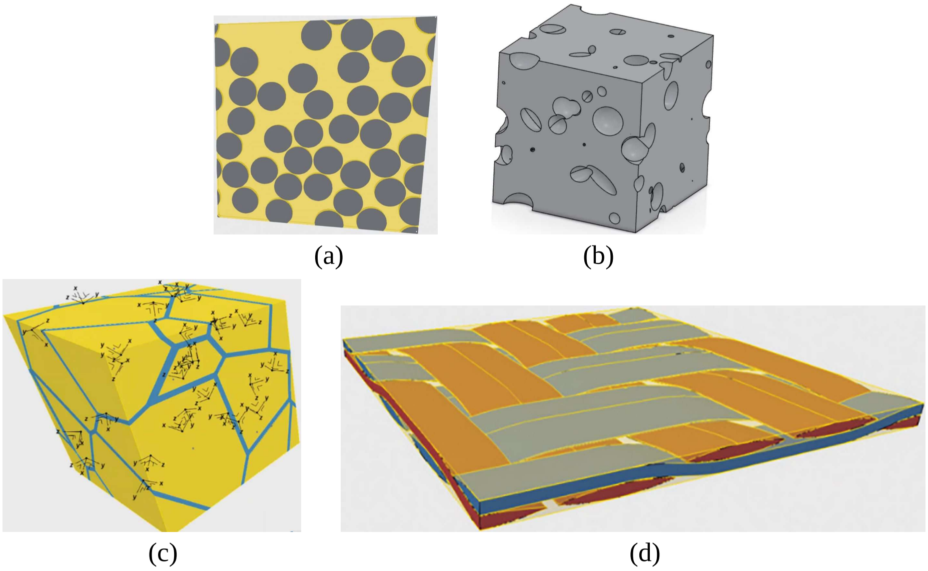
(a) (b)
(c) (d)

FIG. 35: View of various microstructures and their main parameters for several types of structures. (a) Long fiber structure: number of fibers, volume fraction of fibers, minimum distance between fibers; (b) porous structure: volume fraction of pores, shapes of pores; (c) grain structure: number of grains, thickness of grain joint; (d) woven structure: two section shape, number of tows, volume fraction of tows.

models the stress field as being linearly proportional to the strain field. While very effective for small strain deformations, it soon became clear to engineers that a linear elastic material model has a limited range of application, and over the years, many advances have been made in the development of more sophisticated material models. Much of this work is based on testing of material samples and the development of phenomenological material models. Some of the earliest work on metals, investigating elasto-plasticity, behavior under cyclic loading, and behavior across temperatures, strain rates, etc., showed the need for more complex material models as the metal was subjected to more complex loadings. For a constitutive model to be useful in a numerical simulation it must be an appropriate material model for the intended applications. In other words, there is not "one best" material model for any given material.

As more advanced material models, e.g., math models, were developed for FE simulations, the need arose to have software to calibrate these material models. Most material models are a mathematical representation of how the stress relates to the strain, strain rate, time, temperature, etc., in the material. In the material models, there are typically several, or perhaps many, parameters that control these relationships. In this context, we are still thinking of materials that, as engineers, we think of as homogeneous. There may be an underlying microstructure, such as the grain structure in metals, but at the engineering length scale (millimeters and up) we can treat the material as homogeneous. We can test specimens of the material to determine its properties. There is a material model calibration app in the **3D**EXPERIENCE Platform that allows us to determine these material parameters. It does so by using an optimization-based framework to compare the material model response to the underlying test data. Figure 36 shows an example of the material calibration app, performing a calibration for Drucker–Prager plasticity. Once the material model is calibrated, it can be promoted for use by any simulation carried out in the **3D**EXPERIENCE Platform. Since this is occurring within a PLM environment, the underlying test data are stored and archived in a database; the resulting material model is also stored and archived. Traceability and version control are natural parts of the PLM system in which we work.

As we progress to materials that are heterogeneous, materials that are really made from different underlying constituents, one approach might be to model each constituent discretely. Figure 36 shows a multiscale example based around a pneumatic tire in an automobile. The rubber in much of the tire is a complex mixture of rubber and polymeric or metallic reinforcing fibers (plies). As discussed in Section 2.10 you can model the plies in Abaqus using rebar layers. A continual theme running through this is the question of "How much detail can I afford to

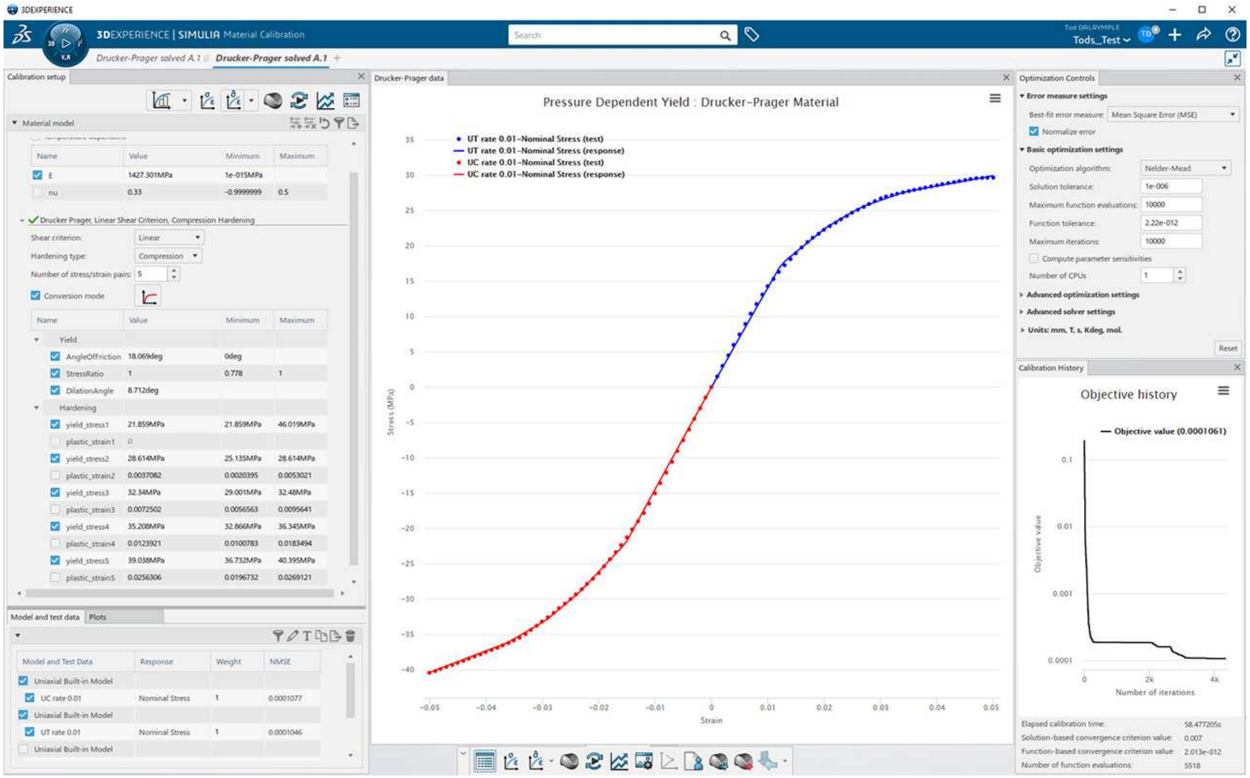
3DEXPERIENCE
3DEXPERIENCE | SIMULIA Material Calibration
Drucker-Prager solved A.1
Drucker-Prager solved A.1
Search
Tod DALRYMPLE
Tods_Test
Calibration setup
Material model
Drucker-Prager data
Pressure Dependent Yield : Drucker-Prager Material
UT rate 0.01–Nominal Stress (test)
UT rate 0.01–Nominal Stress (response)
UC rate 0.01–Nominal Stress (test)
UC rate 0.01–Nominal Stress (response)
Stress (MPa)
35
30
25
20
15
10
5
0
-5
-10
-15
-20
-25
-30
-35
-40
Strain
-0.05
-0.04
-0.03
-0.02
-0.01
0
0.01
0.02
0.03
0.04
0.05
Optimization Controls
Calibration History
Objective history
Objective value (0.0001061)
Objective value
0.1
0.01
0.001
0.0001
0
2k
4k
Number of iterations
Reset
Model and test data
Plots

Name	Value	Minimum	Maximum
☑ E	1427.301MPa	1e-015MPa	
☐ nu	0.33	-0.9999999	0.5

✓ Drucker Prager, Linear Shear Criterion, Compression Hardening

Shear criterion: Linear

Hardening type: Compression

Number of stress/strain pairs: 5

☑ Conversion mode

Name	Value	Minimum	Maximum
Yield			
☑ AngleOfFriction	18.069deg	0deg	
☑ StressRatio	1	0.778	1
☑ DilationAngle	8.712deg		
Hardening			
☑ yield_stress1	21.859MPa	21.859MPa	46.019MPa
☐ plastic_strain1	0		
☑ yield_stress2	28.614MPa	25.135MPa	28.614MPa
☐ plastic_strain2	0.0037082	0.0020395	0.0053021
☑ yield_stress3	32.34MPa	29.001MPa	32.48MPa
☐ plastic_strain3	0.0072502	0.0056563	0.0095641
☑ yield_stress4	35.208MPa	32.866MPa	36.345MPa
☐ plastic_strain4	0.0123921	0.0100783	0.0183494
☑ yield_stress5	39.038MPa	36.732MPa	40.395MPa
☐ plastic_strain5	0.0256306	0.0196732	0.0269121

Model and Test Data	Response	Weight	NMSE
☑ Uniaxial Built-in Model			
☑ UC rate 0.01	Nominal Stress	1	0.0001077
☑ Uniaxial Built-in Model			
☑ UT rate 0.01	Nominal Stress	1	0.0001046
☐ Uniaxial Built-in Model			

Error measure settings

Best-fit error measure: Mean Square Error (MSE)

☑ Normalize error

Basic optimization settings

Optimization algorithm: Nelder-Mead

Solution tolerance: 1e-006

Maximum function evaluations: 10000

Function tolerance: 2.22e-012

Maximum iterations: 10000

☐ Compute parameter sensitivities

Number of CPUs: 1

Advanced optimization settings

Advanced solver settings

Units: mm, T, s, Kdeg, mol.

Elapsed calibration time: 58.477205s

Solution-based convergence criterion value: 0.007

Function-based convergence criterion value: 2.013e-012

Number of function evaluations: 5518

FIG. 36: User interface of material calibration app, Drucker–Prager plasticity example

model?” With each successive generation of computing power, the advent of HPC resources, etc., the answer to this question changes. And yet, today, we cannot afford to model most heterogeneous materials by discretizing their entire subconstituency (in the macrostructural simulation).

We can take the FE-RVE approach, where the morphology of the heterogeneous material is discretely represented with finite elements and the constituent elements are assigned their respective known material properties. This approach often leads to a macro material model that we say is “micromechanics informed.” The FE-RVE can be used in the material calibration app to determine the material parameters of a macro phenomenological material model to capture the overall behavior (if the required level of complexity exists in the macro model).

Or, one can take the mean field homogenization (MFH) approach, where a “material of materials” is defined and the homogenization is performed in the Abaqus FEA solver. The material calibration app supports the calibration of an MFH representation of an elastic fiber embedded in an elastic-plastic matrix. In these situations, one typically has some information about the constituent properties, some information about the fiber morphology, as well as some information from more macroscopic testing. The calibration app can take in all of this information and determine the best constituent material parameters to provide the best match to the macroscopic testing.

3.3 Coarse Graining

A knowledge of underlying material microstructures, such as metal grains or phase separated polymers, can potentially add extra fidelity to FE-RVE representations of the material. Use of simulation to predict microstructure implies the use of course-grained methods, either field-based or bead-based. Where phase-field simulation is used to produce microstructural textures of hard materials such as metal alloys, the allocation of components and phases to use for the simulation input is straightforward. Although potentially complex phase landscapes need to be encoded (for example, by use of CALPHAD databases), the coarse graining arises naturally from the different possible discrete crystal phases occurring in the material. In soft materials and liquids (polymers, solvents, emulsions), however, the allocation of chemical constituents of each coarse-grained bead is not unique. There are constraints through a convenient choice of length scale, but even once this is fixed it is the choice of the practitioner as to how to represent the different chemistries involved. Thereafter careful justification that the coarse-grained system is representative of the underlying material is required. The success of the Martini force field approach is largely due to it providing a simplification to this process—with the practitioner able to refer to a list of chemical functional groups with known water/octanol and water/alkane partitioning free energies that correspond to distinct Martini bead types. To a first approximation the partitioning behavior can be relied upon to capture the necessary physics driving the development of microstructure.

A variety of coarse-graining strategies have been explored. These commonly start from an underlying atomistic representation of the molecules, where conversion into bead allocation is the first task. In general the procedures to assign the topology and parameters can be quite laborious. Materials Studio contains a range of coarse-grained builder tools that streamline the activities associated with coarse graining (see Fig. 37). Bead strings can either be sketched directly or documents containing molecular templates can be used to automatically identify and convert the atomistic sequences into the equivalent bead representation. The second major step is to parameterize a Hamiltonian that can reasonably represent the atomistic level geometry over the set of coarse-grained coordinates with a minimum loss of information. One such route to the Hamiltonian is to sample from an ensemble of states in the atomistic molecular trajectory and employ iterative Boltzmann inversion (IBI).

From a distribution of states $P(q)$ from a set of potentials $U(q)$ in the canonical ensemble,

$$P(q) = Z^{-1}\exp\left(-\beta U(q)\right), \tag{7}$$

the potential $U(q)$ can be constructed by inverting the equation.

$$U(q) = -k_B T \ln P(q). \tag{8}$$

To achieve this simultaneously across all degrees of freedom is the challenge and an iterative approach provides a numerical method to move towards a solution.

$$U_{i+1}(x) = U_i(x) + \alpha k_B T \ln\left[\frac{P_i(x)}{P_{\mathrm{target}(x)}}\right], \quad i = 0, 1, 2, \ldots\ . \tag{9}$$

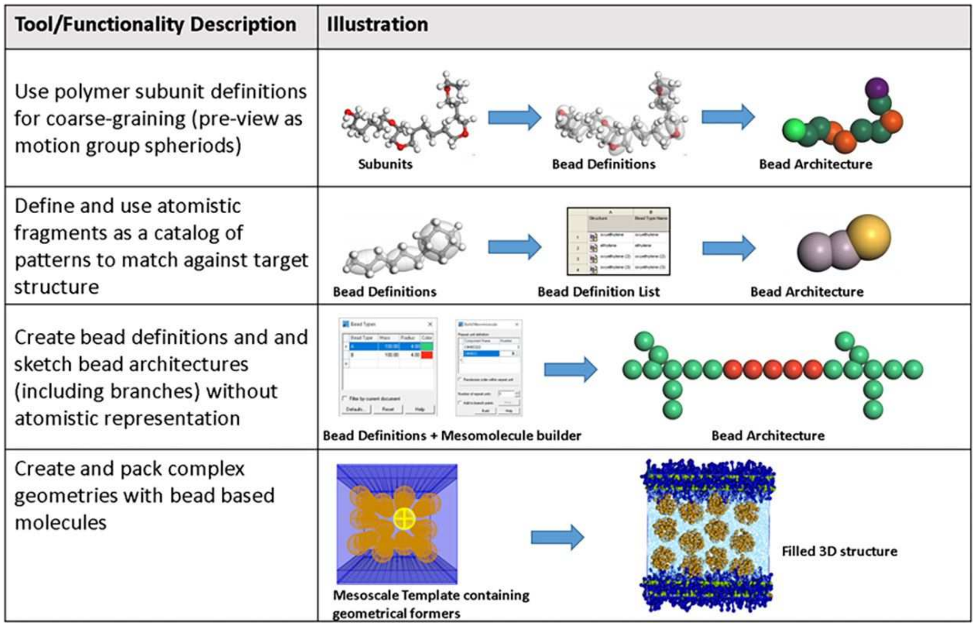

Tool/Functionality Description	**Illustration**
Use polymer subunit definitions for coarse-graining (pre-view as motion group spheriods)	Subunits Bead Definitions Bead Architecture
Define and use atomistic fragments as a catalog of patterns to match against target structure	Bead Definitions Bead Definition List Bead Architecture
Create bead definitions and and sketch bead architectures (including branches) without atomistic representation	Bead Definitions + Mesomolecule builder Bead Architecture
Create and pack complex geometries with bead based molecules	Mesoscale Template containing geometrical formers Filled 3D structure

FIG. 37: Illustration of tools aiding coarse-grained model building in Materials Studio

Scripts to convert atomistic trajectories, apply IBI, and output the coarse-grained force-field file are available to run within the Materials Studio environment which significantly reduces this burden of coarse graining. Extensions of these schemes, IBI, and generation of potentials using machine learning algorithms are a topic of ongoing research (e.g., Joshi and Deshmukh, 2021).

With complex molecular geometries constructed and an appropriate Hamiltonian generated, a further task is to create a starting condition for the condensed phase. For structures such as bilayers, micelles, and vesicles, self-assembly during coarse-grained molecular dynamics or dissipative particle dynamics could be used. In practice this is slow and leads to imperfectly ordered structures. Tools for constructing arbitrarily complex mesostructures from templates are an efficient way to create starting configurations. Each former template can be filled with any combination of coarse-grained particles using the graphical interface options or by automated procedures.

3.4 Results Mapper

Mapping is usually an essential step in the workflows, modeling composites with multiscale approaches. Characteristics of the microstructure can be the result of the manufacturing process and need to be taken into account in the subsequent analysis. For example, fiber orientations in the composite can be computed in a flow simulation that uses boundary layers to capture the sharp gradient near the flow boundaries. The subsequent structural analysis usually uses a more uniform mesh and the mesh resolution is determined based on the mechanical response of the part under a particular service load. Due to the focus on different physics, dissimilar meshes are usually used in the two analyses.

Abaqus has a built-in mapper that automatically maps fields between dissimilar meshes. Both scalar and tensor fields can be mapped and invariants of the tensor fields are preserved during mapping. Figure 38 shows the mapped fiber orientation in an injection molded engine cover part. The injection molding simulation is performed with the plastics app in the **3D**EXPERIENCE Platform and the subsequent analysis is performed with Abaqus.

4. MULTISCALE MATERIALS APPLICATIONS BY MATERIAL CLASSES

It is not the purpose of this section to perform a comprehensive review of the existing literature regarding the commercial software packages leveraged in materials science/ICME endeavors. Quick Google Scholar searches show tens of thousands of pieces of research work, some attached to patents filed based on them.

Instead, we review a few representative applications grouped (loosely) by the type of material. As usual with software vendors we are most often not allowed to present industrial applications that we have worked and hence the examples below, while representative, are a subset of the public domain literature that we were engaged in. We start with a brief and nonexhaustive review of examples of researchers across the world utilizing some of our general purpose software packages (e.g., Abaqus, Materials Studio) for ICME activities. Some examples in polymers, metals, porous natural materials, and biological materials are briefly reviewed afterward.

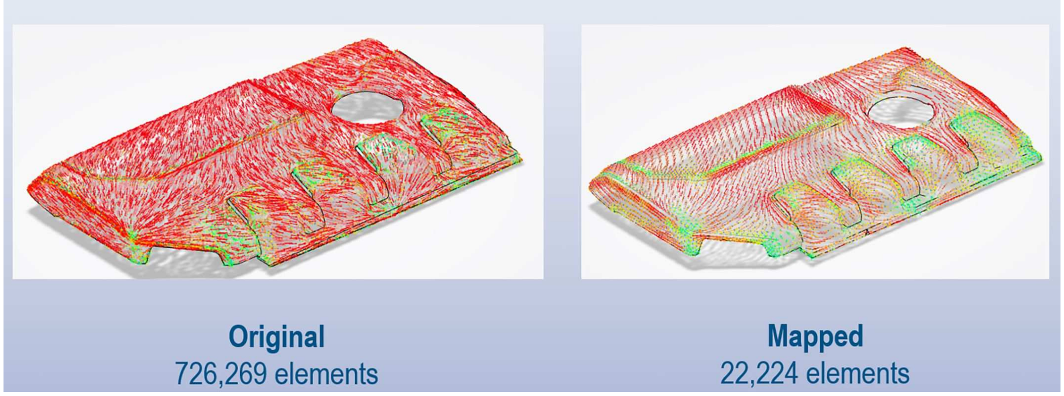

FIG. 38: Fiber orientation mapping between subsequent analyses

4.1 Comprehensive Research Activities (Using Dassault Systèmes Tools)

Abaqus and Materials Studio are important and heavily used simulation tools for multiscale material studies. A quick search on *Abaqus multiscale* in Google Scholar yields almost 14,000 hits, while a search on *Materials Studio* yields over 9000 hits.

Following are a few examples from the literature.

The use of Abaqus for nanotechnology applications was explored by Li et al. (2008). Atomistic RVEs were linked to a continuum model via a generalized mathematical homogenization (GMH). GMH was extended to support many-body potentials and was seamlessly integrated with Abaqus for coarse-scale computations with molecular dynamics code.

Fish and Yuan (2005, 2007) used Abaqus for the development of multiscale enrichment based on partition of unity (MEPU) with an objective to extend the range of applicability of mathematical homogenization theory to problems where scale separation may not be possible. MEPU enriches PDEs with fine-scale features and quasicontiuum formulations with relevant atomistic data. Boundary layers, nonperiodic fields, and nonlinear systems were accounted for, extending the range of applicability of MEPU to nonlinear nonperiodic systems with inseparable fine and coarse scales.

Li et al. (2021) used Abaqus as part of a general computational framework, along with the generalized finite element method (GFEM) and iterative global-local cosimulation (IGL), for multiscale analysis of localized defects in large complex structures. The IGL component provides a two-way coupling between the macroscale Abaqus model and the local GFEM models. They showed examples of localized plasticity around the holes in plates, a hat-stiffened panel, and a welded T-joint with a propagating crack.

In a study of parameter uncertainty for integrated computational materials engineering (ICME) workflows, Whelan and McDowell (2019) established guidelines for using groups of statistical volume element (SVE) simulations to cope with uncertainty in the calibration of material properties. In this workflow, a crystal plasticity model of Ti64 that took into account small-scale 3D slip geometry, dislocation structure, and crystallographic texture was implemented in an Abaqus UMAT. A careful calibration study, including a parameter sensitivity analysis was performed and the simulation results were compared to a baseline from the literature.

Lu et al. (2021) studied the slurry flow of compressible biomass particles in Abaqus/Explicit. They implemented an eight-parameter continuum material model to capture both the quasistatic shear and dynamic flow behavior of the slurry. The material response was implemented in an Abaqus VUMAT. They chose a continuum approach over a particle method, such as DEM, because of the computational savings the continuum approaches offered. They validated their model against experimental results for a quasistatic shear flow and dynamic flow through a hopper.

Some researchers have combined the capabilities of Abaqus and Materials Studio for sophisticated multiscale simulations.

Saavedra Flores et al. (2011) paired Abaqus and Materials Studio to study the tensile response of single-walled carbon nanotubes (SWCNTs). Materials Studio was used to determine material constants for a hyperelastic strain-energy density potential for a subsequent Abaqus simulation.

In Shi et al. (2009) the authors used Abaqus and Materials Studio in a vibration analysis of single-walled carbon nanorings. For the simulation, the authors implemented an Abaqus user-defined element (UEL) based on the so-called atomic-scale finite method (AFEM). The UEL took into account the microstructure of the carbon nanotube. Abaqus was used to carry out the vibration analysis and the results compared to another set of results computed using Materials Studio.

4.2 Polymers

4.2.1 Bridging the Scales: From Molecular Dynamics to Product

Most materials have some complexity of structure at the nano- or microscale that influences their behavior at the continuum level. To enable continuum models to be built that capture this complexity it is necessary to bridge the gap between molecular scale models and the continuum. The approach is likely to be particularly helpful for simulations of composite materials and materials involved in additive manufacturing processes. Classical and mesoscale simulations based on molecular structure can be used to predict key properties, including cohesion and wetting, mechanical behavior, diffusion, adhesion at surfaces, and phase separation. Such simulations can be leveraged in finite element (FE) simulations through homogenization of the predicted material structure and through use of the simulated material properties for FE input. In this section, we will work through and extend one particular multiscale workflow starting with the construction and characterization of a thermoplastic copolymer at the atomistic level and ending with a macroscopic part level simulation.

4.2.1.1 Background

There is a long history of trying to understand continuum level material behavior by looking more closely at the material's nanostructure. Molecular and mesoscale dynamics simulations based on classical equations of motion are ideally suited for studying the structure and properties at this scale, but it is not entirely straightforward to use the results directly within finite element models. Our goal is to describe a suitable workflow for bridging the gap between the very fine-grained work at the atomic/molecular level, working through a "meso" scale simulation level, and finally obtaining continuum level material behavior for use in finite element (FE) simulations of real components. Mesoscale, or coarse-grained, representations of the systems are required as part of the scheme to enable structural information to be captured at the 10–100 nm level, since atomistic level simulations normally operate at smaller scales. We will highlight the process of moving from molecular dynamics (MD) simulations to mesoscale, to FE scale using a polyurea copolymer melt as a concrete example. In recent years, polyurea has been studied extensively, at the molecular level (Grujicic et al., 2010, 2011; Fermemglia and Prici, 2009), as well as at the continuum level through traditional testing of material specimens (Yi et al., 2006). Grujicic et al. (2010, 2011) outlined many of these ideas and tied together the significant scales for the polyurea material. We follow the general methodology of Grujicic et al., using some of the conclusions, but also extend the discussion around finite element modeling through the use of FE-RVEs, homogenization methods, and the derivation of a continuum-level material model. A key reason to study polyurea, as observed by Grujicic et al. (2010, 2011), is that it possesses a complex nanometer-scale material structure. This consists of hydrogen-bonded discrete hard domains, with high glass-transition temperature (T_g), and domains of soft (low T_g) matrix. The mechanical properties of this and structurally related thermoplastic polyurethane materials are determined by the details of the distribution of hard and soft segments. In the first instance we will focus on the individual mechanical behaviors of the hard and soft segments and on the prediction of phase separation between hard and soft segments to form the combined microstructure, also called morphology, or texture. By studying materials at all of these length scales a whole new field has emerged, termed ICME—integrated computational materials engineering. The goal of ICME is to enable the development of new materials, with superior performance, by tailoring the microstructure and processing with knowledge at each length scale.

4.2.1.2 Molecular Scale

The most accurate simulation of matter at the molecular level requires the determination of electronic structure using quantum mechanical theory. However, for treatment of polymers this level of detail is not often required. This is the case here, since the first objective is to predict elastic moduli and yield strain of the polymer constituents, which depends more on the statistical sampling of the polymer configurations and the average forces experienced by each atom, than the internal electronic configuration. The response of each atomic center is instead approximated by a combination of classical potential energies which provide the averaged atomic forces. This simplification allows tens or hundreds of thousands of atoms to be simulated within a 3D periodic simulation cell that represents the polymer melt. To start with, hard and soft polymer segments for the polyurea structure were sketched within BIOVIA Materials Studio (2021) modelling software, as outlined in Fig. 39, and then amorphous cells of each component were constructed by packing multiple chains into cells such as shown in Fig. 40. These form the basis for prediction of the elastic response of domains of hard segments and soft segments (treated separately). This is carried out with the goal of furnishing the nodes within an RVE or continuum model with input based on this first principles property prediction of the material present at each node.

To sample representative polymer configurations Newton's equations of motion are used to evolve the system. This method, termed molecular dynamics (MD), can be coupled to thermostats and barostats to sample configurations

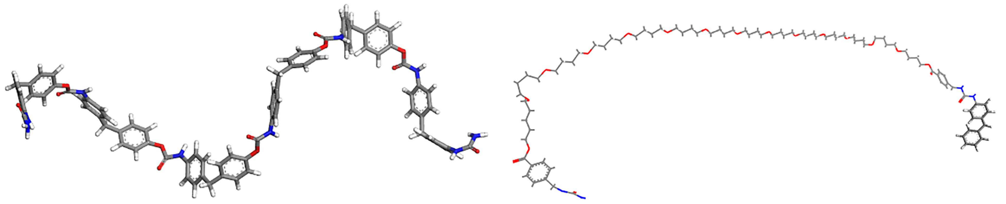

(a) (b)

FIG. 39: Molecular structure of (a) hard segment (b) soft segment material

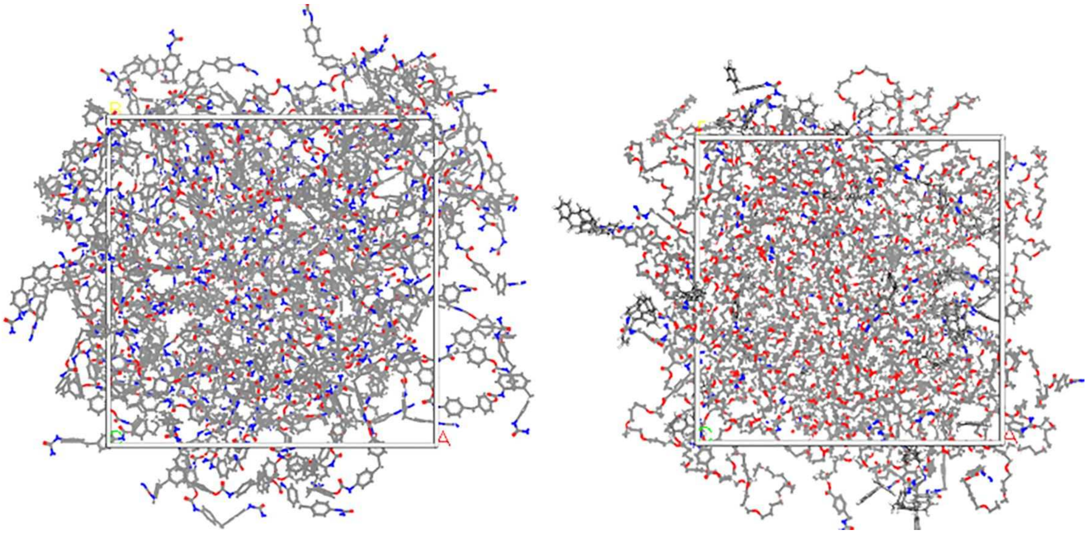

(a) (b)

FIG. 40: Amorphous boxes (5 nm per side) of pure component (a) hard segment, (b) soft segment material

from a range of statistical thermodynamic ensembles, and to obtain a range of thermomechanical property predictions. Here the cells were subjected to constant N (number of atoms), constant P (pressure), and constant T (temperature) MD which equilibrates the system to a natural density based on, in this case, atmospheric pressure and room temperature. The quality of the model depends critically on the classical potential energy describing interactions between atoms. In this work we applied the COMPASS II force field (Sun et al., 2016) which is extensively validated for prediction of a wide range of properties and materials, including polymers.

4.2.1.2.1. Mechanical Property Prediction

Once equilibrated amorphous cells were constructed, a procedure to extract the yield strain and Young's modulus was applied. The methodology chosen was to strain the simulation box and extract the resulting stress in order to construct a stress-strain response curve. This was achieved through application of a scripted procedure to apply compression at a strain rate of 2×10^7 s^{-1}. Engineering stress was computed using components of the stress parallel to the compression direction and collected every picosecond in simulations running for 1 ns per strain. Stress/strain response curves for each system were averaged over eight separate amorphous configurations in order to reduce the standard error in stress at each strain. Figure 41 shows consolidated stress-strain curves for both segment types.

It is important to recognize that the equivalent strain rate for this compression is significantly higher than an experimental procedure. Consequently we do not expect a quantitative prediction of the Young's modulus and yield stress and strain until a strain rate dependence is explored. The values here were used to provide a first estimate in the optimization procedures outlined in the following sections. They also provide an order of magnitude estimate for the difference between hard and soft segment properties.

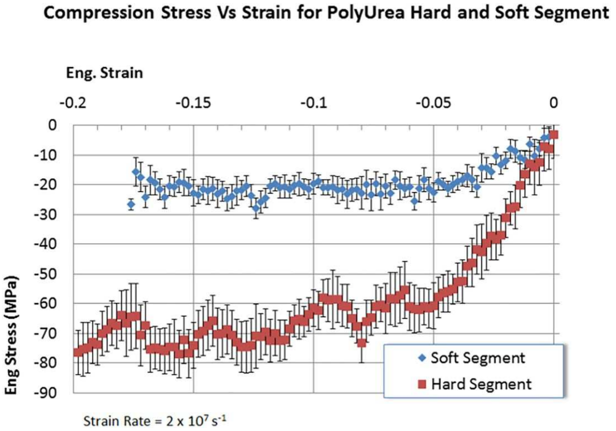

FIG. 41: Average stress-strain response in compression for the hard and soft segments

An alternative to use of mechanical property averages to describe the properties of the RVE node is to generate the average Cauchy stress at each node directly from the molecular simulation as described in more detail in Choi et al. (2016). This will be explored in future work.

4.2.1.3 Mesoscale

The second objective of the molecular level simulation was to provide a first principles prediction of the underlying morphology of the copolymer. The size of such textures is typically on the order of 10–100 nm, which precludes the use of atomistic level simulations. The number of particles that would need to be incorporated and the relaxation times required to reorient polymers into their thermodynamically preferred configuration is prohibitively large compared to that accessible by atomistic level calculations. Consequently it is necessary to coarsen the representation of the material. Several methods exist for achieving this, ranging from united atom treatment, where heavy atom centers simply incorporate the effect of attached hydrogen atoms, to dynamical density functional methods, in which the polymers are represented as density distributions generated by idealized Gaussian chains exposed to external potentials. Coarse-grained molecular dynamics has recently grown in popularity, where typically four heavy atoms are represented at each center. This allows time steps to be increased 10- or 20-fold from a typical 1 fs in atomistic calculations. However, we have chosen a dissipative particle dynamics (DPD) methodology, which uses soft potentials as opposed to those with highly repulsive hard-core potentials at close contact. This delivers time steps of several picoseconds and morphology predictions that evolve in relatively few iterations.

In DPD calculations the key driving force for phase separation between polymer components is an interaction parameter α_{ij} that according to Groot and Warren (1997) is closely related to the Flory–Huggins χ parameter via Eq. (10).

$$\alpha_{AB}(\rho = 3) = 25 + 3.50\chi. \tag{10}$$

In a Flory–Huggins treatment, larger values of χ drive stronger phase separation. In this work Hildebrand solubility parameters were used to provide an estimate of χ as per Eq. (11).

$$\chi = \frac{\nu}{k_B T}(\delta_A - \delta_B)^2, \tag{11}$$

where Hildebrand solubility parameters are related to cohesive energy density by $\delta = \sqrt{E_c/V}$. The cohesive energy density of each of the hard segments (273 MPa) and soft segments (70 MPa) was measured from the atomistic amorphous cells described in the last section and resulted in $\chi = 5.2$ and consequently $\alpha_{ij} = 44$.

The definition of a mesoscale bead followed Grujicic et al. (2010, 2011) in assigning the equivalent of three C4H80 units (a mass of 73 amu). This results in a bead radius of 1 nm, defining the length scale of a simulation cell. The polyurea molecule is represented by the simplified representation of Fig. 42. The DPD morphology prediction is

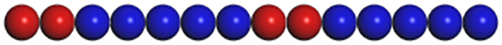

FIG. 42: Mesoscale bead representation of polyurea molecule. Hard segments in red (lighter) and soft segments in blue (darker).

shown in Fig. 43 and shows the minority hard segment phase separated into domains of several nanometers across. Although difficult to see from the pictorial representation, the phases are elongated and somewhat interconnected. This detail potentially introduces new information into FE calculations described below which must otherwise assume idealized hard segment inclusions.

4.2.1.4 Continuum, FE, or Macroscale

4.2.1.4.1. FE-RVE Macroscale

The idea of a representative volume of material has been around for decades and predates FE codes. There is a Wikipedia entry on “Representative elementary volume” that gives a reference to a 1963 paper by Hill (1963). Work in the 1920s on estimating the elastic modulus of an aggregate by averaging elastic stiffnesses (Voigt, 1928), or by averaging elastic compliances (Reuss, 1929), is also related to the idea of a representative volume of material. Researchers and engineers have been studying the microstructure of materials under a microscope (and X-ray, and μCT scan, etc.) for decades (Boyce et al., 2001; Schrader, 2005), and using that insight to help determine material properties based on constituent behaviors. With the advent of FE software, researchers have been studying the effect of microstructure, or morphology, by using RVEs (sometimes called the RUC representative unit cell) for the last several decades.

Our work using MD tools has given us some insight into the mechanical behavior of the soft and hard segments, and the morphology of the material. Figure 43 shows how we can convert the morphology, as determined from DPD, into an FE-RVE. With the RVE, and some appropriate periodic boundary conditions, we can subject the FE-RVE model to one or more types of loading (uniaxial tension, simple compression, etc.) (Oancea et al., 2016). If we have high confidence in the soft and hard segment material properties, the RVE macro response ought to match some traditional macro test data. Following the lead of Grujicic et al. (2010, 2011) we will compare to the test data from Yi et al. (2006). Alternatively, we might use the material properties determined from the MD simulation as an initial guess and perform some parametric optimization to determine the final constituent material behaviors. Grujicic et al. (2010, 2011) proposed that the soft segment material should be nonlinearly elastic (hyperelastic), and that the hard segment should be viewed as elasto-perfectly-plastic. They also gave specific material model parameters for the soft and hard segments.

4.2.1.4.2. Parametric Optimization Using the FE-RVE

While the Grujicic paper concluded that the soft segment should be modeled as hyperelastic and the hard segment as elasto-perfectly-plastic, there is plenty of room to argue the merits of that conclusion. For instance, polyurea has

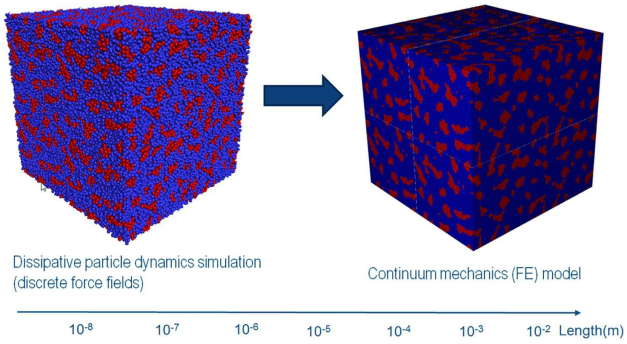

FIG. 43: Conversion of mesoscale morphology into FE mesh

been studied extensively because of its ability to attenuate shock waves from blasts (Grujicic et al., 2010, 2011), and macro level testing has shown the material to be very rate sensitive (Yi et al., 2006). At this point in time, the MD and mesoscale tools provide insight into the constituent behavior, though they are perhaps open to interpretation. We still need to use all available information, including the test data from the macroscale, to guide us in developing the best material representation. We also make use of an idea from the papers by Qi and Boyce (2004, 2005), "Based on the concept of amplified strain, Mullins and Tobin (1957) suggested that the softening in rubber vulcanizates was due to the decrease of volume fraction of the hard domains with strain, as a result of conversion of the hard domains to the soft domains." For the current work, we will follow the lead of Grujicic for the constituent behaviors, with the small addition that we will allow the elastic-plastic behavior of the hard segment to exhibit strain softening. Within this context, we then perform a parametric optimization using the general purpose Isight optimization tool to best define the underlying constituent material models. The optimization tools drive many Abaqus runs of the RVE model, with the material parameters of the soft and hard segments as our design variables. The RVE stress-strain result is compared to the macrolevel test data, and the difference is used to construct our objective function for minimization. The result of this optimization process is shown in Fig. 44. The RVE response matches the test data quite well. The resulting material parameters for the soft and hard segments are also shown in Fig. 44.

The beauty of the FE-RVE is that it captures the morphology of the microstructure with good accuracy and allows us to investigate "what-if" scenarios with the underlying constituent behaviors. The downside to the FE-RVE is that it is still not useful for performing component FE analyses.

4.2.1.4.3. Homogenization to Macroscale

Using the RVE, with its accurate portrayal of the microstructure, we can study how the constituent behaviors influence the macro response. But in order to perform FEA at the component level it would be difficult to use the RVE. We can approximate the macro behavior by analytical mean field homogenization (MFH) methods. There has been over a decade of work putting MFH methods into FE frameworks. Recently, the Abaqus software has been extended natively to include a few types of mean field homogenization. A composite material can have one level of recursion, defining itself through a hominization of other materials, with a keyword interface such as shown in Fig. 45.

The above example says that the material named polyurea is made up of two constituents; the homogenization method is Mori–Tanaka, and the inclusion shape is prolate (ellipsoidal). Hopefully, one can see the similarity with the earlier RVE approach. In each approach we define the constituent properties explicitly. In the RVE, the microstructure is defined explicitly with individual elements. In the MFH approach, the microstructure is approximated by saying that the hard segment inclusion is ellipsoidal in shape and makes up a certain volume fraction (in the case of our polyurea, the volume fraction is 0.287). There are a number of studies in the literature that compare the RVE, with its exact microstructure depiction, to various mean field homogenization techniques, for example, Klusemann and Svendsen (2010). The mean field homogenization based material model can now be used in component level simulations. A future activity is to study the relative performance of this approach.

4.2.1.4.4. Developing a Macroscale PRF Model

So far, we have gained insight into the macrolevel behavior of polyurea from testing and the microlevel from MD level investigations. Following Grujicic, we have postulated that the soft segment and hard segment constituents might be

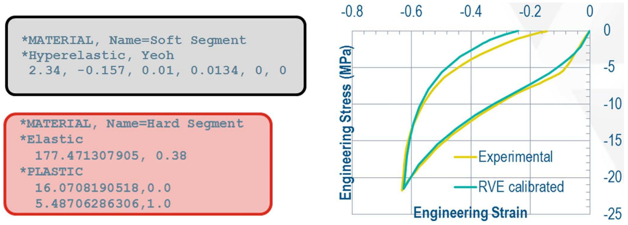

```
*MATERIAL, Name=Soft Segment
*Hyperelastic, Yeoh
 2.34, -0.157, 0.01, 0.0134, 0, 0
```

```
*MATERIAL, Name=Hard Segment
*Elastic
  177.471307905, 0.38
*PLASTIC
  16.0708190518,0.0
  5.48706286306,1.0
```

FIG. 44: Results of parametric optimization of the soft and hard segment FE-RVE model [experimental data: Yi et al. (2006)]

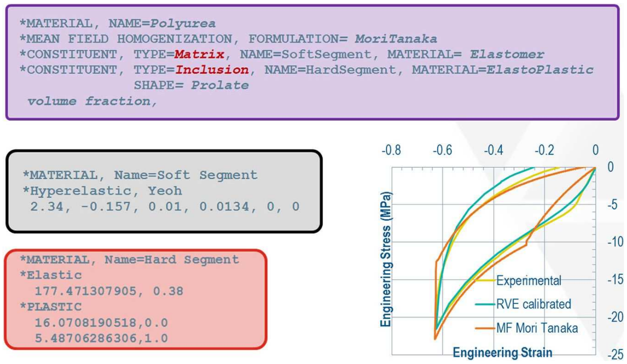

```
*MATERIAL, NAME=Polyurea
*MEAN FIELD HOMOGENIZATION, FORMULATION= MoriTanaka
*CONSTITUENT, TYPE=Matrix, NAME=SoftSegment, MATERIAL= Elastomer
*CONSTITUENT, TYPE=Inclusion, NAME=HardSegment, MATERIAL=ElastoPlastic
                 SHAPE= Prolate
 volume fraction,
```

```
*MATERIAL, Name=Soft Segment
*Hyperelastic, Yeoh
 2.34, -0.157, 0.01, 0.0134, 0, 0
```

```
*MATERIAL, Name=Hard Segment
*Elastic
  177.471307905, 0.38
*PLASTIC
  16.0708190518,0.0
  5.48706286306,1.0
```

FIG. 45: Definition of the polyurea material by mean field homogenization [experimental data: Yi et al. (2006)]

modeled as hyperelastic and elasto-plastic, respectively. Work with both an FE-RVE and mean field homogenization have established some reasonable constituent material model parameters. For practical applications, we may want to have a traditional continuum-level material model. Grujicic speaks to this, but says "Derivation of such a homogenized material constitutive model is beyond the scope of the present work" (Grujicic et al., 2011).

As we look at possible native continuum-level material models in Abaqus, a likely candidate for modeling the combination of behaviors we see in polyurea is the parallel rheological framework (PRF) model. This material model is intended for polymers and is a two- or more network model that may include nonlinear elasticity, plasticity, and viscoelasticity in the various networks (Fig. 46).

The depiction shown here of the PRF model shows two networks—the zeroth network is elastic-plastic and the first network is elastic (in general the additional networks may also be viscoelastic, but in this case we will set the viscous parameters to near zero. Our target material model is a combination of an elasto-plastic network, and an elastic network. We do some basic math on the initial slope of the stress-strain curve to determine the total elasticity (input as *Hyperelastic), and the network 0 and network 1 contributions to that total. In the Abaqus key word line we have

***VISCOELASTIC**, **NONLINEAR**, **NETWORKID =** 1, **SRATIO =** s1, **LAW =** strain

The SRATIO value of s1 gives that fraction of the total elasticity in network 1. Using the incompressible relation, E = 6*C10, the network 1 contribution to the initial stiffness is 9 MPa. Since the total stiffness is $\sim$ 65 MPa, then the network 0 contribution must be about 56 MPa. SRATIO is then $\sim 9/65 = \sim 0.14$. Our first guess at the plasticity yield stress is 5 MPa. After a bit of fine-tuning of the parameters, we can achieve a PRF macromodel that matches the polyurea test data quite well; see Fig. 47.

4.2.1.5 Summary and Next Steps

Researchers have studied the microstructure of materials for decades to get a better understanding of the macrolevel mechanical properties. There is a growing capability using atomistic modeling of materials to study both the microstructure and constituent behaviors from first principles. This paper has taken an earlier work on polyurea, repeated

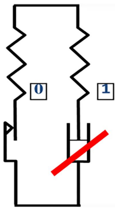

FIG. 46: Target PRF material model, two networks

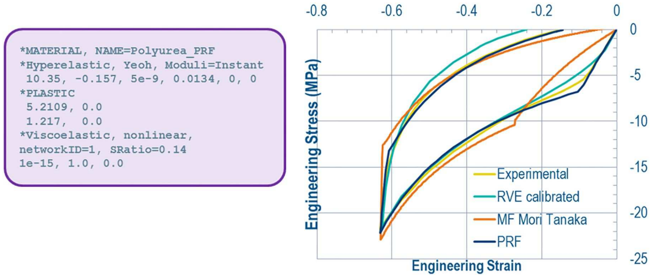

```
*MATERIAL, NAME=Polyurea_PRF
*Hyperelastic, Yeoh, Moduli=Instant
 10.35, -0.157, 5e-9, 0.0134, 0, 0
*PLASTIC
 5.2109, 0.0
 1.217,  0.0
*Viscoelastic, nonlinear,
networkID=1, SRatio=0.14
1e-15, 1.0, 0.0
```

FIG. 47: Comparison of the RVE, MFH, and PRF material models [experimental data: Yi et al. (2006)]

some aspects of that work, and extended the story. We have shown how to use MD simulations to investigate the microstructure and the constituent behavior. Then we have shown how one can bridge the gap between the microlevel and macrolevel. Using an FE-RVE, we can bridge the gap and use FE tools to further investigate and optimize the constituent behavior. The FE-RVE captures the morphology of the microstructure with good accuracy and allows us to investigate "what-if" scenarios with the underlying constituent behaviors. The downside to the FE-RVE is that it is still not useful for performing component FE analyses. One can also use FE-based mean field homogenization methods to bridge the gap between micro to macro levels. The typical MFH methods idealize the inclusions as simple geometries such as spheres, ellipsoids, etc., so detailed information about microstructure may be lost. We imagine that if the actual microstructure is relatively simple, then perhaps the MFH technique can render reasonable accuracy and reasonable computational performance for component level analyses. For the polyurea, the hard segment inclusion was of a relatively simple geometry, so the MFH has been successful.

Future work will include studying the performance of the MFH technique for component FE simulations, and may include revisiting the original assumption about the constituent behavior. Since we know that polyurea is a highly rate-sensitive material, it would seem natural to suppose that one or both of the constituents contribute a viscous behavior. It would be quite interesting to see if we can postulate some viscous contribution at the constituent level and repeat the process outlined in this paper, thus attempting to match the macrolevel testing that shows the rate-sensitive behavior.

4.2.2 Polymer-Based Laminate Composites

Composite materials are widely used in a various range of industries for their relevant stiffness and strength performances. Polymer-based composites typically include glass fibers (glass fiber reinforced polymers—GFRPs) or carbon fibers (carbon fiber reinforced polymers—CFRPs). Recent applications in the aerospace industry make heavy use of CFRPs for structural components. A variety of manufacturing techniques are used, including hand-layup processes for prototypes and automatic process such as AFP, ATL, and ADM for production. The different processes can lead to significant differences in the performances due to the quality and homogeneity of the microstructure created for each layer. Numerous studies have been conducted on composite multiscale modeling and simulation. In fact, microstructure of composites can be easily modeled and idealized at first sight. Throughout the 1970s, the emergence of composites led to various studies to propose homogenization methods using the Eshelby inclusion solution. The Mori–Tanaka model or composites cylindrical assembly (CCA) (Hashin, 1983) have been suggested and considers the microstructure as a resin material containing an inclusion (spherical or cylindrical). Those analytical models offer the ability to be immediate with no simulation delay (FEM generation/solver computation).

However, such analytical model does not provide stress distribution between resin and inclusion, which makes it difficult to identify the strength properties of the microstructure. FE-based RVEs are then suggested with representation based on the real microstructure.

The idealization can be then used in a finite element study (Fig. 48). The hexagonal packing model is the most used for the orthotropic transverse behavior (E2 = E3). Such FE-RVE provides results in agreement with the Eshelby inclusion analytical approach for homogenized properties and the stress distribution between fiber and resin and the interface between fiber and resin. For strength properties, stress distribution between fiber and resin is highly sensitive

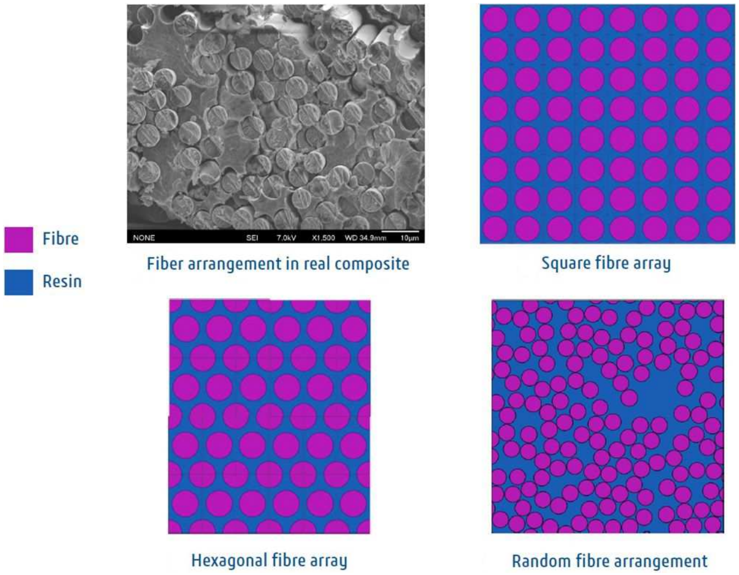

FIG. 48: View of idealization of microstructure for hexagonal, square and diamond microstructures

to the distance between fibers. Therefore, advanced modeling is required to take into account the variability of the distance between fibers due to real arrangement. Various studies exist to model the microstructure using random algorithms to distribute the fibers into the space. One of the key challenges is the ability to randomly distribute the fibers with a high volume fraction of fibers (usually varying from 50% to 65%). This type of modeling challenge has been partially responded to by several studies (Ballard et al., 2014; Omairey et al., 2019). Using the advanced modeling capabilities of the **3D**EXPERIENCE Platform, the random distribution of fibers over the microstructure is carefully considered. The fiber diameter for carbon fibers is about 5 µm. A baseline RVE model distributes the fibers in the volume randomly. This baseline defines a reference stress distribution between fibers and resin. According to the literature, it has been observed that the fiber diameter varies slightly. The diameter variation is used to update the random RVE. Stress concentration changes accordingly. Moreover, regarding the supplier, the shape of the fibers can be different with an elliptic section. This leads to a significant variation of the stress concentration and failure propagation. All three types of structures are shown in Fig. 49.

Both the analytical model and the FE-RVE models use material properties which are defined from lower-scale studies (for example, for the resin at nanoscale using Materials Studio) or from physical tests. On the other hand, for the fiber, physical tests are mostly impossible for a certain amount of properties (transverse stiffness and strength,

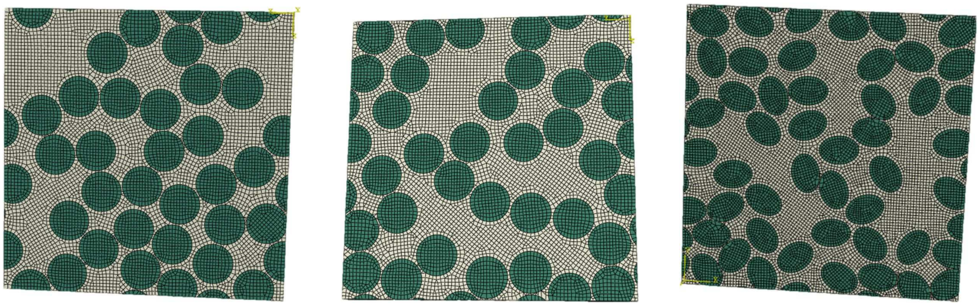
(a) (b) (c)

FIG. 49: Automatically generated fiber arrangements—diameter and shape/orientations. (a) Baseline with single fiber diameter; (b) variation with variable fiber diameter; (c) variation with elliptic shape orientation.

in-plane shear stiffness,strength, etc.). For advanced predictions of the behavior of composite structure, multiscale must be considered for analysis. This is the case for compressive strength which is due to the buckling of fibers due to the initial misalignment (Mechin et al., 2019, 2020). The initial misalignment is due to the curing process leading to different thermal expansion of material (fiber and resin) at the cooling step. The initial misalignment accelerates the buckling of fibers, but the buckling is contained by the resin. The stiffer the resin, the later the buckling occurs. Such real defect can be modeled in RVE microstructure. The use of RVE complex modeling helps to accurately identify the effect of the curing process and the residual properties (Sun et al., 2017).

4.2.3 Defects and Damage in Composite Laminates

Composite materials exhibit a significantly higher energy absorption capacity per unit weight than metallic structures. This has contributed to the increased adoption of composite materials as energy absorbers in the aerospace, automotive, and railway industries. The ability to simulate accurately the crushing response of composites (and their energy absorption mechanisms) can reduce significantly the product development cycle and cost, avoiding laborious and costly experimental testing. The work in Sokolinsky et al. (2011) describes a physics-based Abaqus/Explicit simulation of a corrugated carbon–epoxy fabric composite plate subject to quasistatic crushing. The corrugated plate was developed and tested by the CMH-17 Crashworthiness Working Group (CMH-17, 2008). The objective of the simulation was to predict the specific energy absorption (SEA) of the material using a microstructure informed finite element model that accounts for both delamination and in-plane failure of fabric-reinforced composite plies. The Ply-Fabric model in Abaqus (a structured-based constitutive model for woven reinforced composites) was used to model the in-plane response of the fabric-reinforced plies, and the surfaced-based cohesive contact capability in Abaqus was used to describe the delamination response of the composite plate.

Sokolinsky et al. (2011) shows different views of the deformed shape of the corrugated plate at the end of the simulation. The simulation reproduced important characteristic features of the crushing response of woven composites, such as the frond formation in the composite plate, the propagation of the main delamination through the plate, and the accumulation of debris between the loading rig and the composite plate. The images in Fig. 50 show very good qualitative correlation between the experimental and numerical results.

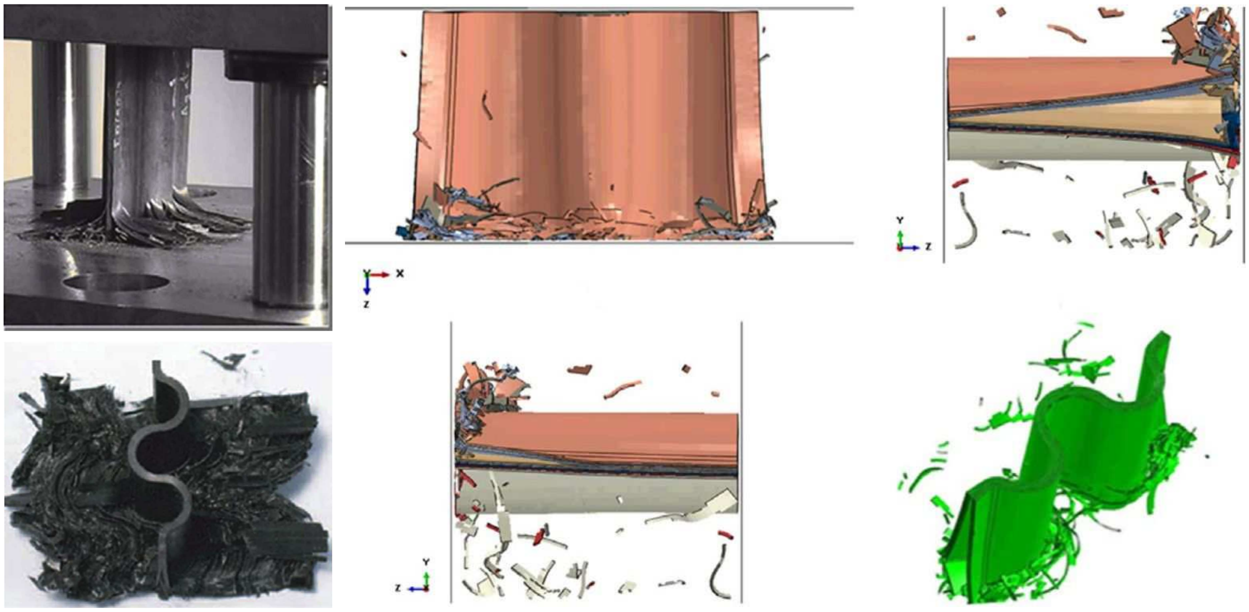

(a) (b)

FIG. 50: Different views of the deformed shapes of the corrugated composite plate. (a) Experimental result; (b) numerical result.

Figure 51 shows a comparison of the load-displacement curves. Both the peak and average crush forces were predicted accurately. A comparison between the experimental and numerically predicted specific energy absorption (SEA) of the corrugated plate is also shown in Fig. 51, and show good agreement, especially in the second half of the crushing process. The largest discrepancy between the results is observed at the early loading stages when the chamfer part of the plate is crushed. Taking into consideration the extremely complicated nature of the crushing process, the overall correspondence between the measured and simulated SEA curves is judged to be acceptable.

The results of the Abaqus/Explicit simulations show very good quantitative and qualitative agreement with the experimental data, thus demonstrating that the methodology and tools are applicable for realistic crush simulations of composite structures. This enables substitution of costly experimental testing with numerical simulation for the crashworthiness design of composites.

The LaRC05 criterion is one of the overall top rated damage criteria by the World Wide Failure Exercise via blind prediction benchmarks for unidirectional fiber-reinforced composites (Kaddour and Hinton, 2013). LaRC05 is a micromechanics-based damage initiation criterion developed by Pinho et al. (2012) which distinguishes between many crucial damage mechanisms, including matrix cracking, fiber kinking, fiber splitting, and fiber tension. The matrix cracking happens during matrix compression and tension. The criterion includes a built-in search for the critical fracture plane. The fiber compression mode includes stress rotations to the fiber kinking plane and misalignment frame. Failure evaluation is then based on the kink-band formation, traction computations, and fracture plane search (Fig. 52).

The LaRC05 damage criterion was implemented in Abaqus/Standard and can be applied generally to polymer-matrix fiber-reinforced composites for damage evaluation, used for fiber-reinforced composite lamina similar to the Hashin criterion, or combined with crack propagation technologies such as XFEM. Gouskos and Iannucci (2018)

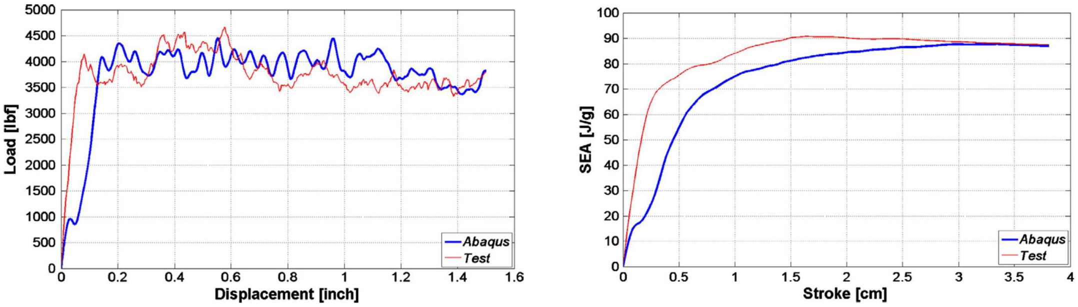

FIG. 51: Comparison between experimental and numerically predicted load-displacement curves (left), and specific energy absorption (right)

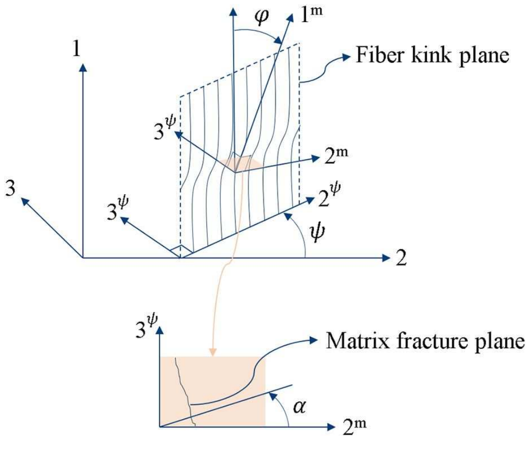

FIG. 52: Mircomechanics damage model for kink-band formation

used the LaRC05 damage criteria in Abaqus with XFEM for crack propagation for a compact tension test of noncrimp fabric laminates. A promising agreement was found in the load-displacement curve and initiation toughness between the experimental results and simulation using Abaqus LaRC05 failure criteria.

4.3 Metals

4.3.1 Lattice Design

New manufacturing techniques such as additive manufacturing allow the creation of new sorts of structures using metamaterials such as lattices. These lattices can be tailored both in terms of their topology and their infill fraction to yield structures with more optimal combinations of weight and mechanical response than could be realized using traditional manufacturing methods. Not only can lattices be used to reduce structural weight, but they can be used in applications such as shock absorption and energy dissipation, vibration damping, and heat exchange due to their large surface area.

Due to their complex structure, in many cases it is not tractable to discretely model the detailed geometry of lattice infill in an engineering structure. In such cases, FE-RVE provides a means to predict an effective response for the lattice, both in terms of linear stiffness and potentially in terms of nonlinear behavior.

The plugin provides a variety of methods to generate certain lattice meshes parametrically, including body-centered lattices, as well as functionality for defining lattice connectivity to create a beam-type lattice model. Through the use of these sorts of tools and the homogenization capabilities of the plugin, one can perform homogenization calculations with lattices of varying infill fractions to determine a polynomial fit of the relationship between infill fraction and effective elastic properties of the lattice. This relationship can then be utilized in topological optimization workflows to design structures with optimal spatially-varying lattice infill fraction (Fig. 53).

Lattice FE-RVE models are able to leverage a broad array of nonlinear physics modeling capabilities in the Abaqus finite element solver. One notable example is using the contact modeling capabilities of Abaqus to predict the crush behavior of lattices. In periodic lattice models, one must account for both self-contact within a single unit cell as well as periodic contact between adjacent unit cells. By copying surface facets from a unit cell to adjacent unit cell locations and using the FE-RVE plugin to periodically constrain the motion of the surface elements to the original unit cell, it is possible to account for this periodic contact while only actually modeling a single unit cell of the lattice (Fig. 54). Such models are capable of accounting for the stiffening effect that self-contact has on lattice response as a lattice is crushed.

In addition to lattices filling space in three dimensions, it is also possible to use FE-RVE simulation to predict the section stiffness properties of shell-type structures with lattice-type geometries (Fig. 55). Structures such as lattice-core panels, corrugated panels, or even structures such as textile composites exhibit in-plane periodicity but lack the in-plane uniformity assumed by laminated plate theory. Through the use of appropriate solid-to-shell type periodic boundary conditions, these structures can be periodically subjected to shell-type deformations which will

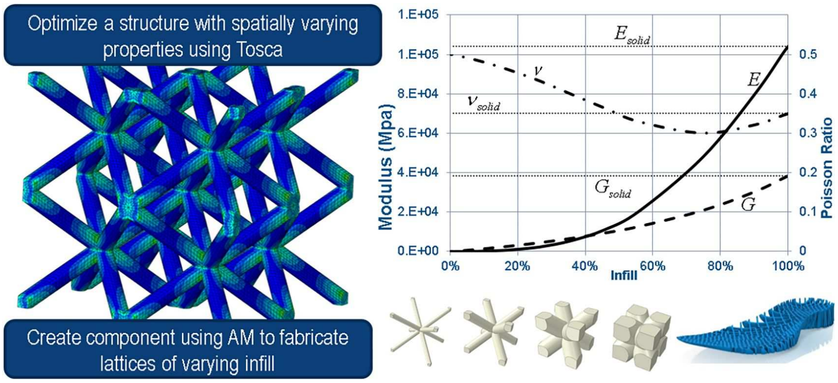

FIG. 53: Relationship between infill fraction and homogenized lattice response from FE-RVE

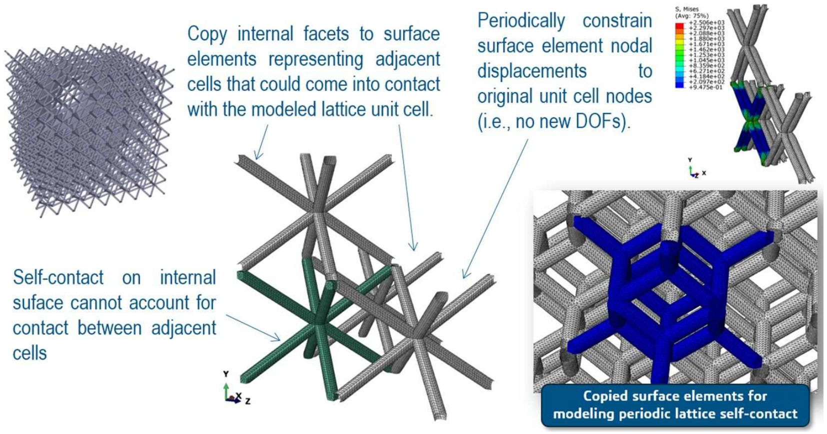

Copy internal facets to surface elements representing adjacent cells that could come into contact with the modeled lattice unit cell.

Periodically constrain surface element nodal displacements to original unit cell nodes (i.e., no new DOFs).

Self-contact on internal suface cannot account for contact between adjacent cells

Copied surface elements for modeling periodic lattice self-contact

FIG. 54: Periodic contact of lattices using surface elements

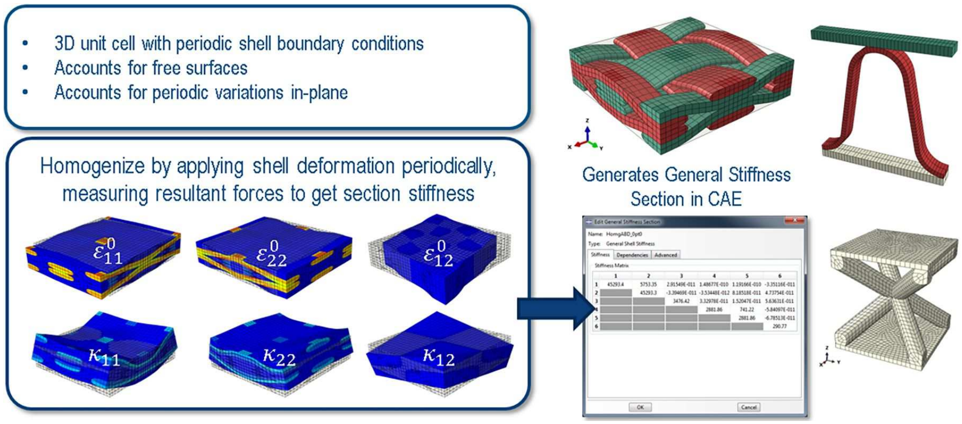

- 3D unit cell with periodic shell boundary conditions
- Accounts for free surfaces
- Accounts for periodic variations in-plane

Homogenize by applying shell deformation periodically, measuring resultant forces to get section stiffness

Generates General Stiffness Section in CAE

Name: HomgABD_0pt0

Type: General Shell Stiffness

Stiffness Matrix

	1	2	3	4	5	6
1	45293.4	5753.35	2.91549E-011	1.48677E-010	1.19166E-010	-3.35116E-011
2		45293.3	-3.39469E-011	-3.53448E-012	8.18518E-011	4.73754E-011
3			3476.42	3.32978E-011	1.52047E-011	5.63631E-011
4				2881.86	741.22	-5.84097E-011
5					2881.86	-6.78513E-011
6						290.77

FIG. 55: Homogenizing shell-section stiffness properties using FE-RVE with solid-to-shell periodic boundary conditions

yield the so-called “ABD” matrix relating shell section forces and moments to the effective membrane strains and shell curvatures so that these structures can be modeled using simple shell elements at larger scales.

4.3.2 Polycrystalline Metals

Advanced high strength steel (AHSS) is widely used in the automotive industry for vehicle lightweighting for their high strength and ductility due to their multiphase microstructures. As a common class of AHSS, dual phase (DP) steels are composed of relatively soft ferrite and relatively hard martensite: the martensite enhances the strength of the material but unfortunately also makes the microstructure inhomogeneous, with a resulting strain partitioning between the two phases (Qin et al., 2018). It is widely agreed that the mechanical properties depend on the stress state, the volume fraction, distribution, morphology, and the strain hardening behaviors of the phases, but research continues to identify which mechanisms dominate as a function of stress state.

FE-RVE modeling provides micromechanics insight as it enables the inspection of local stresses, strains, and potentially damage mechanisms in the material during deformation. Two-dimensional microscopic images (Fig. 56) can be used to reconstruct the microstructure directly in Abaqus using spline curves to ensure smooth phase boundaries (Fig. 57).

Generalized plane strain elements in Abaqus which use reference point/points to control the out-of-plane behavior can be used to model plane stress on average, but allows nonzero out-of-plane stress at each individual node. A calibration exercise is conducted using only single uniaxial tension experimental data to calibrate ferrite properties

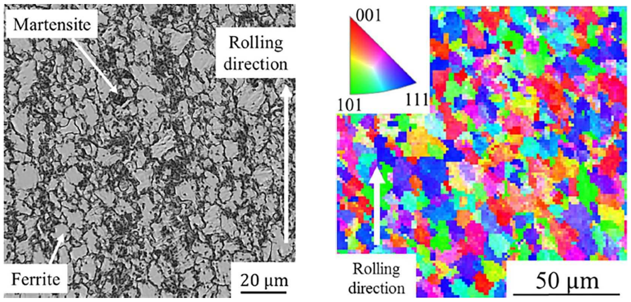

FIG. 56: Left: Optical micrograph in the rolling plane (DP600 – ferrite bright regions martensite dark regions). Right: EBSD map of the rolling plane (no preferred orientation) (reprinted from Qin et al., 2018, with permission from Elsevier, Copyright 2018).

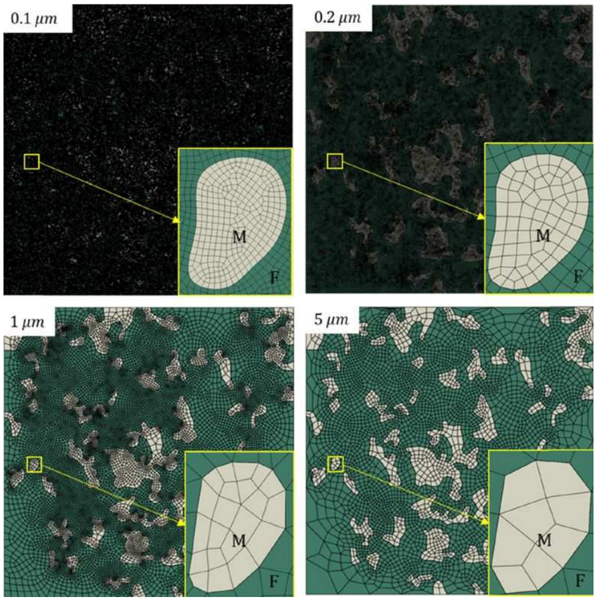

FIG. 57: RVE models with different approximate mesh sizes as noted in the upper corners (reprinted from Qin et al., 2018, with permission from Elsevier, Copyright 2018)

within experimental uncertainty. The RVE is then able to predict multiaxial macroscopic behavior of the multiphase material with reasonable accuracy (Fig. 58).

Use of RVE technology provides additional insights in the overall deformation mechanisms. For example, the highest local strains are developed at closely situated martensite particles; shear bands become clearer with increasing shear loading connecting highly localized deformation in ferrite between closely packed martensite particles, indicating the arrangement of the martensite particles impacts significantly the overall localization behavior (Fig. 59).

Nevertheless, quantitative predictions of evolving microdamage and impact on macroscale behavior remain an art with plenty of research going on. Prediction of ultimate strength and strain remains largely out of scope of RVE technology as typically necking behavior is involved at testing specimen scales. A calibration exercise at macroscale of a Swift (power) law accomplishes the mission (Qin et al., 2018) as shown in Fig. 60.

4.3.3 Grain Microstructure from Phase Field

The Materials Studio Collection (MSC) in Pipeline Pilot has a set of protocols that support modeling of metal alloys. These protocols target prediction of stable phases, properties of random alloys, creation of CALPHAD databases, and phase-field modeling.

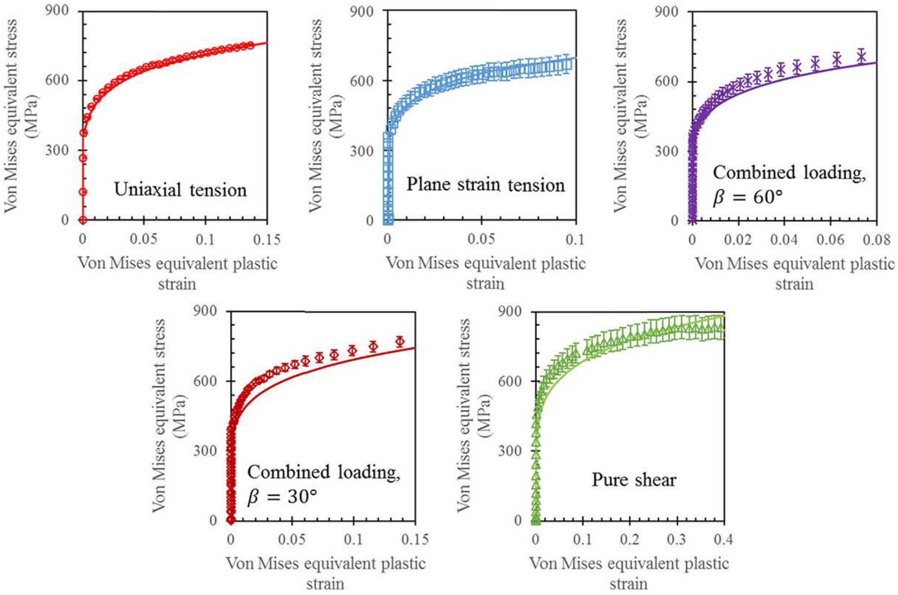

FIG. 58: Mises stress vs. equivalent plastic strain curves—experimental vs. RVE simulations (reprinted from Qin et al., 2018, with permission from Elsevier, Copyright 2018)

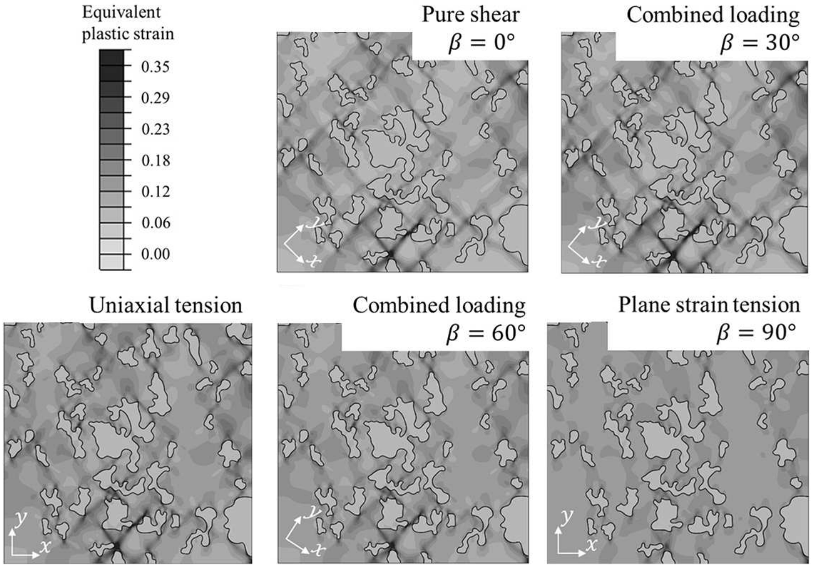
Equivalent plastic strain
0.35
0.29
0.23
0.18
0.12
0.06
0.00
Pure shear $\beta = 0°$
Combined loading $\beta = 30°$
Uniaxial tension
Combined loading $\beta = 60°$
Plane strain tension $\beta = 90°$
y
x

FIG. 59: Equivalent plastic strain fields in the RVE under different loading conditions but the same applied equivalent plastic strain (reprinted from Qin et al., 2018, with permission from Elsevier, Copyright 2018)

Prediction of stable low temperature phases is done by fitting the formation energy to a cluster expansion (CE) using the ATAT toolset (van de Walle et al., 2002a,b). The formation energies for the fitted structures are calculated using the MS CASTEP DFT tool. The cluster expansion is extended until the energy convergence criteria are met and the convex hull predicted by the CE agrees with the one predicted using DFT data. Multiple CEs that use different base lattices can be combined into a single convex hull. In the Al–Ni example in Fig. 61(a), because of their larger size, the known Al_3Ni_2 and Al_3Ni structures are not in the predicted convex hull. Since the number of structures rapidly increases with the number of atoms, it is not possible to include phases with large unit cells. Phases with

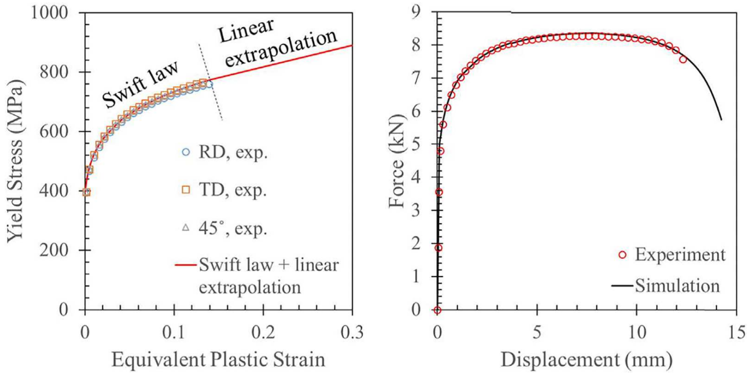

FIG. 60: DP600 strain hardening curves and fitted Swift law hardening extrapolated after necking (left). Force vs. displacement uniaxial tension using a representative macroscale uniaxial tension specimen demonstrating necking behavior (right) (reprinted from Qin et al., 2018, with permission from Elsevier, Copyright 2018).

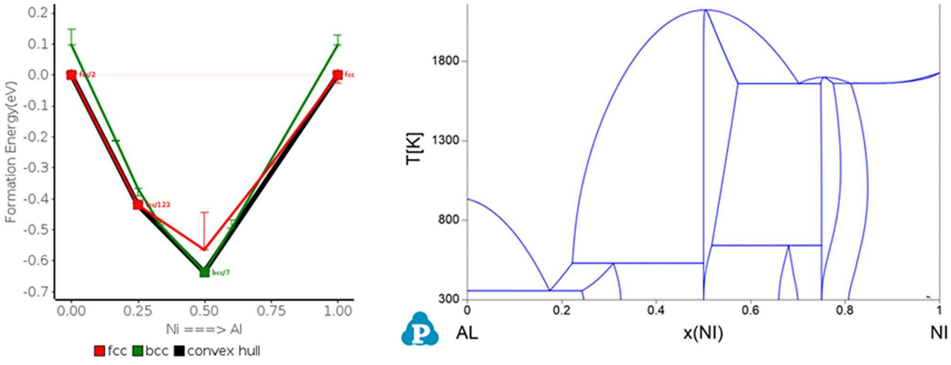

(a) (b)

FIG. 61: Predicted Ni–Al convex hull (left). Phase diagram (right) predicted from a CALPHAD database created using the CE energies.

special lattice structures are also unlikely to show up in the convex hull; only special structures that can be accessed by relaxing a regular lattice structure can be found.

A set of stable structures can be used to create a thermodynamic model in the form of a CALPHAD database. The protocol is built around the ATAT toolset, and in particular the sqs2tdb CALPHAD database fitting tool (van de Walle et al., 2017). A set of special quasirandom structures (SQSs) is created and used as a composition grid for each phase. Formation energy and optionally vibrational free energy for each structure is then evaluated and fitted to a CALPHAD model. There are two options when evaluating the energies: either use the cluster expansions created during the convex hull prediction, or carry out geometry optimization using the CASTEP DFT tool. The use of the cluster expansions as a source of energies supplies almost instant energies but with a lower accuracy compared to the more expensive DFT optimized energies. Figure 61(b) shows the phase diagram generated from the Al–Ni CALPHAD database produced by the protocol. The Ni-rich side of the phase diagram agrees well with existing phase diagrams, while the description of the Al-rich side suffers from the missing Al_3Ni_2 and Al_3Ni phases.

Microstructure prediction for metal alloys can be investigated using a phase-field method. The MSC collection currently supplies two phase-field protocols: one for solidification, and one for grain growth. General parameters such as grid size and temperature are defined through the protocol input parameters. Component- and phase-dependent properties such as interface mobility and composition are specified in a study table. The thermodynamic input for the alloy can be supplied either as a linearized phase diagram or through a CALPHAD database. The protocol can use either ThermoCalc or OpenCALPHAD as a thermodynamic interface to a CALPHAD database. The database can come either from external sources or from a prior calculation with the Materials Studio Collection protocol. The ThermoCalc interface also offers an option of using a mobility database, which supplies diffusion parameters. The simulated microstructure is returned as a trajectory document with field data, while the numerical properties are returned in a study table. The final microstructure can also be returned in Abaqus format for further analysis using SIMULIA tools; see Fig. 62(c).

Figure 62 shows a phase-field modeling example of peritectic solidification of Fe–C. In this example liquid Fe–C with a 0.012 mole fraction of carbon is cooled down, first solidifying into δ-ferrite. As it passes into the peritectic regime, γ-austenite nucleation sites start to nucleate and grow along the liquid-ferrite interface. In Fig. 62 a directional dendrite growth is modeled with an imposed temperature gradient along the growth direction. Initially only δ-ferrite is growing, enriching the melt with carbon. As the temperature at the base of the dendrite drops below the peritectic temperature, γ-austenite begins to nucleate and grow up along the surface of the liquid-ferrite interface consuming both the ferrite and liquid phase. Once the ferrite surface has been covered by austenite, the liquid-ferrite interface is no longer available and the austenite growth in this area becomes diffusion limited. The results from the calculations agree well with both experimental findings (Phelan, 2008) and other simulations (Tiaden, 1999).

4.3.4 Metallurgical Solid Phase Transformation

The input needed for such a sophisticated model is proportionally complex. The user systematically defines all possible transformations that can take place via a parent-children paradigm (e.g., austenite to martensite); the temperature conditions when transformations can occur with associated time-temperature-transformation (TTT) diagrams, Fig. 63(a); and whether the transformations are reversible, diffusional, or nondiffusional. An example of the algorithm leveraged to predict martensitic transformations is shown in Fig. 63(b).

The reliability of additively manufactured (AM) parts is often less than desirable as they suffer from manufacturing defects. Material multiscale techniques as implemented in Abaqus in a generic metallurgical phase transformation framework for metal alloys provide valuable insights and can help the practitioner with assessing the success of a quality print. The multiscale process includes evaluations of phase transformations from raw materials (e.g., powders) via melting/solidification followed by metallurgical solid-state phase transformations associated with either

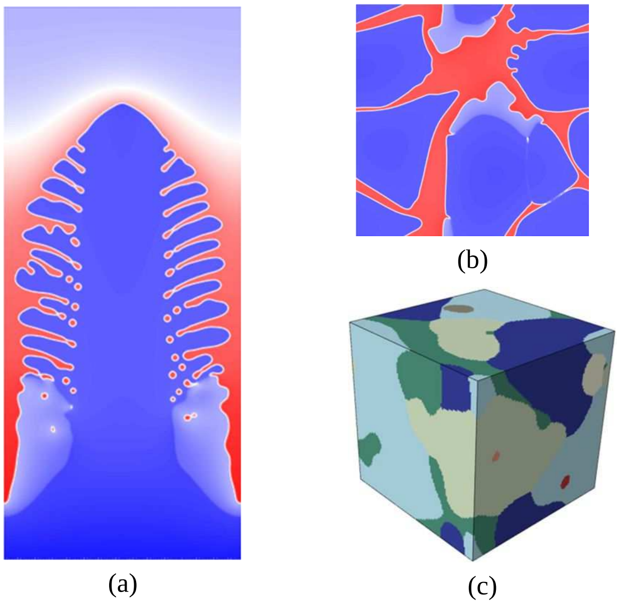

FIG. 62: (a) Ferrite dentrite growing in a thermal gradient, followed by peritectic austenite growth along the liquid-solid interface. The red sections are carbon rich. (b) Peritectic austenite growth along the surface of ferrite grains. (c) 3D micro structure in Abaqus format.

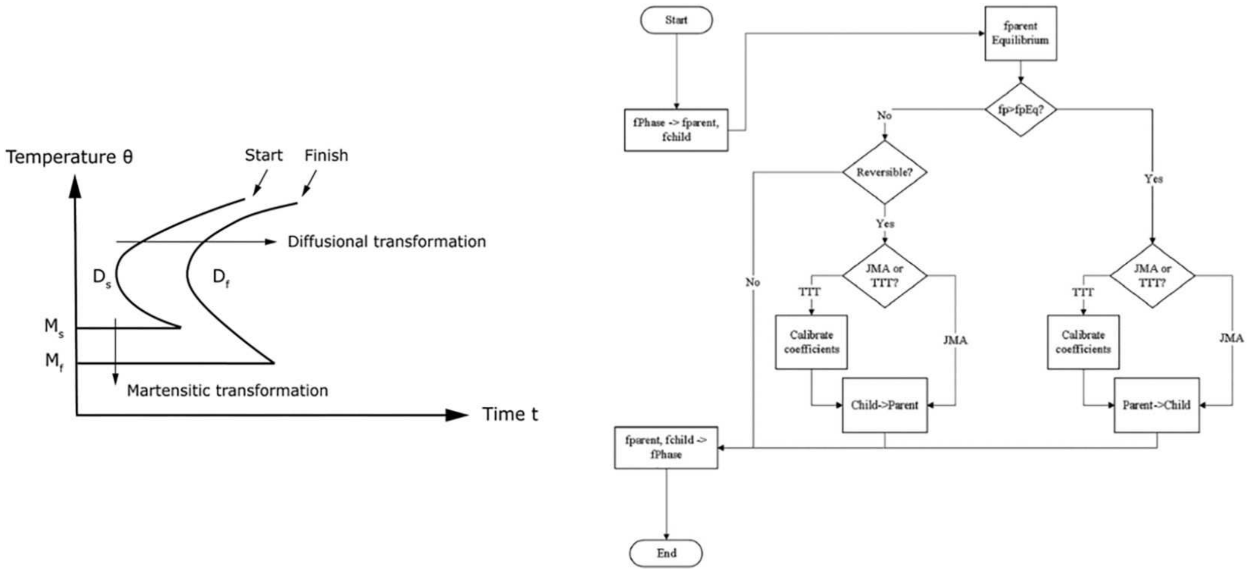
Temperature θ
Start
Finish
Diffusional transformation
D_s
D_f
M_s
M_f
Martensitic transformation
Time t
Start
fPhase -> fparent, fchild
fparent Equilibrium
fp>fpEq?
No
Yes
Reversible?
No
Yes
JMA or TTT?
TTT
JMA
Calibrate coefficients
Child->Parent
JMA or TTT?
TTT
JMA
Calibrate coefficients
Parent->Child
fparent, fchild -> fPhase
End

(a) (b)

FIG. 63: (a) TTT diagram input into the metallurgical phase transformation framework (Abaqus, 2021); (b) algorithm to model martensitic transformations (reprinted from Zhang et al., 2019a, with permission from Elsevier, Copyright 2019)

rapid heating or cooling events in typical 3D printing sequences or slower-rate temperature evolutions associated with heat treatment applications (Zhang et al., 2019a).

Figure 64 provides a quick overview of the multiscale numerical predictions against experimental data starting from melt pool size/shape predictions, unfused powders/pores, volume fractions of solid phases resulting from the highly complex thermal histories, and grain thickness evolution after heat treatment.

Grain morphology is critical to overall prediction of material properties of additively manufactured parts. While Cellular Automata methods have been explored successfully in predicting grain aspect ratios and lamellar thicknesses,

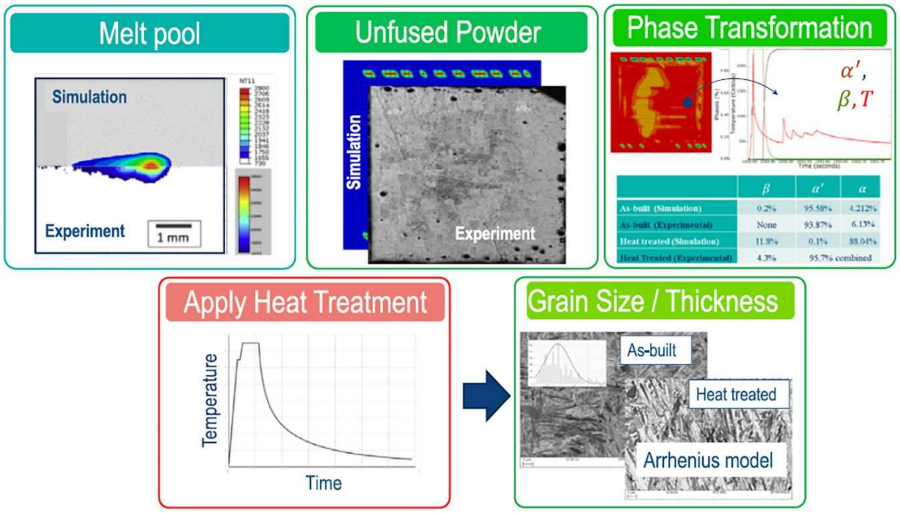
Melt pool
Simulation
Experiment
1 mm
Unfused Powder
Simulation
Experiment
Phase Transformation
α',
β, T
Time (seconds)
Apply Heat Treatment
Temperature
Time
Grain Size / Thickness
As-built
Heat treated
Arrhenius model

	β	α'	α
As-built (Simulation)	0.2%	95.58%	4.212%
As-built (Experimental)	None	93.87%	6.13%
Heat treated (Simulation)	11.8%	0.1%	88.04%
Heat Treated (Experimental)	4.3%	95.7% combined	

FIG. 64: Overview of numerical predictions across multiple scales: from melt pool sizes to volume fraction of the various solidified phases to metal grain sizes for a Ti-6Al-4V alloy (reprinted from Zhang et al., 2019a, with permission from Elsevier, Copyright 2019)

the expense of the methods to cover a large enough area to produce reasonable statistical output in multilayer prints is still reserved for the researchers rather than for the practitioners. Figure 65(a) (Zhang et al., 2019b) shows an EBSD-measure α lamellar thickness which we take as input in the computational model. Figure 65(b) (Abaqus, 2021) compiles from experimental solidification maps grain size and aspect ratio predictions, thermal gradient G and solidification rate R space.

Can one predict material properties for a printed specimen largely based on material multiscale methods? To the authors' knowledge, while reasonable progress has been made worldwide, a pure virtual highly predictive tool chain is not quite achievable. Instead we have relied in this study on micromechanics informed phenomenological models that predict Young modulus, yield stress, and ultimate strength based on volume fractions of solid phases and grain sizes/thicknesses. Combining all these micromechanics pieces of information we have calibrated from those a Ramberg–Osgood plasticity model which predicts yield and strength behavior reasonably well for both as printed and heat treated specimens (Fig. 66).

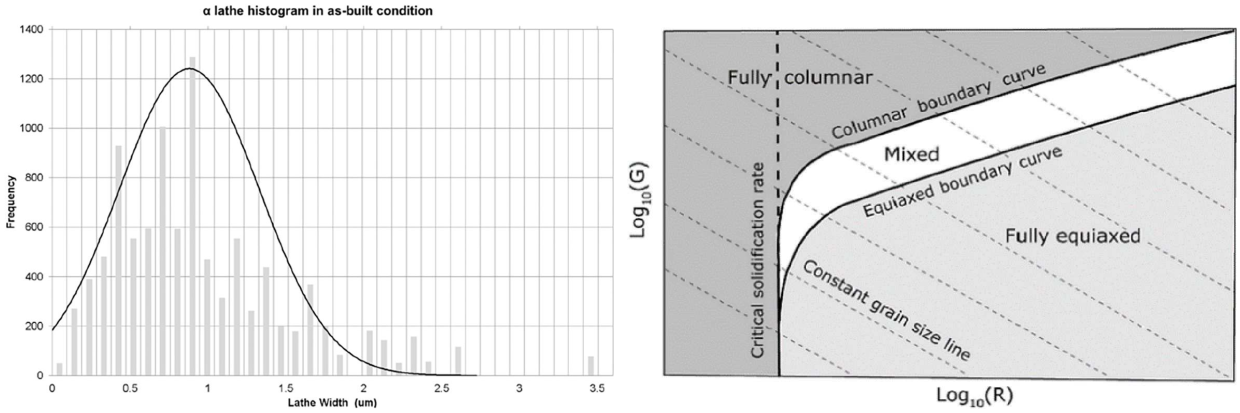

(a) (b)

FIG. 65: (a) Histogram of measured α thickness from image processing of EBSD (reprinted from Zhang et al., 2019b, with permission from Elsevier, Copyright 2019). (b) Solidification map for β grain morphology prediction (Abaqus, 2021).

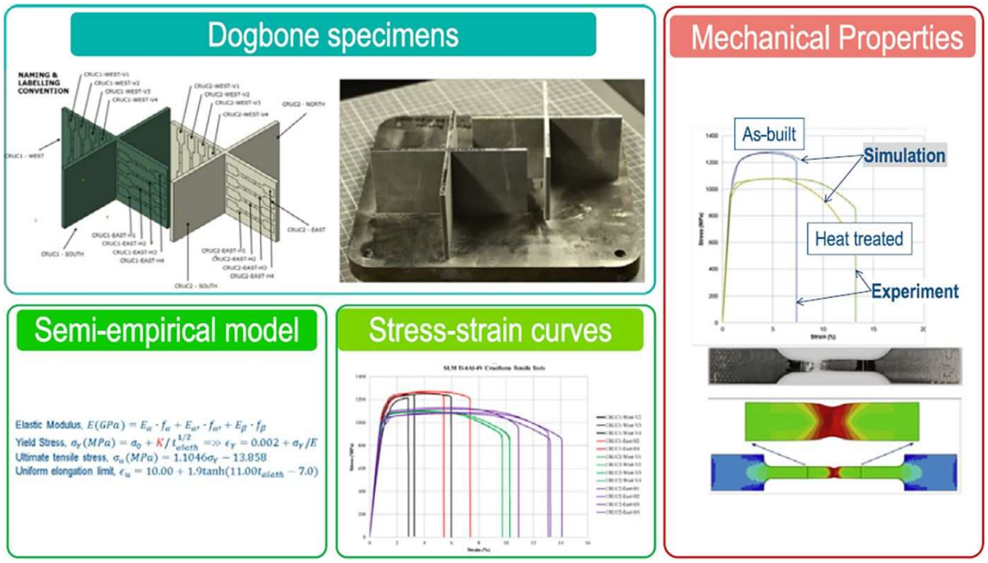

Elastic Modulus, $E(GPa) = E_{\alpha} \cdot f_{\alpha} + E_{\alpha'} \cdot f_{\alpha'} + E_{\beta} \cdot f_{\beta}$

Yield Stress, $\sigma_Y(MPa) = \sigma_0 + K/t_{\alpha lath}^{1/2} \Rightarrow \epsilon_Y = 0.002 + \sigma_Y/E$

Ultimate tensile stress, $\sigma_u(MPa) = 1.1046\sigma_Y - 13.858$

Uniform elongation limit, $\epsilon_u = 10.00 + 1.9\tanh(11.00 t_{\alpha lath} - 7.0)$

FIG. 66: Overview of micromechanics inspired elasto-plasticity/ultimate strength model and comparison between numerical predictions and experimental test data (reprinted from Zhang et al., 2019b, with permission from Elsevier, Copyright 2019)

4.3.5 Metal Surface and Roughness Model for Electromagnetic Simulation

In Section 2.8.2 we described the concept of compact models to efficiently model reflection and transmission from a material setup by means of equivalent surface elements with no thickness. In many applications, the field transmission is actually of less (or no) interest compared to the reflection. This is the case for dense or high conductivity materials where, due to the skin effect, the electromagnetic field penetrates the structure only to a very small extent.

For these scenarios—encountered virtually in any microstrip circuit, filter, or antenna design—we developed the lossy metal and the general surface impedance material models. These release the ideal perfect electric conductor assumption in favor of a more realistic modeling of metal and lead to a more accurate simulation result for S-parameters, circuit insertion losses (Fig. 67) (Tao and Scharf, 2015), quality factor, and radiation patterns.

The material model for metals can either be described analytically (when conductivity is given) or imported from measurement and previous simulations. To smoothen measurement noise and ensure causality and passivity of the final model a vector fitting algorithm is applied as a preprocessing step.

With the increasing application frequency (e.g., high resolution radar, 5G, electro-optical devices) more complex models have to be considered which also take the metal surface roughness into account.

There are some classical approaches to deal with metal roughness, such as the Hammerstad–Jensen (Hammerstad and Jensen, 1980) and the Huray snowball formulation (Huray, 2009), which are also available in our material module.

But even if widely used, the underlying hypotheses for these models are not always met in current applications. This is true especially for the operating frequency and the roughness root mean square, resulting in nonrealistic saturation effects.

To overcome these limitations we adopted a modern formulation, the so-called gradient model (Gold and Helmreich, 2017). This senianalytical model starts from a stochastic representation of the rough surface and still only requires a few input parameters which are generally found in the vendor datasheet.

The obtained surface impedance result is guaranteed to be causal and passive. In comparison to the nonroughness case it shows a change in both the real and imaginary part of the impedance. The former is responsible for the increased losses, the latter for a resonance frequency shift. Both effects have been inspected and confirmed from measurement up to the 100 GHz range (Gold and Helmreich, 2017).

4.4 Rock/Porous Media Characterization

As a major application of porous media (PM) fluid flow simulation, digital rock applications have been developed over the past years based on X-ray microtomography (microCT) imaging technology that allows capturing pore-scale 3D structures of reservoir rocks at the micrometer scale. Flow simulation methods, such as the lattice Boltzmann method (LBM) for single-phase and multiphase flow, have been proved (Jerauld et al., 2017) a valuable addition to conventional laboratory rock characterization, in terms of time, cost, and to improve planning, such as enhanced oil recovery scenario analysis. A multiscale fluid flow workflow LBM extension, as described in Section 2.7, is needed

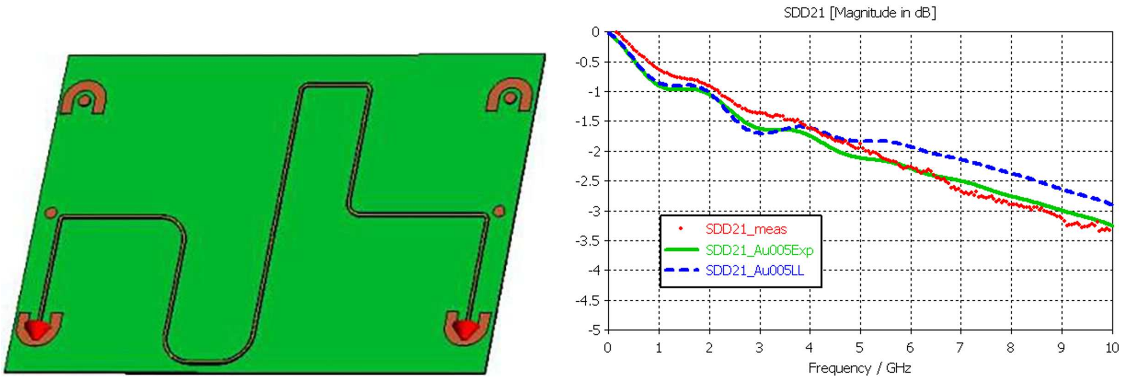

FIG. 67: Printed loadboard design and insertion loss (based on Shlepnev and McMorrow, 2011; based on Moreira et al., 2006)

to enable fluid flow simulation in cases of genuine multiscale pore structure, as found in certain rocks. Here, we show two examples of such cases: a carbonate rock, and a shale rock.

The application of this multiscale workflow to an Indiana limestone carbonate sample is detailed in Fager et al. (2021); here we only present a summary of the main results. First, a small subvolume of the microCT model is selected in order to compare with a registered model. A registered model is a fully resolved dual porosity model, in this case constructed by scaling the microCT model by a factor of 10×, and replacing the PM regions by copies of a 3D PM model, using periodic mirror boundaries that enforce full connectivity of the PM pore structure. We show the images in Fig. 68, bottom from left to right: standard single-scale (no PM regions), registered-synthetic, registered-confocal, and multiscale-PM confocal porosity, where synthetic/confocal correspond to two choices of possible 3D PM models used in the PM regions. The simulated fluid flow property is a water/oil capillary pressure imbibition curve, shown in Fig. 68 (top), where our multiscale results show agreement with the fully resolved registered models, and all of them are quite different from the single-scale result that does not take into account the additional connectivity for fluid flow provided by the ignored PM regions, considered impermeable solid in this case.

Next, a larger volume for this carbonate sample is used for the imbibition simulation. Registered models become impractical at this point, and only results from single-scale and multiscale simulation are shown in Fig. 69, where again we observe that the addition of the PM connectivity enables the injected water to better mobilize the oil in the resolvable pores. These results are in agreement with the experimental measure value of $S_w = 62\%$ at $P_c = 0$. We also show separately the pore/PM contributions to the total saturation and capture in Fig. 69 (insets) four sequential time snapshots in the water/oil displacement, water being injected from the bottom.

A second illustration of our multiscale digital rock workflow is to predict shale matrix permeability (Zhang et al., 2020), that combines first-principles molecular dynamics (MD) and LBM multiscale flow simulations, as illustrated in Fig. 70. Inputs are molecular models for the organic shale content, shale 3D microscopy images, fluid composition, pressure, and temperature. By complementing the flow in the image resolved pore regions with flow in the unresolved pore organic regions, also referred to as PM regions, the overall estimation of the shale matrix permeability can be improved.

The molecular modeling is summarized in Fig. 71. A simulation box containing a number of kerogen molecules is used to construct an organic matter condensed structure, by simulating the NPT ensemble using MD. Density and porosity of the condensed kerogen structure obtained are comparable with published data. Gas adsorption isotherms of methane in these kerogen structures are computed at different pressure and temperature conditions using the grand

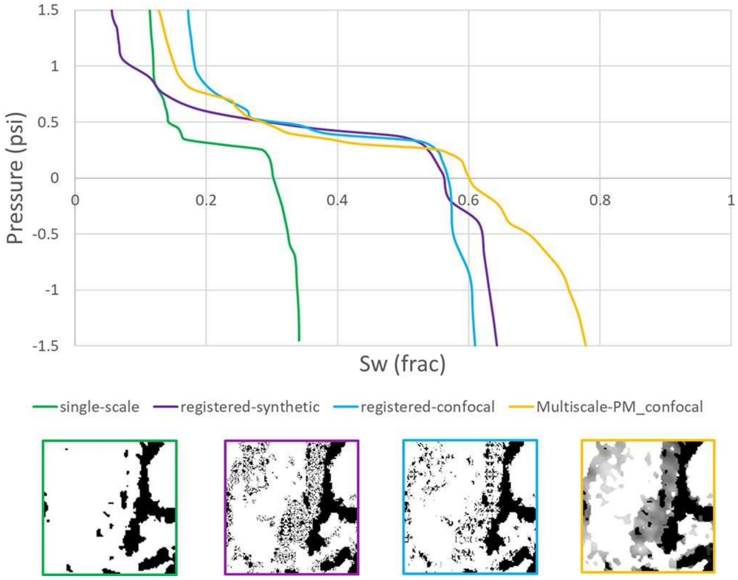

FIG. 68: Carbonate subvolume multiscale simulation and comparison to single-scale and registered models

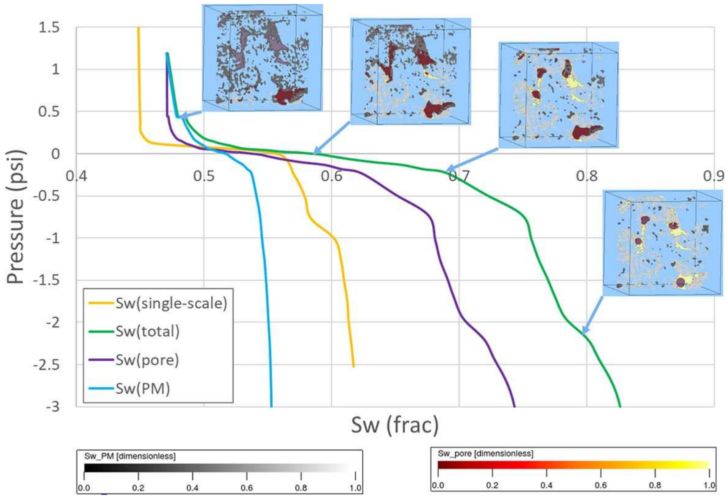

FIG. 69: Carbonate large-volume multiscale simulation, contributions from pore/PM, and four time snapshots

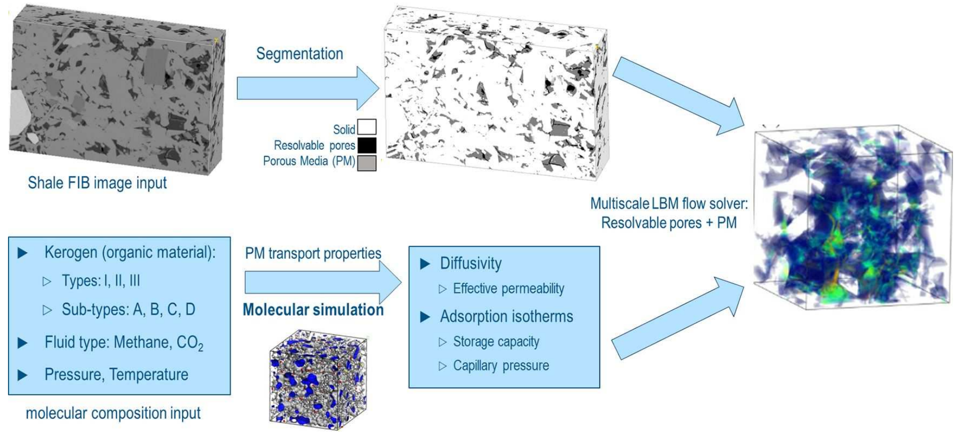
Segmentation
Solid
Resolvable pores
Porous Media (PM)
Shale FIB image input
Multiscale LBM flow solver:
Resolvable pores + PM
▶ Kerogen (organic material):
▷ Types: I, II, III
▷ Sub-types: A, B, C, D
▶ Fluid type: Methane, CO_2
▶ Pressure, Temperature
molecular composition input
PM transport properties
Molecular simulation
▶ Diffusivity
▷ Effective permeability
▶ Adsorption isotherms
▷ Storage capacity
▷ Capillary pressure

FIG. 70: Multiscale workflow combines LBM flow with molecular simulations for unresolved pore permeability in PM regions

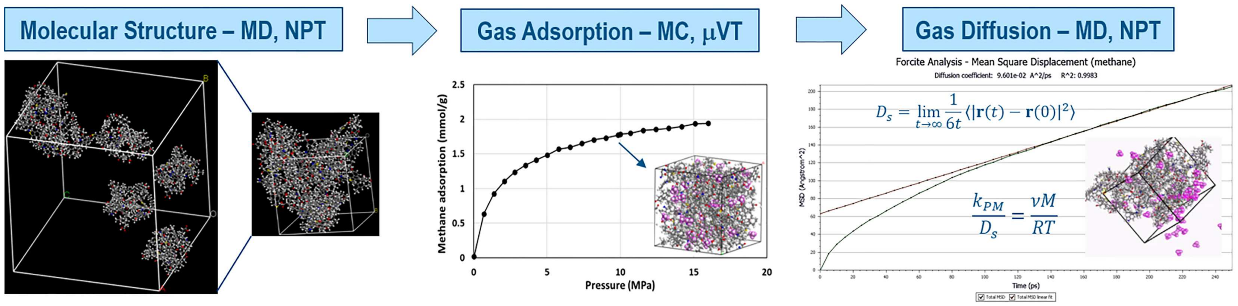

FIG. 71: Molecular simulation of Kerogen structure, methane adsorption, and diffusion coefficient

canonical Monte Carlo (GCMC) method on the μVT ensemble. Based on the configurations obtained from the GCMC simulation, a MD simulation in the NVE ensemble is used to compute the self-diffusion coefficient of methane through kerogen from the resulting trajectories.

Finally, as illustrated in Fig. 72 (left), considering several realizations and model size convergence, an effective kerogen permeability to methane is computed from the self-diffusion coefficient and used as input in a LBM

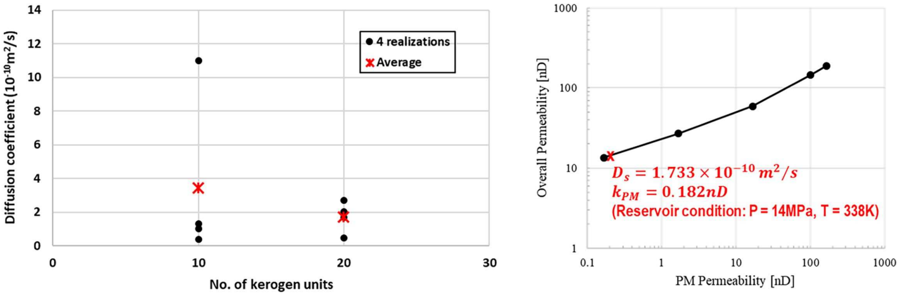

FIG. 72: Diffusion coefficient (left) and overall shale permeability (right) simulation results from multiscale LBM

multiscale flow simulation model to predict overall shale matrix permeability; see Fig. 72 (right). Results for the overall shale sample permeability are more realistic when kerogen permeability is included, which is only possible by using a multiscale workflow.

4.5 Biological Tissue

4.5.1 Micromechanics Informed Biological Soft Tissue Modeling

Biological tissues are anisotropic. Collagen fibers are key ingredients in the structure of arteries. For the artery as an example, in the middle layer, they are arranged in two helically distributed families with a small pitch and very little dispersion in their orientations (i.e., they are aligned quite close to the circumferential direction). By contrast, in the adventitial and intimal layers, the orientation of the collagen fibers is dispersed.

To model anisotropic tissues, phenomenological models and microstructural approaches can be used. Phenomenological models describe macroscopic behavior but provide lower fidelity for practical design applications. The microstructural approach determines the macroscopic mechanical response of the tissue from its underlying components and provides higher fidelity to elucidate structure and function relations. The Lanir and Sacks microstructural constitutive model (Lanir, 1983; Sacks, 2003) is implemented in Abaqus which considers fiber recruitment and fiber orientation in a fiber network embedded in an incompressible matrix.

The total strain-energy potential is decomposed into a network of fibers consisting of fibers with varying waviness and orientation and an incompressible matrix. We start with the actual mechanical strain calculation for a single fiber by undulated initial assumption and straightened by stretch. The single fiber starts to transmit load after it stretches beyond a certain straightened strain. Stress is calculated with linear elastic behavior when stretched. Gradual recruitment of straightened fibers with different waviness is modeled with a recruitment density distribution function D which attributes to a nonlinear stress strain behavior. The recruitment density distribution function describes the varying degrees of undulation of individual fibers and the ensemble strain-energy potential is described as the sum of individual strain energies weighted by the distribution of slack strains. Last, the ensemble response is homogenized to the tissue level by defining the network fiber strain energy as the sum of strain energy of fiber ensembles, weighted by an orientation distribution function R (Fig. 73).

This multiscale material model is implemented in Abaqus via invariant-based strain-energy potential user subroutines (UANISOHYPER_STRAIN) (Kaul et al., 2014). The model can be used together with Mullins effect to include stress softening (damage) behavior, and viscoelasticity to include rate effects. We define the strain-energy potential of an anisotropic hyperelastic material as a function of Green strain and volume ratio. The component of strain is defined by *ORIENTATION, where the fiber mean orientation information comes in. Given the following inputs to the multiscale material model—matrix as an incompressible neo-Hookean material, linear modulus of fiber, and parameters to describe fiber-recruitment distribution and fiber-orientation distribution—we are now able to investigate the macroscopic effects from microstructural properties. We simulated the suture stretch test and compared fiber orientation prediction to measurements from small-angle light scattering (SALS) (Billiar and Sacks, 1997). Good agreement was achieved about the reorientation of the preferred fiber direction towards the direction of stretch, and the amount

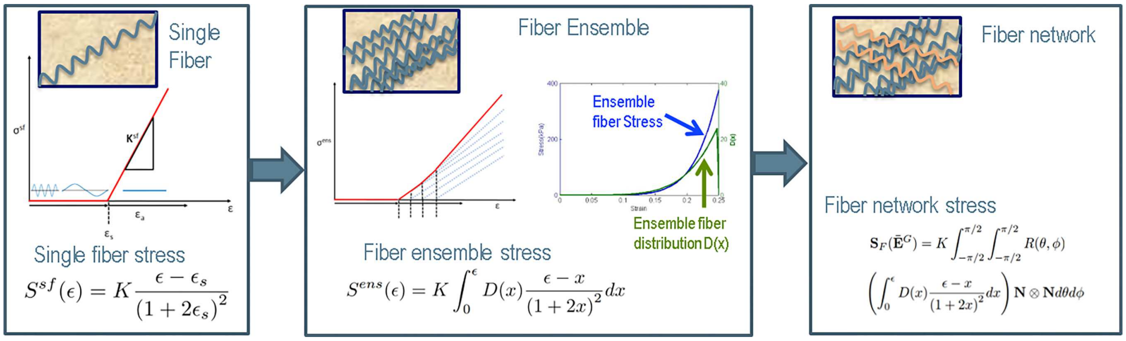
Single Fiber
σ^{sf}
K^{sf}
ϵ_a
ϵ_s
ϵ
Single fiber stress
$S^{sf}(\epsilon) = K\frac{\epsilon-\epsilon_s}{(1+2\epsilon_s)^2}$
Fiber Ensemble
σ^{ens}
Ensemble fiber Stress
Stress(kPa)
D(x)
Strain
Ensemble fiber distribution D(x)
Fiber ensemble stress
$S^{ens}(\epsilon) = K\int_0^{\epsilon} D(x)\frac{\epsilon-x}{(1+2x)^2}dx$
Fiber network
Fiber network stress
$\mathbf{S}_F(\bar{\mathbf{E}}^G) = K\int_{-\pi/2}^{\pi/2}\int_{-\pi/2}^{\pi/2} R(\theta,\phi)$
$\left(\int_0^{\epsilon} D(x)\frac{\epsilon-x}{(1+2x)^2}dx\right)\mathbf{N}\otimes\mathbf{N}d\theta d\phi$

FIG. 73: Implementation of Lanir and Sacks microstructural model that considers fiber recruitment and fiber orientation in a fiber network embedded in an incompressible matrix in Abaqus

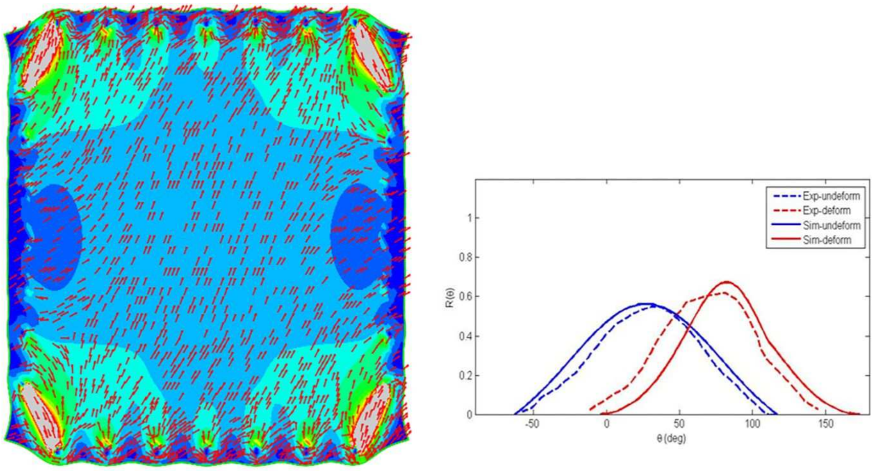

Preferred fiber orientation overlaid with tissue stress

Fiber orientation distribution

FIG. 74: Simulation result of suture stretch test using the microstructural model in good agreement with experimental measurements

of increase in the degree of fiber alignment (Fig. 74). The experimentally determined mean preferred fiber direction increased about 48°; the simulation predicted increase about 54° with 12% differences (Waldman et al., 2002).

4.5.2 Skin Penetration Model at Molecular and Biological Tissue Scales

Skin barrier properties are essential in various fields of research, in toxicology and risk assessment for preventing the uptake of harmful substances, in medical drug administration via transdermal delivery, and in the design of cosmetic products (Schwöbel and Klamt, 2019). *In vivo* and *in vitro* measurements are difficult to conduct; on the one hand they are expensive and time consuming, and on the other hand there are ethical and regulatory reasons. A new area of interest is the dermal penetration through variable skin systems, which can be obtained by the COSMOplex method in an efficient way (Klamt et al., 2019), not limited to the normal skin, but including hydrated skin systems, systems enriched by penetration enhancers, or even compromised skin systems (Schwöbel and Klamt, 2019).

The mechanistic skin penetration model is constructed as a set of parallel and serial resistors, bridging the microscopic scale, with its three-dimensional interactions on a molecular level, and the biological pathways on a cellular level at micrometer scale, as shown in Fig. 75. The cellular scale reflects cell shapes, cell and tissue sizes, and tortuosities from layered structures of cells and corneocytes. Molecular interactions between the penetrant and matrices present in the different parts of the skin (lipids, phospholipids, proteins, plasma, stroma, etc.) are calculated by the statistical thermodynamics method conductor-like screening model for realistic solvation (COSMO-RS) (Klamt et

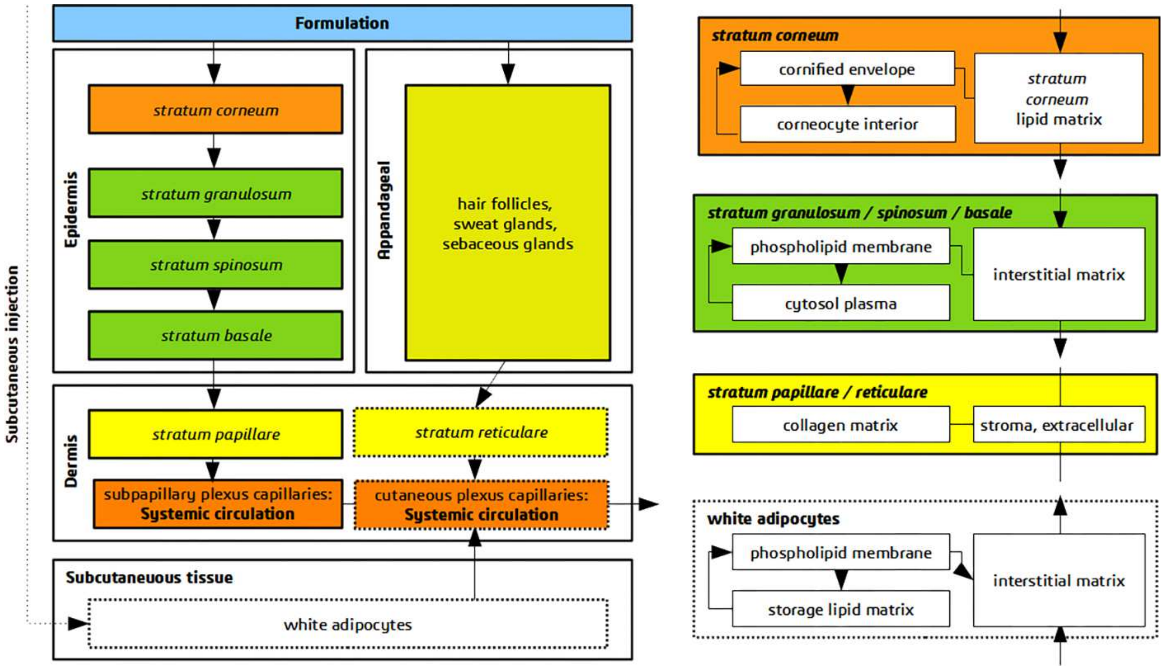
Formulation
Subcutaneous injection
Epidermis
stratum corneum
stratum granulosum
stratum spinosum
stratum basale
Appandageal
hair follicles,
sweat glands,
sebaceous glands
Dermis
stratum papillare
stratum reticulare
subpapillary plexus capillaries:
Systemic circulation
cutaneous plexus capillaries:
Systemic circulation
Subcutaneuous tissue
white adipocytes
stratum corneum
cornified envelope
corneocyte interior
stratum corneum lipid matrix
stratum granulosum / spinosum / basale
phospholipid membrane
cytosol plasma
interstitial matrix
stratum papillare / reticulare
collagen matrix
stroma, extracellular
white adipocytes
phospholipid membrane
storage lipid matrix
interstitial matrix

FIG. 75: Biophysical tissue model of the pathways involved in the skin penetration process (left) and biochemical matrices involved (right), with particular partitioning and diffusion related parameters predicted at the molecular scale by COSMO-RS therein

al., 1998). The particular matrices are shown on the right-hand side of Fig. 75, e.g., *stratum corneum* lipid structure, cornified envelope, and phospholipid membranes of cells in the viable epidermis, plus mostly aqueous media in corneocytes, cell plasma, and the interstitial space. More in detail, permeabilities related to matrix:water partition coefficients and matrix-specific diffusion coefficients are calculated systematically by the efficient COSMOperm method (Schwöbel et al., 2020), capable of accounting for local microstructures, with calculational times of a few minutes despite its subatomistic nature at a quantum chemical level. The extended model in Fig. 75 contains the dermis and subcutaneous compartment in addition to the original model. Here, absorption by the collagen fiber matrix is predicted by partition coefficients to structural proteins by protonation state-specific COSMO σ moments (Bittermann et al., 2018), corrected by the slightly lower affinities of typical organic molecules to collagen as compared to structural proteins in muscles (Endo et al., 2012). Geisler et al. (2015) showed that COSMO-RS is the most predictive method to obtain the partitioning into storage lipids, especially for complex compounds. Storage lipids are present abundantly in white adipocytes of the subcutis, and are relevant to describe the controlled release of drugs injected subcutaneously.

Formulation related vehicle effects are directly accounted for via COSMO-RS ($r^2 = 0.94$), i.e., the influence of the topically applied formulation containing the active ingredient, which can alter the skin penetration rate by several orders of magnitude. Diffusion coefficients ($r^2 = 0.82$) and free energies related to partitioning ($r^2 = 0.94$) are validated against molecular dynamics simulations (Lundborg et al., 2018), and the resulting skin penetration rate against experimental $\log_{10}(K_p)$ values, with an accuracy of *rmse* $= 0.33$ for the *stratum corneum* membrane alone, or *rmse* $= 0.72$ for the human *ex vivo*/*in vitro* epidermis membrane. Even more, the model is able to capture the effects of various skin types, e.g., different levels of hydration or the effect of skin penetration enhancers.

4.5.3 Modeling of Ionic Channels in a Heart

Drugs can induce lethal arrhythmias in the heart, such as torsade de pointes. The risk evaluation of a new compound is costly and can take a long time, which hinders the development of new drugs. Multiscale ionic channel modeling can help quickly access the cardiac toxicity of new and existing drugs. The input of the model is the drug-specific current block from single-cell electrophysiology and the output is the spatiotemporal activation profile and associated electrocardiogram. The mechanism of electrophysiological abnormalities propagation from specific channel blockage, via altered single-cell actin potentials and prolonged QT intervals, to the spontaneous emergence of ventricular tachycardia in the form of torsades de pointes can be revealed and studied.

First, the electrophysiology of the cardiac tissue is represented by the spatiotemporal evolution of the transmembrane potential ϕ following the reaction-diffusion governing equation:

$$\dot{\phi} = \mathrm{div}(\boldsymbol{D} \cdot \nabla\emptyset) + f^{\emptyset}. \tag{12}$$

For the flux term, $\mathrm{div}(\boldsymbol{D} \cdot \nabla\phi)$, we assume an anisotropic conductivity $\boldsymbol{D}$ with a fast contribution parallel to the myocardial fiber direction and a slow contribution perpendicular to it. For the source term, f^{ϕ}, we use different ionic models for different cell types and introduce the source as the ionic current scaled by the membrane capacitance. To solve the governing equation [Eq. (12)] we exploit the structural similarities of the electrophysiological problem with a heat transfer problem with a nonlinear heat source in Abaqus Unified FEA (Abaqus, 2021).

The ionic currents are functions of the membrane potential and a set of state variables $q(\theta)$. The state variables obey ordinary differential equations as functions of the transmembrane potential ϕ and their current values q.

Bi-ventricular model of a healthy 21-year-old, 50th percentile U.S. male human heart is used for this study (Fig. 76). The O’Hara–Rudy model is adopted for the ventricle cells, and the Stewart model is adopted for the Purkinje fiber network. The O’Hara–Rudy model is based on 15 ionic currents, for example, the L-type calcium current I_{CaL}, the fast and late sodium currents I_{Na}, the calcium sodium and calcium potassium currents I_{CaNa} and I_{CaK}, etc., and 39 state variables. The fast sodium current I_{Na} is replaced with the ten Tusscher model to model the propagation in tissue scale simulations. The model is parameterized to account for regional specificity for three different ventricle cell types: epicardium, midwall, and endocardium cells. The Stewart model enables self-excitation without external stimulus based on 14 ionic currents and 20 state variables. Figure 77 shows the single-cell action potential for ventricular cardiomyocytes on the left and Purkinje fiber cells on the right. The ventricle cell model distinguishes between endocardial, midwall, and epicardial cells (Fig. 77).

The finite element model solves the governing equations by discretizing the transmembrane potential as nodal degrees of freedom, and the ionic currents and gating variables as internal variables. Tissue anisotropy is included in the flux term by fiber definitions and choice of isotropic and anisotropic conductivities. For the source term, a body flux subroutine incorporates the ionic currents in the solid element formulation. To account for regional specificity in cell type, a series of Laplace problems are simulated using the ventricular model with three sets of essential boundary conditions at the epicardial and endocardial surfaces. The Purkinje fiber network is created to densely cover the endocardium using the user element for modeling the discretized governing equations. The effects of the drugs on

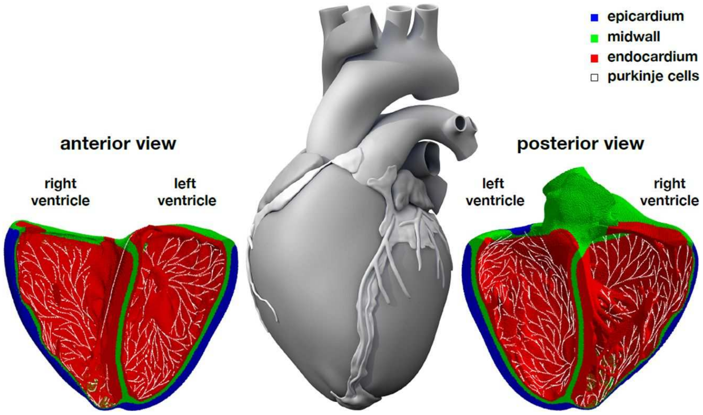

FIG. 76: Finite element model of left and right ventricles with very refined mesh, three layers, and the Purkinje fiber network used for multiscale modeling (reprinted from Sahli Costabal et al., 2018, with permission from John Wiley & Sons, Copyright 2018)

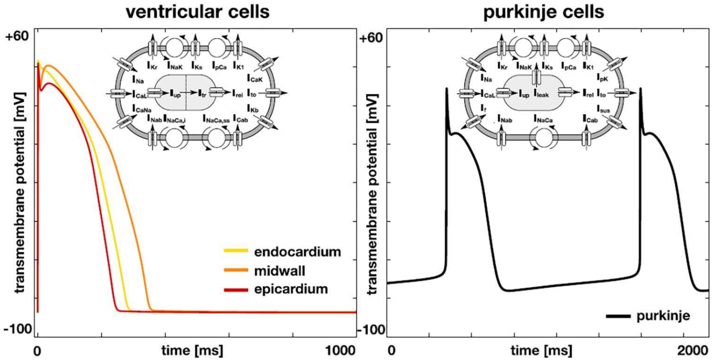

FIG. 77: Single-cell action potential for human ventricular cardiomyocytes and Purkinje fiber cells implemented in Abaqus (reprinted from Sahli Costabal et al., 2018, with permission from John Wiley & Sons, Copyright 2018)

single-cell potentials are modeled by selectively blocking the ionic currents. The degree of block of individual ion channels is measured experimentally and fitted to Hill-type equations to estimate fractional block.

Figure 78 shows the excitation profiles and electrocardiogram recordings for baseline and drug treatment with ranolazine and quinidine from the multiscale simulations. Black arrows in the electrocardiograms indicate the time points of the ten excitation profiles of each sequence. Compared to baseline with a return to the resting state within 460 ms, drug treatment with ranolazine delays the repolarization period and the return to the resting state takes 505 ms. In both cases, excitation is driven by the Purkinje network, with repeated, similar depolarization patterns every 1000 ms. Drug treatment with quinidine triggers a sequence of rapid, widened irregular QRS complexes with varying activation fronts from right to left, from base to apex, from left to right, and from apex to base, before the heart returns to its resting state at 4750 ms (Fig. 78).

5. MULTISCALE MATERIALS—OTHER APPLICATION AREAS

It is often the case that engineered components or complex products are made of many materials interacting in the complex multiphysics/multiscale sense. In this section we review a handful of such applications, as in the previous section, without being able to reference our industrial partners.

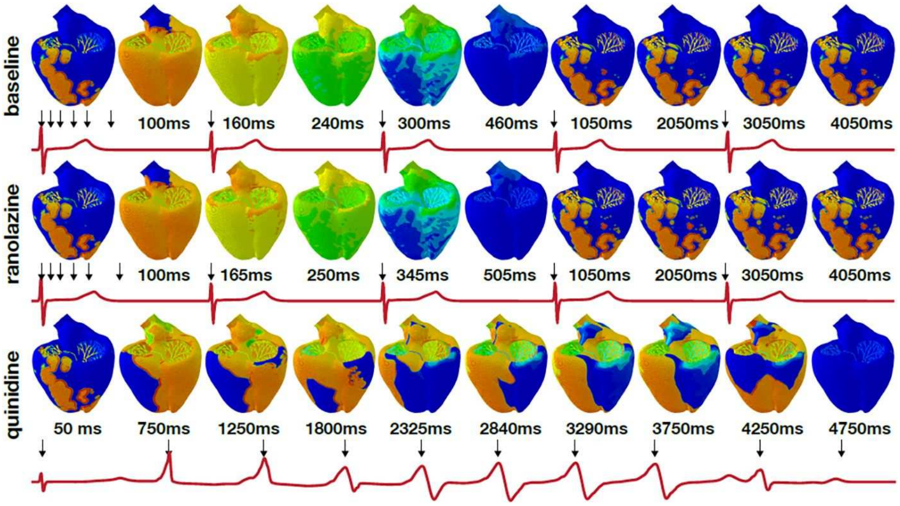
baseline
100ms
160ms
240ms
300ms
460ms
1050ms
2050ms
3050ms
4050ms
ranolazine
100ms
165ms
250ms
345ms
505ms
1050ms
2050ms
3050ms
4050ms
quinidine
50 ms
750ms
1250ms
1800ms
2325ms
2840ms
3290ms
3750ms
4250ms
4750ms

FIG. 78: Excitation profiles and electrocardiogram recordings for baseline and drug treatment with ranolazine and quinidine (reprinted from Sahli Costabal et al., 2018, with permission from John Wiley & Sons, Copyright 2018)

5.1 Tire Reinforcements

Tires are highly complex, mission critical composite structures that routinely operate in extreme environmental and loading conditions. They must be engineered to satisfy a long list of challenging, and often competing, design criteria. Criteria include good wear and handling characteristics over a range of surface types and weather conditions, survivability during extreme events, e.g., hitting a pothole, low rolling resistance for improved gas mileage, quiet operation, and economically feasible manufacturing costs.

In the tire industry, the phrase “magic triangle” refers to the competing goals of minimizing rolling resistance while at the same time maximizing traction and wear (Flanigan et al., 2011).

To remain competitive, tire manufacturers continually modify and improve their designs. They must meet the constantly shifting requirements from the automobile, truck, and aircraft industries and from safety and environmental regulations that exist in a wide range of global economic regions. Tire engineers rely heavily on numerical simulations to meet these design challenges.

SIMULIA is the recognized world leader in tire simulation technology. We offer a wide range of advanced material and friction models and specialized procedures for quickly generating complex tire models, including ply reinforcement and tread designs. We support a wide range of modeling procedures for the manufacturing process, footprint simulations, steady-state operating conditions (both implicit and explicit time integration), standing waves, hysteretic heat generation, extreme impact events, hydroplaning, and acoustics.

Most pneumatic tires are reinforced with embedded plies, belts, and beads, as illustrated in Fig. 79 (see https://www.firestonecompleteautocare.com/blog/tires/what-are-different-parts-of-a-tire/).

Abaqus offers a complete set of rebar modeling features that allow you to economically capture the small-scale structural response of embedded reinforcements in a large-scale model. These features include rebar layers in shell, membrane, and surface elements. Solid elements are reinforced using embedded element constraints. Rebar layers have material properties that are independent of the host elements and they can accurately capture shearing effects that occur in large deformations. To simplify the modeling process the ply geometry can be conveniently specified with respect to the “green,” or uncured, tire configuration. The tire lift equation provides mapping from the uncured geometry to the cured geometry (see Fig. 80).

To improve tire wear characteristics, it is common practice to added silica to the rubber (Flanigan et al., 2011). Embedded silica particles typically have a much higher modulus than the rubber matrix and thus increase the homogenized stiffness of the tire.

Figure 81 outlines a workflow in which a periodic unit cell of a rubber matrix filled with particles, modeling silica, is used to generate a virtual global response of a filled material using the SIMULIA FE-RVE technology discussed in Section 2.9. A Yeoh hyperelastic material with linear viscoelasticity is calibrated to the FE-RVE response data using the Material Calibration app discussed in Section 3.2. A footprint and rolling analysis of a typical automobile tire is subsequently performed using both the filled and unfilled materials. As expected, the stiffer response of the filled material leads to a smaller tire deformation and modified footprint pressure.

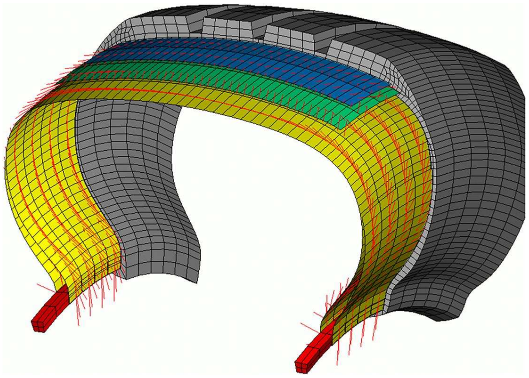

FIG. 79: Typical tire cross section

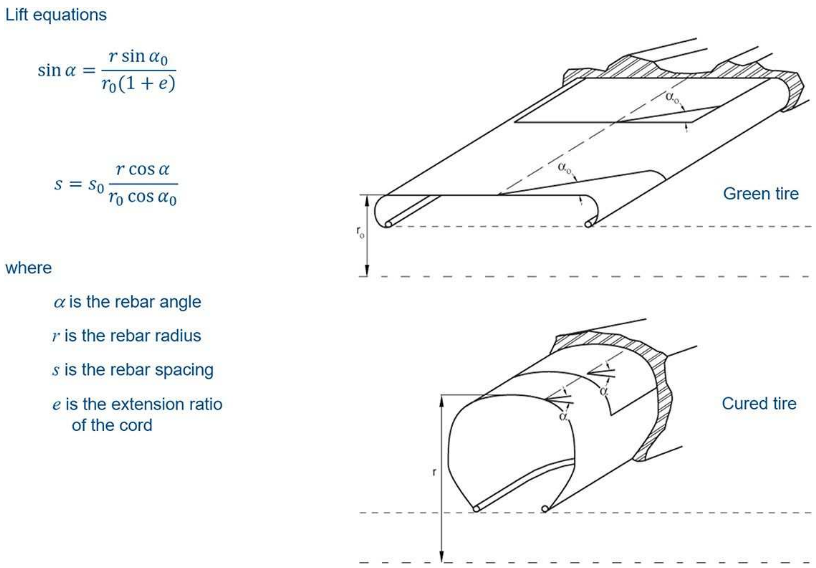

Lift equations

$$\sin\alpha = \frac{r\sin\alpha_0}{r_0(1+e)}$$

$$s = s_0\frac{r\cos\alpha}{r_0\cos\alpha_0}$$

where

α is the rebar angle

r is the rebar radius

s is the rebar spacing

e is the extension ratio of the cord

Green tire
Cured tire
α_0
α_0
r_0
α
α
r

FIG. 80: Lift equations for mapping from uncured to cured tire geometry

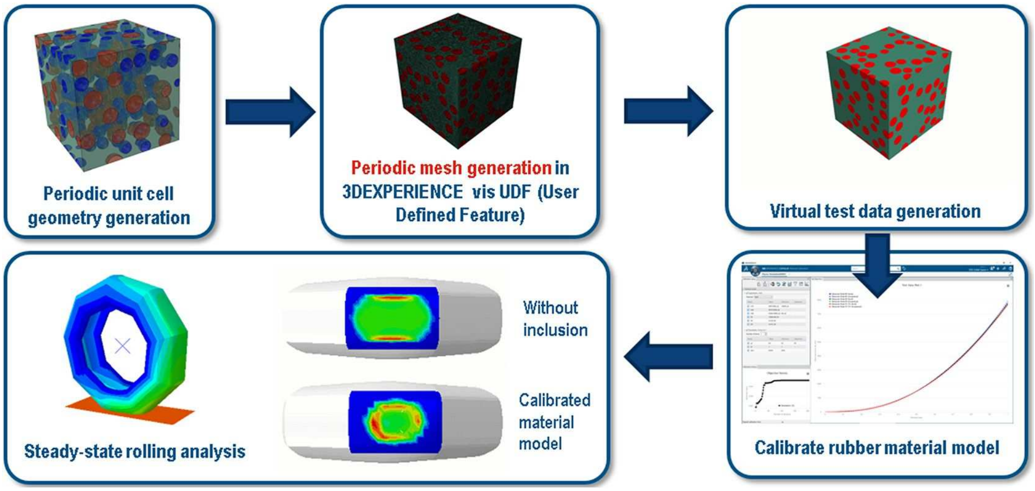

Periodic unit cell geometry generation
Periodic mesh generation in 3DEXPERIENCE vis UDF (User Defined Feature)
Virtual test data generation
Calibrate rubber material model
Steady-state rolling analysis
Without inclusion
Calibrated material model

FIG. 81: Sample multiscale calibration workflow for a filled rubber and subsequent tire simulation

5.2 Helicopter Rotor Blades via Multiscale Materials

Multibody simulation (MBS) software systems are used across all industries for the design of wind turbines, aircrafts, automotive and rail vehicles, in the field of general machinery, and for further purposes. Multibody simulation deals with the dynamic behavior of complex mechanical systems or the interactions of the components of these systems. On the other hand, the finite element method (FEM) is the standard to determine deformations, mechanical stress, etc., of individual components of such systems. Increasingly, product development requires a concurrent use of these simulation domains, since the deformation of individual components and the behavior of the entire mechanical system might significantly influence each other.

This is especially true for helicopter rotor blades, which, integrated into the mechanical system model of a helicopter, are subjected to tremendous Coriolis forces, centrifugal stiffening, and aerodynamic forces, and finally the coupling of flap, lag, and torsional deformation making it necessary to consider structural elasticities with high accuracy at a low computational cost.

In contrast to high-resolution finite element methods, it is a strength of multibody system models to describe complex mechanical systems with a comparatively small number of degrees of freedom, which leads to a low computational effort and suits it to the validation of various designs. The increasing knowledge during the design process can be accounted for easily by an increasing level of detail of the MBS and FEM models.

For a wide range of application areas in which the assumption of small deformation and linearized material laws is sufficient, most MBS solvers use the floating frame of reference formulation for modeling linearized structural flexibilities, in which a modal deformation field is superimposed on finite rigid body motion. The modal deformation field, inertia invariants, modal stiffness, and damping are generated in the FEM software and passed on to the multibody system model. The setup of such flexible body representation is almost automated.

A nonlinear reduced order modeling technique has been developed for use in multibody systems when components of a mechanical system exhibit large deformation effects. So far, this technique is available for wind turbine rotor blades and torsion beam suspensions of automotive vehicles. However, such nonlinear reduced order models cannot be used yet for rotor blades of helicopters due to an insufficiently accurate description of the inertia forces.

The obvious abstraction level for a rotor blade is that of a beam structure. Composite beam theory offers an alternative for modeling flexible helicopter rotor blades. This features in-plane and out-of-plane deformations of the cross sections and finite deformations of the axes of the beam elements (Han and Bauchau, 2015). The constitutive equations of such a beam structure can be computed from a linear finite element model that represents the flexibility of the different materials of a cross section such as woven-, long fiber-, core, and other materials, which enables an automated transition to the logical scale. The according cross-sectional analyses yield the material matrix for all directions of bending, torsion, and axial deformations and recovery relations allowing the computation of the three-dimensional cross-section deformation from the deformation of the beam axis and stress and strain from the stress resultants after completion of the multibody system analysis.

Based on a 3D model built with the CATIA apps on the **3D**EXPERIENCE Platform a blade of the main rotor with material assignments was converted into a beam representation by a script, which has been implemented as a proof of concept. To run this script the user specifies the beam discretization of the blade model, parameters for setting up the mesh for the cross-sectional analyses such as element type and size, and output requests such as the field variables for which data shall be recovered in the post-processing of the multibody simulation. The rotor blade generation script first generates cross-section geometry in the middle of each beam element, meshes each cross section, triggers the cross-sectional finite element analyses, and passes finally their results, the material law, cross-sectional inertia data, and recovery relations on to the multibody system model along with a complete nonlinear beam representation. The entire abstraction process from the 3D model towards a 1D structural beam model was fully automated (Fig. 82). The beam representation has been validated against 3D finite element models. Even accurate local stress and strain data can be extracted for almost prismatic structures.

A multibody system model of the BO 105 multipurpose light helicopter was set up to demonstrate the workflow for the validation of design variants of an entire mechanical system through simulation (Fig. 83). The mechanical model of the helicopter was first set up in the CATIA apps of the **3D**EXPERIENCE Platform and then converted into a multibody system model. The flap and lead-lag hinges of the four composite rotor blades are represented by the elastic bending properties of the blade roots. Their correct modeling in the multibody system model is prerequisite to replicating the behavior of the helicopter with sufficient accuracy. Finally, the multibody system model was coupled with the comprehensive versatile aeromechanics simulation tool (VAST) of the German Aerospace Center (DLR) by cosimulation. A total of 20 collocation points were distributed over the radius of the main rotor to exchange deformation, lift and drag forces, and the aerodynamic torque. Pilot inputs are propagated to the pitch angles of the main rotor blades through a detailed model of the mixing lever assembly and the swashplate. Similarly, rigid representations of the tail rotor blades have been coupled with VAST.

Trim calculations for various forward flight velocities showed an acceptable match between simulation and flight test data for the collective and longitudinal main rotor blade control angle, whereas the lateral control angle for higher flight velocities did not match the test data. A reason for deviations in the required lateral control angle at high flight velocities is the influence of the fuselage on flow velocities at the rotor, which is not yet included in VAST. Further flight maneuver simulations are described in Mindt et al. (2019).

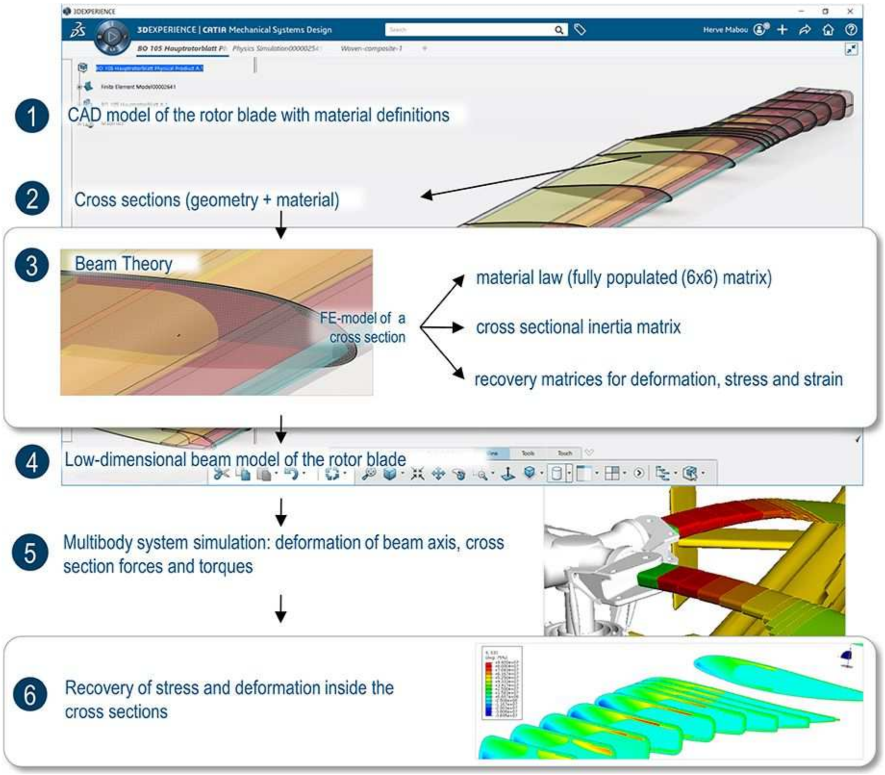
3DEXPERIENCE | CATIA Mechanical Systems Design
BO 105 Hauptrotorblatt
1 CAD model of the rotor blade with material definitions
2 Cross sections (geometry + material)
3 Beam Theory
FE-model of a cross section
material law (fully populated (6x6) matrix)
cross sectional inertia matrix
recovery matrices for deformation, stress and strain
4 Low-dimensional beam model of the rotor blade
5 Multibody system simulation: deformation of beam axis, cross section forces and torques
6 Recovery of stress and deformation inside the cross sections

FIG. 82: Workflow proposal for a rotor blade analysis from 3D CAD modeling via automated beam model generation, multibody system analysis, and recovery of deformation and stress

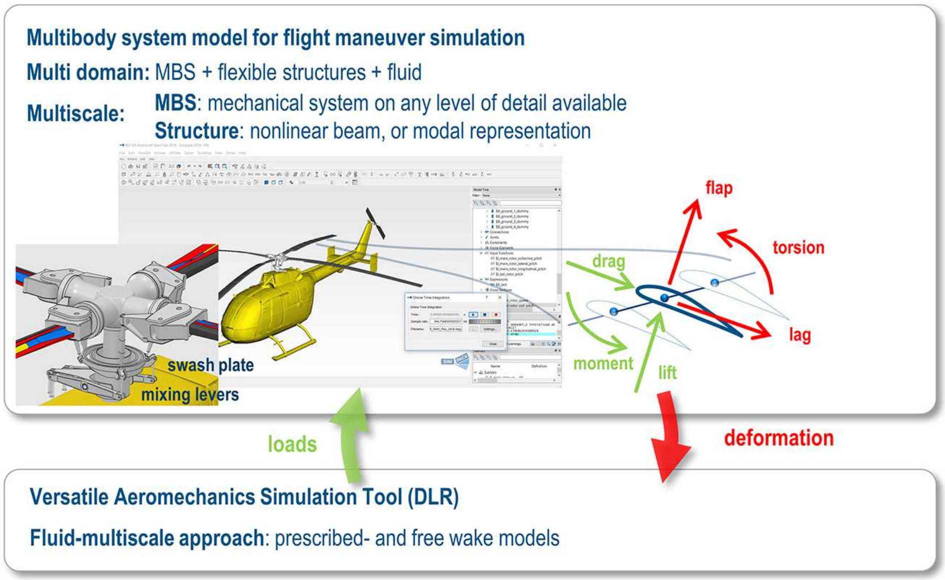
Multibody system model for flight maneuver simulation
Multi domain: MBS + flexible structures + fluid
Multiscale: MBS: mechanical system on any level of detail available
Structure: nonlinear beam, or modal representation
swash plate
mixing levers
flap
torsion
drag
lag
moment
lift
loads
deformation
Versatile Aeromechanics Simulation Tool (DLR)
Fluid-multiscale approach: prescribed- and free wake models

FIG. 83: Multibody system model coupled with the aeromechanics code VAST of the DLR for flight maneuver simulation

The German Federal Ministry for Economic Affairs and Energy funded the work presented in this section under support code 20H1506. The responsibility for the content of this section lies with the authors.

5.3 Battery Porous Electrode Theory Models

Li-Ion batteries are at the core of the worldwide impetus on electrification that is prevalent in many industries, particularly in automotive and high tech. For engineering purposes, the typical battery cell construction (Fig. 84) involves scales from the submicron level as associated with active particles in anodes/cathodes, connected up to tens of millimeters (or even a meter) as associated with the entire cell. Predictive simulation methods (Abaqus, 2021) solve effectively and accurately the concurrent scales problem by employing a FE^2 method rooted in the porous electrode theory (Newman and Thomas-Alyea, 2004).

The multiscale/multiphysics nature of the problem is described succinctly in Fig. 85. There are several material multiscale aspects that require simultaneous solution: (1) A diffusion in solid particles (assumed spherical) at microscale on particles with characteristic dimensions from 0.1 to 20 μm. This diffusion models intercalation/de-intercalation cycles and it is associated with solid phase transformations that have a significant influence on the nonlinearity of the diffusion coeffcients and the overall mechanical swelling of the particles; (2) reactive electrochemistry at the wetted particle surface coupling the macroscale electrochemistry involving electric potentials and concentration

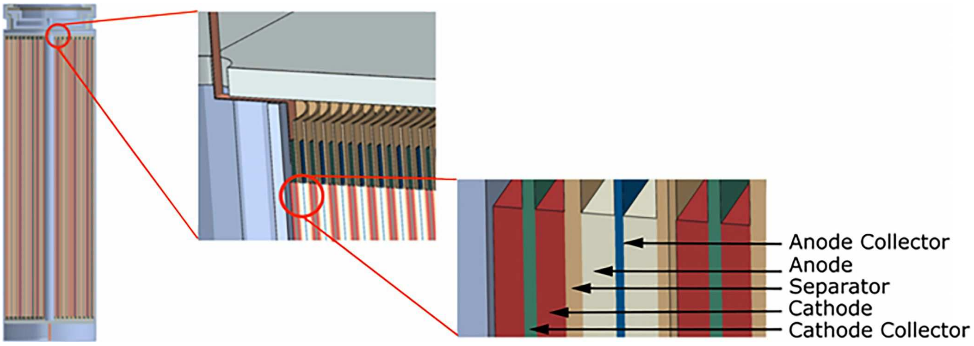
Anode Collector
Anode
Separator
Cathode
Cathode Collector

FIG. 84: Li-Ion battery cells—a prime example of multiscale behavior. From 0.1 m to 1 μm by the nature of the manufacturing process and reactive powders included (Abaqus, 2021).

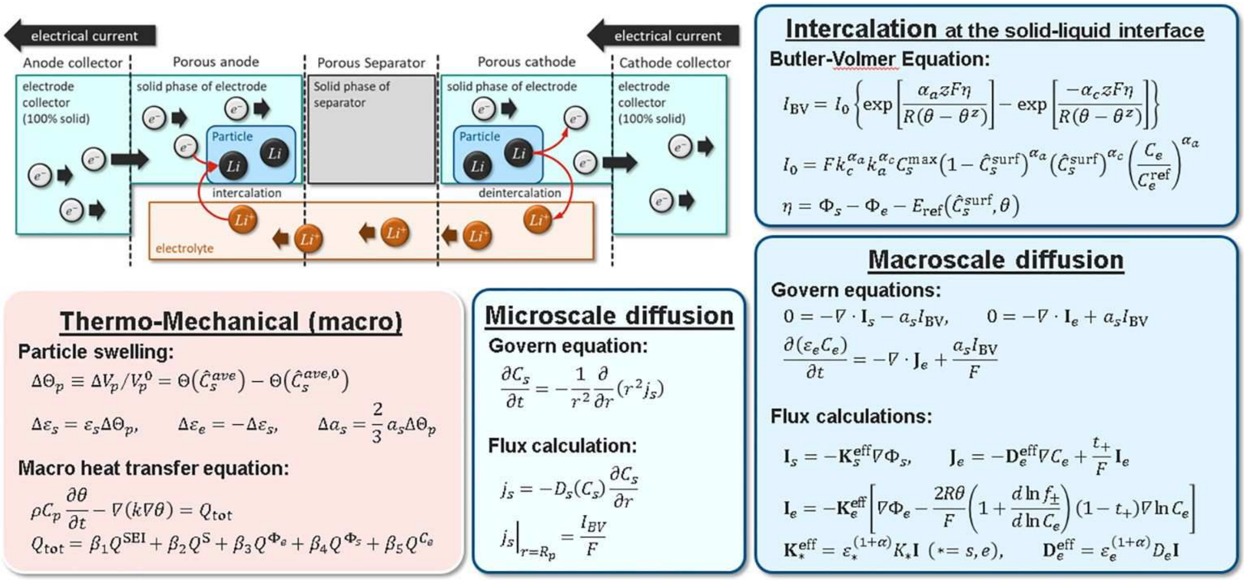
electrical current
electrical current
Anode collector
Porous anode
Porous Separator
Porous cathode
Cathode collector
electrode collector (100% solid)
solid phase of electrode
Solid phase of separator
solid phase of electrode
electrode collector (100% solid)
e^-
Particle
Li
Li
Particle
Li
Li
intercalation
deintercalation
Li^+
electrolyte
Intercalation at the solid-liquid interface
Butler-Volmer Equation:
$I_{\mathrm{BV}} = I_0 \left\{ \exp\left[\frac{\alpha_a zF\eta}{R(\theta-\theta^z)}\right] - \exp\left[\frac{-\alpha_c zF\eta}{R(\theta-\theta^z)}\right] \right\}$
$I_0 = F k_c^{\alpha_a} k_a^{\alpha_c} C_s^{\max}\left(1-\hat{C}_s^{\mathrm{surf}}\right)^{\alpha_a}\left(\hat{C}_s^{\mathrm{surf}}\right)^{\alpha_c}\left(\frac{C_e}{C_e^{\mathrm{ref}}}\right)^{\alpha_a}$
$\eta = \Phi_s - \Phi_e - E_{\mathrm{ref}}\left(\hat{C}_s^{\mathrm{surf}}, \theta\right)$
Macroscale diffusion
Govern equations:
$0 = -\nabla \cdot \mathbf{I}_s - a_s I_{\mathrm{BV}}, \qquad 0 = -\nabla \cdot \mathbf{I}_e + a_s I_{\mathrm{BV}}$
$\frac{\partial(\varepsilon_e C_e)}{\partial t} = -\nabla \cdot \mathbf{J}_e + \frac{a_s I_{\mathrm{BV}}}{F}$
Flux calculations:
$\mathbf{I}_s = -\mathbf{K}_s^{\mathrm{eff}} \nabla \Phi_s, \qquad \mathbf{J}_e = -\mathbf{D}_e^{\mathrm{eff}} \nabla C_e + \frac{t_+}{F}\mathbf{I}_e$
$\mathbf{I}_e = -\mathbf{K}_e^{\mathrm{eff}}\left[\nabla\Phi_e - \frac{2R\theta}{F}\left(1+\frac{d\ln f_\pm}{d\ln C_e}\right)(1-t_+)\nabla \ln C_e\right]$
$\mathbf{K}_*^{\mathrm{eff}} = \varepsilon_*^{(1+\alpha)} K_* \mathbf{I} \ (* = s, e), \qquad \mathbf{D}_e^{\mathrm{eff}} = \varepsilon_e^{(1+\alpha)} D_e \mathbf{I}$
Thermo-Mechanical (macro)
Particle swelling:
$\Delta\Theta_p \equiv \Delta V_p / V_p^0 = \Theta\left(\hat{C}_s^{ave}\right) - \Theta\left(\hat{C}_s^{ave,0}\right)$
$\Delta\varepsilon_s = \varepsilon_s \Delta\Theta_p, \qquad \Delta\varepsilon_e = -\Delta\varepsilon_s, \qquad \Delta a_s = \frac{2}{3} a_s \Delta\Theta_p$
Macro heat transfer equation:
$\rho C_p \frac{\partial\theta}{\partial t} - \nabla(k\nabla\theta) = Q_{\mathrm{tot}}$
$Q_{\mathrm{tot}} = \beta_1 Q^{\mathrm{SEI}} + \beta_2 Q^{\mathrm{S}} + \beta_3 Q^{\Phi_e} + \beta_4 Q^{\Phi_s} + \beta_5 Q^{C_e}$
Microscale diffusion
Govern equation:
$\frac{\partial C_s}{\partial t} = -\frac{1}{r^2}\frac{\partial}{\partial r}(r^2 j_s)$
Flux calculation:
$j_s = -D_s(C_s)\frac{\partial C_s}{\partial r}$
$j_s\big|_{r=R_p} = \frac{I_{BV}}{F}$

FIG. 85: Li-Ion battery cells—a schematic representation illustrated in a charge scenario (top left). Governing equations in fully coupled thermo-electrochemistry-mechanical involve scales involving five orders of magnitude requiering FE^2 solver technology (Abaqus, 2021).

in the electrolyte to a de-homogenized flux driving the intercalation/de-intercalation process; (3) a multiphysics homogenization method to impose the overall conservation of Li to realize the interplay between the different scales. Swelling at particle level drives overall deformation of the electrodes/cell leading to evolutions of the macroscale porosities and tortuosities which in turn affect the overall macroscale diffusion. Some results, Li diffusion/migration, and electron conduction schematics are illustrated in Fig. 86.

The need for increased energy densities in battery cells is driving a lot of research worlwide. One such direction involves Si-based anodes which hold the potential of increasing stored capacity multiple-fold with incredible potential benefits to engineering applications (e.g., increased driving range in automobiles). However, the lithiation process in Si is accompanied by a very large volumetric swelling and stress development (Kumar et al., 2017) which leads to premature degradation in usual charge/discharge cycles. Discrete element methods combined with finite elements techniques as illustrated in Fig. 87 can provide additional insights in behavior at the submicron scale.

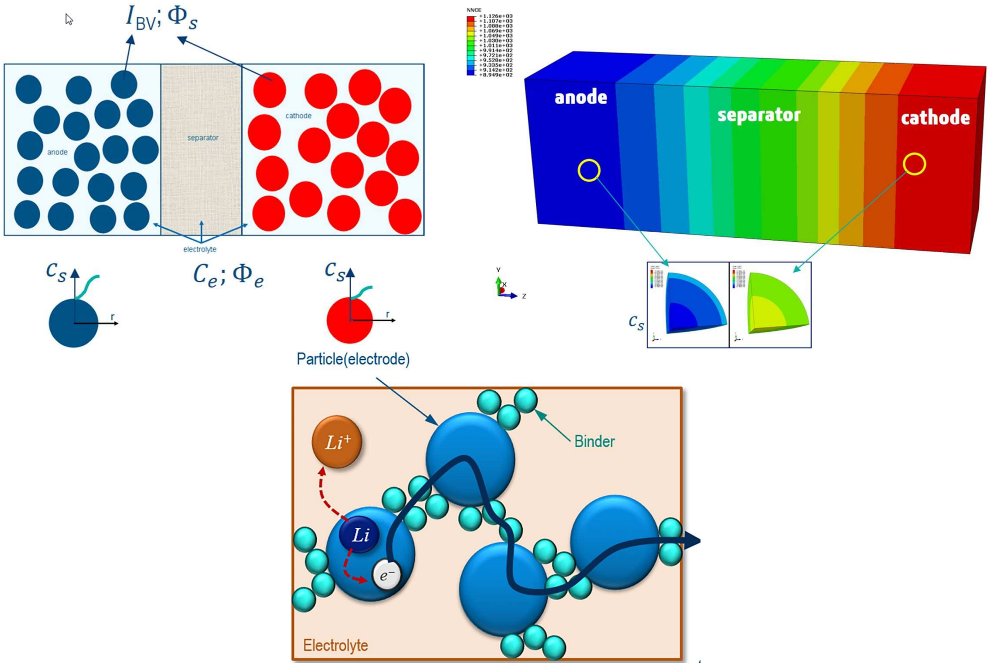

FIG. 86: Li-Ion battery cells—a schematic representation illustrating the field variables being solved in a multiscale FE^2 sense; sample results for Li-Ion concentration in the electrolyte (cell scale) and particles at microscale (top right); cartoon representation of a tortuous path of travel of Li-Ion and electrons follow in a functional battery (Abaqus, 2021)

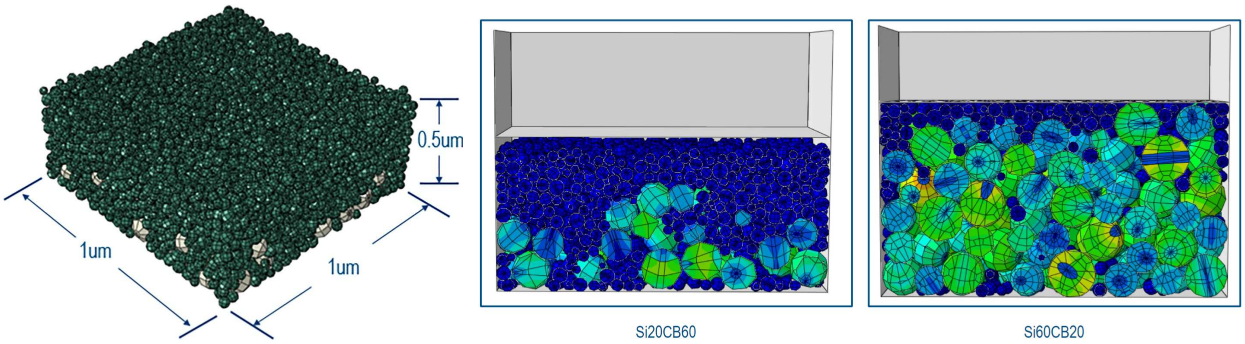

Si20CB60

Si60CB20

FIG. 87: Pseudo-manufacturing model of active anode particles (left); lithiation model for various weight fractions Si, and graphite mixtures illustrating one of the grand challenges of Si-based anodes architectures—large swelling leading to reduced battery life

5.4 Battery Electrolyte Characterization: From Atoms to Cells

In this case on liquid battery electrolytes, we create a direct and complete in silico link between the chemical formulation (e.g., the recipe) of an electrolyte solution and the overall performance of the battery cell. Current commercial electrolytes are typically based on a carbonate solvent with $\mathrm{LiPF_6}$ acting as a salt and a range of different additives (Ecker et al., 2015a,b). These additives play an important role in the battery performance and in controlling degradation, for example, to avoid formation of toxic HF (Okuno et al., 2016), help form the solid electrolyte interphase (SEI) (Han et al., 2015), or to provide chemical protection against overcharging (Buhrmester et al., 2005), among many other uses. The key challenge with these additives is that all components of the electrolyte composition also affect its charge transport performance and are intrinsically linked to the overall battery cell performance. The formulation of electrolytes therefore is a multiobjective optimization required for each cell chemistry. At the same time, it is done relatively late in the materials development cycle and on time scales much shorter than the multiple years typically required to design and scale up other battery materials such as a new cathode or anode chemistry.

This multiobjective optimization problem is a prototypical use case for multiscale modeling. Validated molecular modeling workflows make it possible to screen different additive candidates for chemical properties. For example, BIOVIA Materials Studio (2021) has been used extensively to compute the electrochemical stability of many different candidates (Halls and Tasaki, 2009). To enable the multiobjective study of the electrolyte with a direct link to the overall battery cell performance, it is essential to establish a direct link between the electrolyte formulation and charge/discharge curves of complete battery cells. This section summarizes the multiscale connection introduced in detail by Hanke et al. (2020), with a focus on the different methods used to obtain the charge transport properties of Li-Ion solutions for different concentrations and temperatures.

With molecular scales, we begin by translating the solvent formulation into numbers of molecules from which we can build a simulation cell using the Monte Carlo based Amorphous Cell Module in Materials Studio (Akkermans et al., 2013). The key ingredients are provided as mass ratio of ethylene carbonate (EC, molecular weight 88.1 g/mol) and ethyl methyl carbonate (EMC, molecular weight 104.1 g/mol). We also add varying pairs of $\mathrm{Li^+}$ and $\mathrm{PF_6^-}$ ions into the cell to account for the concentration dependence. We found it sufficient to use approximately 200 molecules in total. For each simulation cell, an initial MD simulation is run for 100 ps using an NPT ensemble (e.g., keeping the number of molecules constant, and applying a barostat to apply a constant pressure of 0 and a thermostat to keep a constant temperature) with the COMPASS suite of force fields in Materials Studio (Sun et al., 2016; Akkermans et al., 2020). This calculation will provide the density of the solution, from which we can calculate the concentration c (in mol/l) of the salt solution—an essential parameter for the Newman model simulations.

To obtain the charge transport parameters, we continue with a longer 5 ns MD simulation in an NVE ensemble (constant number of molecules, volume, and total energy). The diffusion $D_\pm$ coefficient for an individual ionic species is calculated by averaging the mean square displacements $\Delta R^2(t)$ of the ions over time and applying the long-time random walk relation, $\lim_{t\to\infty}\left\langle \Delta R^2(t)\right\rangle = 6Dt$. The angled brackets denote the average over all ion displacements and time intervals available in a MD trajectory. The partial conductivity for individual ionic species is now calculated using the diffusion coefficient and the Einstein relation $\kappa_\pm = D_\pm c e^2 N_A / k_B T$; here e is the charge of an electron, N_A is Avogadro's number, and k_B the Boltzmann constant. The overall conductivity is calculated by summing partial conductivities over all ion species. The transference number for Li-Ions is obtained from the relative contribution of Li to the conductivity, e.g., $t_+ = D_+/(D_+ + D_-)$.

So far, we covered a single simulation cell for a single temperature at a single concentration value. The full parameterization of an electrolyte requires averaging over several different simulation cells for each c/T pair and then repeating the entire analysis over several different concentrations and temperatures. Finally, the global results are fit into a single-model parameterization representing the electrolyte. The entire workflow is detailed in Hanke et al. (2020). To achieve all of these calculations, it is imperative to automate the calculations as much as possible, done here using protocols in BIOVIA Pipeline Pilot (2021) which allows users to go directly from the number of molecules to the final electrolyte transport relations in a single-user interaction. At the same time, it is essential to keep track of important simulation details, for example, to allow users to track the statistics. This information must be available both on the level of an individual trajectory and for the global calculation of the temperature- and concentration-dependent charge transport properties. Figures 88(a)–88(d) summarize the results of the workflow so far.

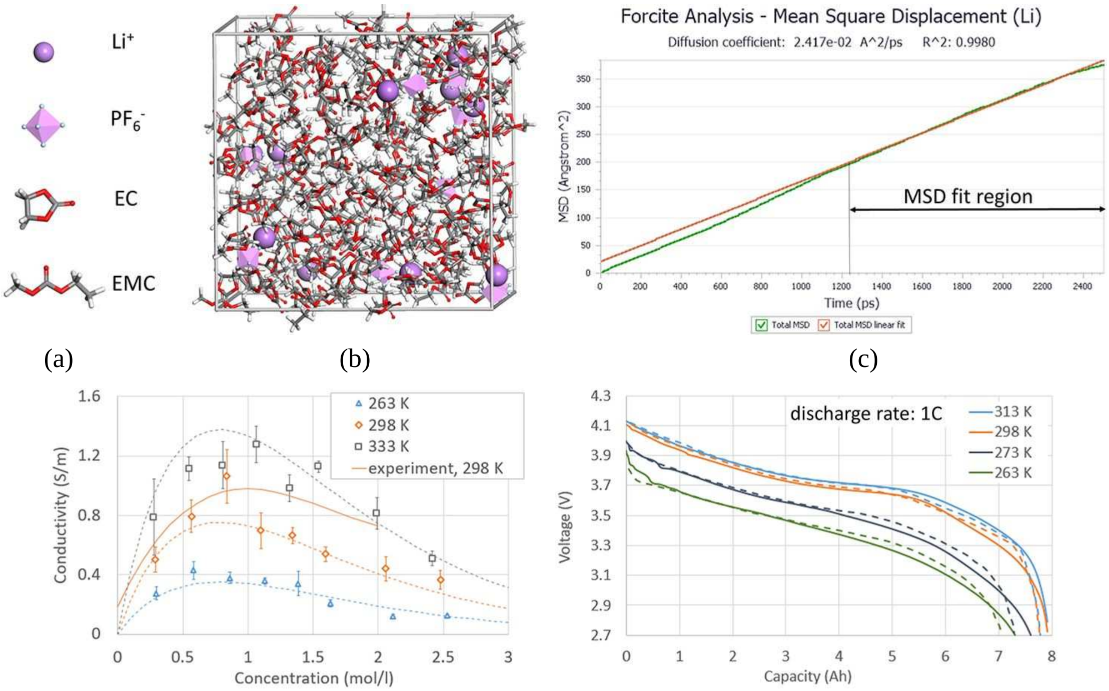

(a) (b) (c)

(d) (e)

FIG. 88: Linking the motion of individual Li-Ions to battery cell performance

At this stage, we have obtained the charge transport properties for a liquid electrolyte directly from its formulation using only molecular dynamics simulations. We can now use the resulting charge transport model in our Newman model implementation in the Dymola battery library or in Abaqus as described previously, with the remaining parameters of the Newman model taken from existing measurements by Ecker et al. (2015a). The results of this calculation are shown in Fig. 88(e) and show quantitative agreement with measured battery cell performance data for a discharge rate of 1 C (e.g., complete discharge of the cell in 1 hr) and for different temperatures. The same approach provides quantitative agreement with measured voltage traces for both fast charging and at low temperature.

Overall, this multiscale workflow enables the multiobjective in silico design and optimization of electrolytes for a number of different chemical characteristics as well as charge transport properties. This is particularly important for controlling long-time degradation of the battery, which is to a large extent controlled by the (electro-) chemical behavior of individual electrolyte molecules. While improving the longevity of the electrolyte, it remains essential to optimize the charge transport properties of the battery as well.

6. MACHINE LEARNING

There is no doubt that machine learning is infiltrating into many fields of study as a promising technology. In the field of multiscale materials modeling, machine learning approaches are gaining popularity to extract constitutive laws from lower-scale computations as well as to construct surrogate models for efficient calculation of microstructure responses. For example, Rocha et al. (2021) used an active learning framework to accelerate concurrent multiscale (FE^2) analysis. The framework was concluded promising to reduce the computational cost of FE^2 with limitations such as being unable to handle nonmonotonic strain paths. Machine learning can also be employed for computational materials design ensembling computational techniques spanning quantum chemistry, molecular dynamics to continuum scale. Mortazavi et al. (2020) used machine learning to model interatomic potentials enabling first-principles multiscale modeling where no viable classical modeling alternative is available. Despite many publications, machine learning in the multiscale material modeling faces challenges. While providing accurate prediction within the training data range, the model may become unconstrained and inaccurate outside the training data regime. Machine learning needs big data and it is difficult to transform the current physical testing system to keep up with the thirst for data. It is difficult to include added complexity such as nonmonotonic loading and history dependence, and to extract physically meaningful quantities to infer the material state. This section presents a few numerical examples focusing on how to train a proper machine learning model to tackle some of the above challenges.

6.1 ANN Approach for Hyperelastic Material Modeling with Stability Constraint and Extrapolation Capability

We use a multilayer perceptron ANN to model the strain-energy potential with respect to the strain invariants. The inputs are the strain invariants I_1, I_2; the output is the strain-energy potential U (Fig. 89). The neural net connects the inputs to hidden layer/layers and then to the output layer through activation functions. Experimental measurements or virtual simulations can be used to create the training database. In this case, the uniaxial, biaxial, and planar test data are used to train the machine learning model. The weights and biases of the neurons are optimized through the training of the network driven by the data and a multilayer function can be extracted from the trained neural network. Due to the high flexibility of the neural network, it is mostly guaranteed that the mathematical model matches very well with the test data. However, out of the range of available data, the response may become unconstrained and unstable. Proper selection of the activation function based on physics could improve the extrapolation capability of the trained machine learning potential. In this case, since the stress is the derivative of the potential with respect to the strain, in order to improve numerical stability, the derivative of the activation function with respect to strain should monotonically increase as strain increases. Therefore, the softplus activation function is a better choice in this case as compared to a tanh activation function. Another approach to constrain the machine learning function is to use physical constraint as added terms in the loss function. In this example, we added a Drucker stability constraint based error function as a weighted term in the loss function. We are able to improve the stable range of the trained hyperelastic model with a minimal loss in the accuracy of the model (Table 1).

A different approach is to train the machine learning model to correct the error between the test data and the best fitting conventional material model, e.g., Ogden3. A Gaussian activation function is used for the neural network and trained to correct localized errors of the best fitting Ogden3 model within the test data range. The hybrid model approaches the behavior of the Ogden3 as strain moves out of the test data range. This approach guarantees best fitting between test data and model within a given data range and well understood numerical stability for out of range strains, e.g., unconditionally stable in this case (Fig. 90).

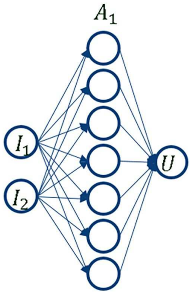

FIG. 89: Basic structure of a multilayer perceptron model

TABLE 1: Stable nominal strain ranges (based on Du et al., 2021)

Stable Strain Range	Without Constraint	With Constraint
Uniaxial	(–0.26, ∞)	(–0.38, ∞)
Biaxial	(–1, 0.051)	(–1, 0.5)
Planar	(–0.28, 0.38)	(–1, ∞)

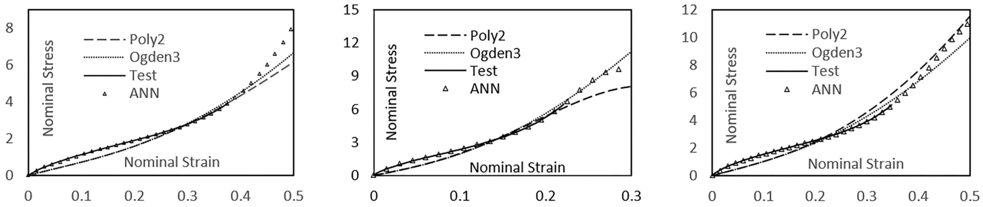

FIG. 90: Nominal stress vs. nominal strain of the hybrid model (based on Du et al., 2021)

6.2 Recurrent Neural Network Approach for Anisotropic Plastic Material Modeling with History Dependence

We use the gated recurrent unit (GRU) followed by a regular ANN to include the history dependence of anisotropic plastic materials. Virtual simulations can be performed in batches for a large number (750 simulations in this case) of load cases with random loadings and unloadings. The stress and strain histories can be extracted and used as the training data. The inputs to the GRU are all past histories of strains. The GRU extracts from the past strain data the controlling history variables $h_{<t-1>}$, updates them to the current state $h_{<t>}$, and feeds into the subsequent ANN layers for regression modeling (Fig. 91).

The method is applicable to data generated by virtual experiment/microstructure simulations for scale bridging. However, in order to validate the predictiveness of the RNN approach, we used Abaqus 2D Hill plasticity and 3D Barlat plasticity as virtual data/ground truth. Figure 92 shows good matching between ground truth simulations using the built-in Hill plasticity model and machine learning predictions for four new unseen loading histories. Figure 93 shows good matching between ground truth simulations using the built-in Barlat plasticity model and machine learning predictions for two new unseen loading histories.

These models are implemented into Abaqus through the UMAT and/or VUMAT subroutine interface. The trained machine learning models are rewritten in the material routines for stress update at the material point, providing the exact same accuracy in FE simulations as external ML testing, and they do not exhibit issues such as error accumulation as found in some incremental forms of machine learning approaches. These models can be applied to any datasets including datasets obtained from running RVE simulations for multiscale material modeling. Nevertheless, the above studies have a heavy focus on machine learning practice, skipping the microstructural simulation and virtual data generation steps, and merely serve as numerical examples to show a few ideas on how to tackle some of the common challenges in using machine learning for a multiscale material model. Other challenges such as errors in discontinuous function machine learning predictions, machine learning error mitigation, or physical measure extraction for the material state may be tacked with hybrid/physics informed approaches (Bi et al., 2021; Vlassis and Sun, 2021).

7. TOWARDS STREAMLINING MATERIAL MULTISCALE IN ENGINEERING PRACTICE

The **3D**EXPERIENCE Platform is a collaborative environment that connects designers and engineers in real time. Users leverage the latest data whenever and wherever needed, increasing collaboration and improving productivity. Everything including the processes, the data, and the applications can be shared by all stakeholders in a secured

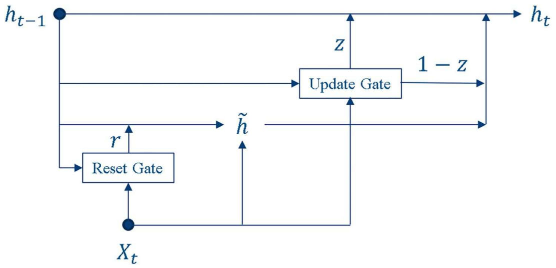

FIG. 91: Basic structure of a GRU model

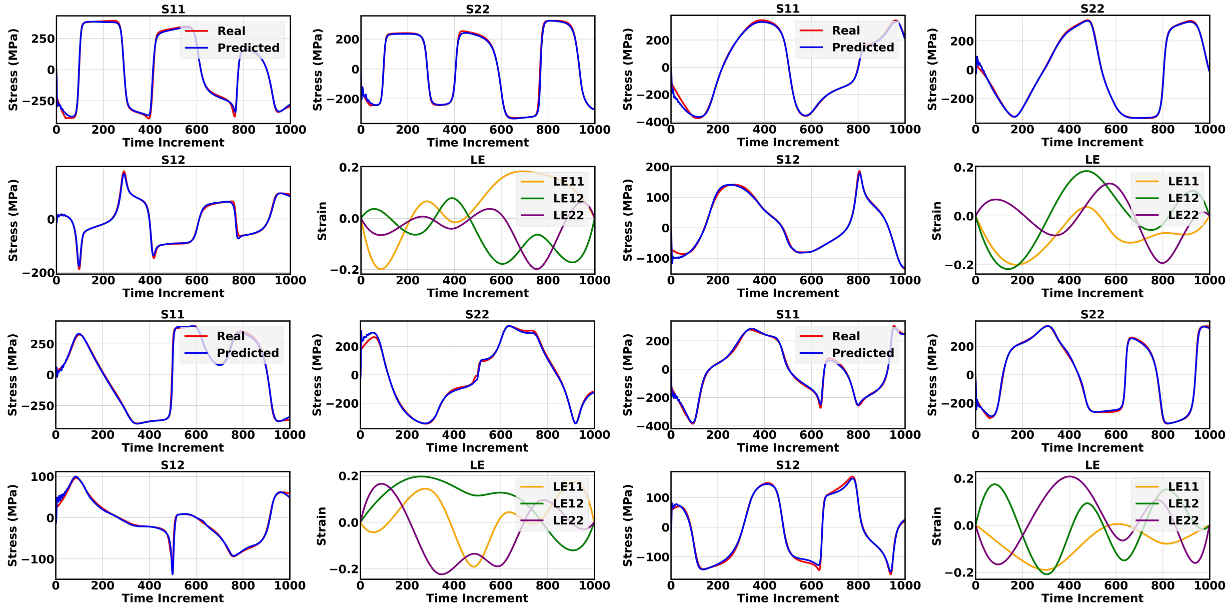

FIG. 92: ML predictions (blue) vs. virtual experiments (red) for unseen loadings, validation with 2D Hill (based on Bi et al., 2021)

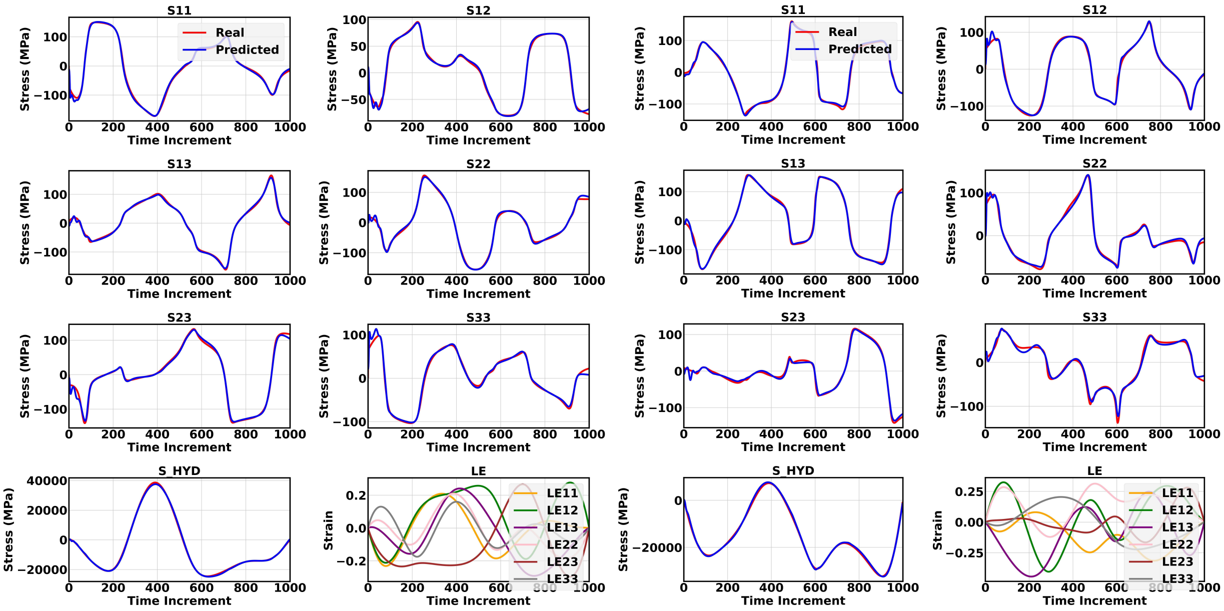

FIG. 93: ML predictions (blue) vs. virtual experiments (red) for unseen loadings, validation with 3D Barlat (based on Bi et al., 2021)

environment. The **3D**EXPERIENCE Platform enables all participants to view and test the product or service at any stage as they can be experienced virtually. This offers the advantage of being able to make cost-effective changes quickly and at any time.

The **3D**EXPERIENCE Platform portfolio comprises 3D modeling applications, simulation applications, social and collaborative applications, and IT applications, which enables a streamlined workflow that connects material designers with simulation engineers of different expertise and also the manufacturers.

Next we demonstrate the streamlined workflow on the platform with the example of an end-to-end process designing an injection molded part with fiber-reinforced composite as shown in Fig. 94. The Plastic Part Design app can be used by a plastic part designer for the initial design of the CAD geometry. Once the design is complete, the part is published on the platform; the plastic injection engineer can then access the part on the platform and start their injection molding simulation in the Plastic Injection app. Design parameters such as the gate locations can be optimized by an optimization process using the Results Analytics app. Geometry changes may also be recommended by plastic injection engineers and can be directly reviewed and approved by the designers in real time on the platform. In the meantime structural engineers can have access to the current version of the CAD design and create a simulation to test the integrity of the part design and fiber distributions from the injection molding simulation. A customized process can be used to connect the plastic injection simulation to the structural simulation, in which results mapping is done automatically during the import of the results fields including fiber orientation, temperature, and residual stresses. The entire process from part design to structural simulation can be automated using an execution process and optimal design parameters can be identified and reviewed by all participants of the project.

8. CONCLUSIONS

Inventing a new material is truly “rocket science.” The creative process is driven by brilliant minds working together often from multiple domains leveraging vastly different science and engineering skills. Most commonly the resulting work is subject to protective patents regarding the “secrete sauce” behind the recipe. Corporations of all kinds consider materials development as one of the core assets as far as Intellectual Property is concerned. For that matter public domain dissemination of best practices, numerical modeling included, does often not reflect entirely the state of a “production”-related simulation tool chain in an enterprise. This paper is no exception.

There is no doubt that ICME/materials science computational methods often come to the aid of the material scientist/engineer to complement physical testing/measurements/prototyping for accelerated timelines of product development. Some of the techniques are reserved for the dedicated scientist/researcher in advanced research labs, and others represent core tools used in consulting companies or dedicated departments in industrial corporations, while others have permeated routine engineering practice.

While we cannot really share most of the interesting applications we have been working on with our customers, perhaps the description of the methods and applications that we could share can help the reader form an opinion

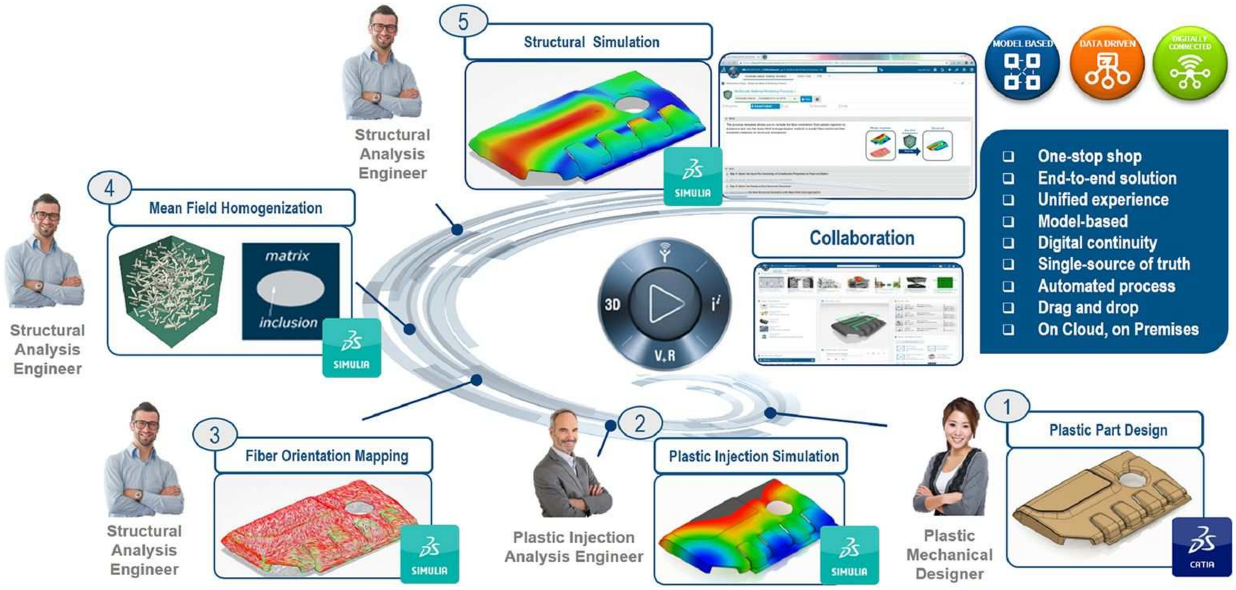
5
Structural Simulation
Structural Analysis Engineer
SIMULIA
MODEL BASED
DATA DRIVEN
DIGITALLY CONNECTED
❑ One-stop shop
❑ End-to-end solution
❑ Unified experience
❑ Model-based
❑ Digital continuity
❑ Single-source of truth
❑ Automated process
❑ Drag and drop
❑ On Cloud, on Premises
4
Mean Field Homogenization
matrix
inclusion
SIMULIA
Structural Analysis Engineer
Collaboration
3D
V,R
i
3
Fiber Orientation Mapping
SIMULIA
Structural Analysis Engineer
2
Plastic Injection Simulation
SIMULIA
Plastic Injection Analysis Engineer
1
Plastic Part Design
CATIA
Plastic Mechanical Designer

FIG. 94: End-to-end digital thread for maximized process automation

of the overall offering. At Dassault Systèmes the effort on providing advanced, customizable, flexible, and easy to use simulation tools to help the materials engineer/scientist has been sustained with new advancements with each release. We embarked on this journey years ago offering commercial solutions at all scales starting from *ab initio* to product. We are committed to advancing existing tools and to creating new ones to extend the penetration of advanced multiscale methods in daily engineering practice.

REFERENCES

Abaqus, Abaqus User Documentation, Johnston, RI: Dassault Systèmes SIMULIA, 2021.

Akkermans, R.L.C., Spenley, N.A., and Robertson, S.H., Monte Carlo Methods in Materials Studio, *Mol. Simul.*, vol. **39**, nos. 14-15, pp. 1153–1164, 2013.

Akkermans, R.L.C., Spenley, N.A., and Robertson, S.H., COMPASS III: Automated Fitting Workflows and Extension to Ionic Liquids, *Mol. Simul.*, vol. **47**, no. 7, pp. 540–551, 2020.

Al-Khalil, M., Kirtil, E., and Rigby, R., Use of Abaqus Explicit for Composite Sandwich Damage Prediction during Bird Impact, in *Proc. of SIMULIA Community Conf.*, 2015.

Baillargeon, B., Rebelo, N., Fox, D.D., Taylor, R.L., and Kuhl, E., The Living Heart Project: A Robust and Integrative Simulator for Human Heart Function, *Eur. J. Mech., A: Solids*, vol. **48**, pp. 38–47, 2014.

Balasubramani, S.G., Chen, G.P., Coriani, S., Diedenhofen, M., Frank, M.S., Franzke, Y.J., Furche, F., Grotjahn, R., Harding, M.E., Hättig, C., Hellweg, A., Helmich-Paris, B., Holzer, C., Huniar, U., Kaupp, M., Khah, A.M., Khani, S.K., Müller, T., Mack, F., Nguyen, B.D., Parker, S.M., Perlt, E., Rappoport, D., Reiter, K., Roy, S., Rückert, M., Schmitz, G., Sierka, M., Tapavicza, E., Tew, D.P., van Wüllen, C., Voora, V.K., Weigend, F., Wodynski, A., and Yu, J.M., TURBOMOLE: Modular Program Suite for Ab Initio Quantum-Chemical and Condensed-Matter Simulations, *J. Chem. Phys.*, vol. **152**, no. 18, p. 184107, 2020.

Ballard, M.K., McLendon, W.R., and Whitcomb, J.D., The Influence of Microstructure Randomness on Prediction of Fiber Properties in Composites, *J. Compos. Mater.*, vol. **48**, no. 29, pp. 3605–3620, 2014.

Bannan, C.C., Burley, K.H., Chiu, M., Shirts, M.R., Gilson, M.K., and Mobley, D.L., Blind Prediction of Cyclohexane-Water Distribution Coefficients from the SAMPL5 Challenge, *J. Comput.-Aided Mol. Des.*, vol. **30**, no. 11, pp. 927–944, 2016.

Bargmann, S., Klusemann, B., Markmann, J., Schnabel, J.E., Schneider, K., Soyarslan, C., and Wilmers, J., Generation of 3D Representative Volume Elements for Heterogeneous Materials: A Review, *Prog. Mater. Sci.*, vol. **96**, pp. 322–384, 2018.

Bergstrom, J.S. and Bischoff, J.E., An Advanced Thermomechanical Constitutive Model for UHMWPE, *Int. J. Struct. Changes Solids*, vol. **2**, pp. 31–39, 2010.

Bi, J., Gao, Z., and Oancea, V., Artificial Neural Network and Recurrent Neural Network Approaches for Isotropic and Anisotropic Plastic Material Modeling, in *Mechanistic Machine Learning and Digital Twins for Computational Science, Engineering & Technology, an IACM Conf.*, San Diego, CA, September 26–29, 2021.

Bi, J., Tripathy, S., Savane, V., and Kumar, A., Multiscale Infill/Lattice Optimization Using RVE, *Science in the Age of Experience*, Boston, MA, May 23–26, 2016.

BIOVIA COSMOtherm 2021, Copyright Dassault Systèmes, 2021.

BIOVIA Materials Studio 2021, Copyright Dassault Systèmes, 2021.

BIOVIA Pipeline Pilot 2021, Copyright Dassault Systèmes, 2021.

Billiar, K.L. and Sacks, M.S., A Method to Quantify the Fiber Kinematics of Planar Tissues under Biaxial Stretch, *J. Biomech.*, vol. **30**, no. 7, pp. 753–756, 1997.

Bittermann, K., Spycher, S., Endo, S., Pohler, L., Huniar, U., Goss, K.U., and Klamt, A., Prediction of Phospholipid-Water Partition Coefficients of Ionic Organic Chemicals Using the Mechanistic Model COSMOmic, *J. Phys. Chem. B*, vol. **118**, pp. 14833–14842, 2014.

Bittermann, K., Linden, L., and Goss, K.U., Screening Tools for the Bioconcentration Potential of Monovalent Organic Ions in Fish, *Environ. Sci.: Processes Impacts*, vol. **20**, no. 5, pp. 845–853, 2018.

Boyce, M.C., Kear, K., Socrate, S., and Shaw, K., Deformation of Thermoplastic Vulcanizates, *J. Mech. Phys. Solids*, vol. **49**, no. 5, pp. 1073–1098, 2001.

Boyce, B.L., Kramer, S.L.B., and Xue, L., The Second Sandia Fracture Challenge: Predictions of Ductile Failure under Quasi-Static and Moderate-Rate Dynamic Loading, *Int. J. Fract.*, vol. **198**, pp. 5–100, 2016.

Buhrmester, C., Chen, J., Moshurchak, L., Jiang, J., Wang, R.L., and Dahn, J., Studies of Aromatic Redox Shuttle Additives for $LiFePO_4$-Based Li-Ion Cells, *J. Electrochem. Soc.*, vol. **152**, p. A2390, 2005.

Burke, K., Perspective on Density Functional Theory, *J. Chem. Phys.*, vol. **136**, p. 150901, 2012.

Chen, C., Depa, P., Sakai, V.G., Maranas, J.K., Lynn, J.W., Peral, I., and Copley, J.R.D., A Comparison of United Atom, Explicit Atom, and Coarse-Grained Simulation Models for Poly(ethylene oxide), *J. Chem. Phys.*, vol. **124**, p. 234901, 2006.

Choi, J., Shin, H., and Cho, H., A Multiscale Mechanical Model for the Effective Interphase of SWNT/Expoxy Nanocomposite, *Polymer*, vol. **89**, pp. 159–171, 2016.

Clark, S.J., Segall, M.D., Pickard, C.J., Hasnip, P.J., Probert, M.J., Refson, K., and Payne, M.C., First Principles Methods Using CASTEP, *Z. Kristall*, vol. **220**, pp. 567–570, 2005.

CMH-17 Meeting Results, in *6th CMH-17 Crashworthiness Working Group Meeting*, Ottawa, Canada, August 5, 2008.

Delley, B., An All-Electron Numerical Method for Solving the Local Density Functional for Polyatomic Molecules, *J. Phys. Chem.*, vol. **92**, p. 508, 1990.

Delley, B., DMol3 DFT Studies: From Molecules and Molecular Environments to Surfaces and Solids, *Comput. Mater. Sci.*, vol. **17**, pp. 122–126, 2000.

Djordjevic, A.R., Biljie, R.M., Likar-Smiljanic, V.D., and Sarkar, T.K., Wideband Frequency-Domain Characterization of FR-4 and Time-Domain Causality, *IEEE Trans. Electromagn. Compat.*, vol. **43**, no. 4, pp. 662–667, 2001.

Du, H., Bi, J., Oancea, V., van der Velden, A., Cojocaru, D., Wohlever, C., and Hurtado, J., Artificial Neural Network Approach for Hyperelastic Material Modeling with Stability Constraint and Extrapolation Capability, in *Proc. of Mechanistic Machine Learning and Digital Twins for Computational Science, Engineering & Technology*, San Diego, CA, September 26–29, 2021.

Ecker, M., Tran, T.K.D., Dechent, P., Käbitz, S., Warnecke, A., and Sauer, D.U., Parameterization of a Physico-Chemical Model of a Lithium-Ion Battery. I. Determination of Parameters, *J. Electrochem. Soc.*, vol. **162**, p. A1836, 2015a.

Ecker, M., Käbitz, S., Laresgoiti, I., and Sauer, D.U., Parameterization of a Physico-Chemical Model of a Lithium-Ion Battery. II. Model Validation, *J. Electrochem. Soc.*, vol. **162**, p. A1849, 2015b.

Endo, S., Bauerfeind, J., and Goss, K.U., Partitioning of Neutral Organic Compounds to Structural Proteins, *Environ. Sci. Technol.*, vol. **46**, no. 22, pp. 12697–12703, 2012.

Fager, A., Otomo, H., Salazar-Tio, R., Balasubramanian, G., Crouse, B., Zhang, R., Chen, H., and Schembre-McCabe, J., Multi-Scale Digital Rock: Application of a Multi-Scale Multi-Phase Workflow to a Carbonate Reservoir Rock, in *Proc. of The Society of Core Analysis Conf. SCA2021-U004*, 2021.

Fermemglia, M. and Prici, S., Multiscale Molecular Modeling in Nanostructured Material Design and Process, *Comput. Chem. Eng.*, vol. **33**, no. 10, pp. 1701–1710, 2009.

Fish, J., *Practical Multiscaling*, New York: John Wiley & Sons, Ltd., 2014.

Fish, J. and Ghouli, A., Multiscale Analytical Sensitivity Analysis for Composite Materials, *Int. J. Numer. Methods Eng.*, vol. **50**, pp. 1501–1520, 2001.

Fish, J. and Yuan, Z., Multiscale Enrichment Based on the Partition of Unity, *Int. J. Numer. Methods Eng.*, vol. **62**, no. 10, pp. 1341–1359, 2005.

Fish, J. and Yuan, Z., Multiscale Enrichment Based on Partition of Unity for Nonperiodic Fields and Nonlinear Problems, *Comput. Mech.*, vol. **40**, pp. 249–259, 2007.

Flanigan, C.M., Beyer, L., Klekamp, D., Rohweder, D., Stuck, B., and Terrill, E.R., Comparative Study of Silica, Carbon Black and Novel Fillers in Tread Compounds, in *Proc. of 180th Technical Meeting of the Rubber Division of the American Chemical Society, Inc.*, Cleveland, OH, October 11–13, 2011.

Gale, J.D. and Rohl, A.L., The General Utility Lattice Program, *Mol. Simul.*, vol. **29**, pp. 291–341, 2003.

Gasser, T.C., Ogden, R.W., and Holzapfel, G.A., Hyperelastic Modelling of Arterial Layers with Distributed Collagen Fiber Orientations, *J. R. Soc. Interface*, vol. **3**, pp. 15–35, 2006.

Geers, M.G.D., Kouznetsova, V.G., Matouš, K., and Yvonnet, J., Homogenization Methods and Multiscale Modeling: Nonlinear Problems, in *Encyclopedia of Computational Mechanics*, 2nd ed., 2017.

Geisler, A., Oemisch, L., Endo, S., and Goss, K.U., Predicting Storage-Lipid Water Partitioning of Organic Solutes from Molecular Structure, *Environ. Sci. Technol.*, vol. **49**, no. 9, pp. 5538–5545, 2015.

Glahn, T., Chiavaccini, E., and Schuhmann, R., FIT-TD Simulation of Non-Linear Materials for Second Harmonic Generation in

Periodically Poled Lithiumniobate Waveguides, in *Proc. of 2011 Int. Conf. on Electromagnetics in Advanced Applications*, pp. 27–30, 2011.

Gold, G. and Helmreich, K., A Physical Surface Roughness Model and Its Applications, *IEEE Trans. Microwave Theory Tech.*, vol. **65**, no. 10, pp. 3720–3732, 2017.

Gouskos, D. and Iannucci, L., Finite Element Analysis of Non-Crimp Fabric Laminates under Compact Tension, in *Proc. of ECCM18—18th European Conf. on Composite Materials*, Athens, Greece, June 24–28, 2018.

Govindarajan, S.M., Hurtado, J.A., and Mars, W.V., Simulation of Mullins Effect and Permanent Set in Filled Elastomers Using Multiplicative Decomposition, in *Proc. of the 5th European Conf. on Constitutive Models for Rubber, ECCMR, 2007*, Paris, France, September 2007, vol. **5**, 2008.

Groot, R.D. and Warren, P.B., Dissipative Particle Dynamics: Bridging the Gap between Atomistic and Mesoscopic Simulation, *J. Chem. Phys.*, vol. **107**, pp. 4423–4435, 1997.

Grujicic, M., Bell, W.C., Pandurangan, B., and He, T., Blast-Wave Impact-Mitigation Capability of Polyurea when Used as Helmet Suspension-Pad Material, *Mater. Des.*, vol. **31**, no. 9, pp. 4050–4065, 2010.

Grujicic, M., Pandurangan, B., King, A.E., Runt, J., Tarter, J., and Dillon, G., Multi-Length Scale Modeling and Analysis of Microstructure Evolution and Mechanical Properties in Polyurea, *J. Mater. Sci.*, vol. **46**, no. 6, pp. 1767–1779, 2011.

Halls, M. and Tasaki, K., High-Throughput Quantum Chemistry and Virtual Screening for Lithium Ion Battery Electrolyte Additives, *J. Power Sources*, vol. **195**, pp. 1472–1478, 2010.

Hammerstad, E.O. and Jensen, Ø., Accurate Models for Microstrip Computer Aided Design, *IEEE MTT-S Int. Microwave Symp. Dig.*, pp. 407–409, 1980.

Han, Y.K., Yoo, J., and Yim, T., Why is Tris(trimethylsilyl) Phosphate Effective as an Additive for High-Voltage Lithium-Ion Batteries?, *J. Mater. Chem. A*, vol. **3**, p. 10900, 2015.

Han, S. and Bauchau, O.A., Nonlinear Three-Dimensional Beam Theory for Flexible Multibody Dynamics, *Multibody Syst. Dyn.*, vol. **34**, no. 3, pp. 211–242, 2015.

Hanke, F., Modrow, N., Akkermans, R.L.C., Korotkin, I., Mocanu, F.C., Neufeld, V.A., and Veit, M., Multi-Scale Electrolyte Transport Simulations for Lithium Ion Batteries, *J. Electrochem. Soc.*, vol. **167**, p. 013522, 2020.

Hashin, Z., Analysis of Composite Materials—A Survey, *J. Appl. Mech.*, vol. **50**, pp. 481–505, 1983.

Hill, R., Elastic Properties of Reinforced Solids: Some Theoretical Principles, *J. Mech. Phys. Solids*, vol. **11**, no. 5, pp. 357–372, 1963.

Hohenberg, P. and Kohn, W., Inhomogeneous Electron Gas, *Phys. Rev.*, vol. **136**, p. B864, 1964.

Holzapfel, G.A., Gasser, T.C., and Ogden, R.W., A New Constitutive Framework for Arterial Wall Mechanics and a Comparative Study of Material Models, *J. Elasticity*, vol. **61**, pp. 1–48, 2000.

Holzapfel, G.A. and Ogden, R.W., Constitutive Modelling of Passive Myocardium: A Structurally Based Framework for Material Characterization, *Philos. Trans.*, vol. **367**, no. 1902, pp. 3445–3475, 2009.

Huang, J. and MacKerell, A.D., Jr., CHARMM36 All-Atom Additive Protein Force Field: Validation Based on Comparison to NMR Data, *J. Comput. Chem.*, vol. **34**, no. 25, pp. 2135–2145, 2013.

Huray, P.G., *The Foundations of Signal Integrity*, Hoboken, NJ: John Wiley & Sons, Inc., 2009.

Hurtado, J.A., Lapczyk, I., and Govindarajan, S.M., Parallel Rheological Framework to Model Non-Linear Viscoelasticity, Permanent Set, and Mullins Effect in Elastomers, *Const. Models Rubber*, vol. **8**, pp. 95–100, 2013.

Jerauld, G.R., Fredrich, J., Lane, N., Sheng, Q., Crouse, B., Freed, D.M., Fager, A., and Xu, R., Validation of a Workflow for Digitally Measuring Relative Permeability, in *Proc. of Abu Dhabi Int. Petroleum Exhibition and Conf.*, Dallas, TX: Society of Petroleum Engineers, p. SPE-188688-MS, 2017.

Ji, H., McLendon, R., Hurtado, J.A., Oancea, V., and Bi, J., Multi-Scale Material Modeling with the Mean-Field Homogenization Method, *NAFEMS World Congress 2017*, Stockholm, Sweden, June 11–13, 2017.

Johnson, A.F., Modelling Fabric-Reinforced Composites under Impact Loads, *Composites, Part A*, vol. **32**, no. 9, pp. 1197–1206, 2001.

Joshi, S.Y. and Deshmukh, S.A., A Review of Advancements in Coarse-Grained Molecular Dynamics Simulations, *Mol. Simul.*, vol. **47**, nos. 10-11, pp. 786–803, 2021.

Jung, J., Nishima, W., Daniels, M., Bascom, G., Kobayashi, C., Adedoyin, A., Wall, M., Lappala, A., Phillips, D., Fischer, W., Tung, C.S., Schlick, T., Sugita, Y., and Sanbonmatsu, K.Y., *J. Comput. Chem.*, vol. **40**, pp. 1919–1930, 2019.

Kaddour, A.S. and Hinton, M.J., Maturity of 3D Failure Criteria for Fiber-Reinforced Composites: Comparsion between Theories and Experiments: Part B of WWFE-II, *J. Compos. Mater.*, vol. **47**, nos. 6-7, pp. 925–966, 2013.

Karkkainen, R.L., Sankar, B.V., and Tzeng, J.T., A Direct Micromechanical Approach toward the Development of Quadratic Stress Gradient Failure Criteria for Textile Composites, *J. Compos. Mater.*, vol. **41**, no. 16, pp. 1917–1937, 2007.

Kaul, V., Yao, J., and Hurtado, J.A., A Microstructural Anisotropic Hyperelastic Material for Soft Tissues, in *Proc. of 7th World Congress of Biomechanics*, 2014.

Klamt, A. and Schüürmann, G., COSMO: A New Approach to Dielectric Screening in Solvents with Explicit Expressions for the Screening Energy and Its Gradient, *J. Chem. Soc., Perkin Trans. 2*, vol. **1993**, no. 5, pp. 799–805, 1993.

Klamt, A., Jonas, V., Bürger, T., and Lohrenz, J.C., Refinement and Parametrization of COSMO-RS, *J. Phys. Chem. A*, vol. **102**, pp. 5074–5085, 1998.

Klamt, A., Krooshof, G.J.P., and Taylor, R., COSMOSPACE: Alternative to Conventional Activity-Coefficient Models, *AIChE J.*, vol. **48**, no. 10, pp. 2332–2349, 2002.

Klamt, A., Huniar, U., Spycher, S., and Keldenich, J., COSMOmic: A Mechanistic Approach to the Calculation of Membrane-Water Partition Coefficients and Internal Distributions within Membranes and Micelles, *J. Phys. Chem. B*, vol. **112**, no. 38, pp. 12148–12157, 2008.

Klamt, A., Schwöbel, J.A.H., Huniar, U., Koch, L., Terzi, S., and Gaudin, T., COSMOplex: Self-Consistent Simulation of Self-Organizing Inhomogeneous Systems Based on COSMO-RS, *Phys. Chem. Chem. Phys.*, vol. **21**, no. 18, pp. 9225–9238, 2019.

Klusemann, B. and Svendsen, B., Homogenization Methods for Multi-Phase Elastic Composites: Comparisons and Benchmarks, *Technische Mechanik*, vol. **30**, no. 4, pp. 374–386, 2010.

Kohn, W. and Sham, L.J., Self-Consistent Equations Including Exchange and Correlation Effects, *Phys. Rev.*, vol. **140**, p. A1133, 1965.

Kumar, R., HaWoo, J., Xiao, X., and Sheldon, B.W., Internal Microstructural Changes and Stress Evolution in Silicon Nanoparticle Based Composite Electrodes, *J. Electrochem. Soc.*, vol. **164**, no. 14A, pp. 3750–3765, 2017.

Lanir, Y., Constitutive Equations for Fibrous Connective Tissues, *J. Biomech.*, vol. **16**, no. 1, pp. 1–2, 1983.

Li, A., Li, R., and Fish, J., Generalized Mathematical Homogenization: From Theory to Practice, *Comput. Methods Appl. Mech. Eng.*, vol. **197**, nos. 41-42, pp. 245–269, 2008.

Li, H., O'Hara, P., and Duarte, C.A., Non-Intrusive Coupling of a 3-D Generalized Finite Element Method and Abaqus for the Multiscale Analysis of Localized Defects and Structural Features, *Finite Elem. Anal. Des.*, vol. **193**, p. 103554, 2021.

Lu, Y., Jin, W., Klinger, J., Westover, T.L., and Dai, S., Flow Characterization of Compressible Biomass Particles Using Multiscale Experiments and a Hypoplastic Model, *Powder Technol.*, vol. **383**, pp. 396–409, 2021.

Lundborg, M., Narangifard, A., Wennberg, C.L., Lindahl, E., Daneholt, B., and Norlén, L., Human Skin Barrier Structure and Function Analyzed by Cryo-EM and Molecular Dynamics Simulation, *J. Struct. Biology*, vol. **203**, no. 2, pp. 149–161, 2018.

Marrink, S.J., de Vries, A.H., and Mark, A.E., Coarse Grained Model for Semiquantitative Lipid Simulations, *J. Phys. Chem. B*, vol. **108**, pp. 750–760, 2004.

Martin, R., *Electronic Structure, Basic Theory and Practical Methods*, Cambridge: Cambridge University Press, 2012.

Mazhnik, E. and Oganov, A.R., A Model of Hardness and Fracture Toughness of Solids, *J. Appl. Phys.*, vol. **126**, p. 125109, 2019.

Mechin, P.Y., Keryvin, V., Grandidier, J.-C., and Glehen, D., An Experimental Protocol to Measure the Parameters Affecting the Compressive Strength of CFRP with a Fibre Micro-Buckling Failure Criterion, *Compos. Struct.*, vol. **211**, pp. 154–162, 2019.

Mechin, P.Y., Keryvin, V., and Grandidier, J.C., Limitations on Adding Nano-Fillers to Increase the Compressive Strength of Continuous Fibre/Epoxy Matrix Composites, *Compos. Sci. Technol.*, vol. **192**, p. 108099, 2020.

Mesarovic, S.D. and Padbidri, J., Minimal Kinematic Boundary Conditions for Simulations of Disordered Microstructures, *Philos. Mag.*, vol. **85**, no. 1, pp. 65–78, 2005.

McLendon, W.R., Micromechanics Plugin for Abaqus, from https://www.linkedin.com/pulse/micromechanics-plugin-abaqus-ross-mclendon/, 2017.

McLendon, W.R., Bi, J., Kulkarni, S., Matos, M., Deng, J., Cojocaru, D., and Ji, H., Predicting Lattice Response and Stability Using Finite Element RVE Analysis, in *Proc. of NAFEMS Multiscale and Multiphysics Modeling & Simulation*, Columbus, OH, March, 2017.

McLendon, R., Cojocaru, D., Dalrymple, T., Spirka, T., and Young, P., Calibration of a Phenomenological Foam Material Model from Microscale Simulation, in *Proc. of NAFEMS World Congress 2019*, Quebec City, Quebec, Canada, 2019.

McLendon, W.R. and Whitcomb, J.D., Characteristic Failure Initiation Sites in Plain Weave Textile Composites, *J. Compos. Mater.*, vol. **47**, no. 25, pp. 3143–3161, 2013.

McLendon, W.R. and Whitcomb, J.D., Influence of Thermally Induced Microstress and Microstructural Randomness on Transverse Strength of Unidirectional Composites, *J. Compos. Mater.*, vol. **50**, no. 11, pp. 1467–1481, 2016.

Mindt, M., Dietz, S., Schulze, M., and Mabou, H., Simulation of the Free Flying Helicopter by Coupling of a New Comprehensive Aeromechanics Code with an Advanced Flexible Multibody Model, in *Proc. of Vertical Flight Society 75th Annual Forum & Technology Display*, Philadelphia, PA, May 2019.

Moreira, J., Tsai, M., Kenton, J., Barnes, H., and Faller, D., PCB Loadboard Design Challenges for Multi-Gigabit Devices, *Autom. Test Appl.*, vol. **3**, pp. 1749–1776, 2006.

Mortazavi, B., Podryabinkin, E., Roche, S., Rabczuk, T., Zhuang, X., and Shapeev, A., Machine-Learning Interatomic Potentials Enable First-Principles Multiscale Modeling of Lattice Thermal Conductivity in Graphene/Borophene Heterostructures, *Mater. Horiz.*, vol. **7**, pp. 2359–2367, 2020.

Mullins, L., and Tobin, N.R., Theoretical Model for the Elastic Behavior of Filler-Reinforced Vulcanized Rubber, *Rubber Chem. Technol.*, vol. **30**, no. 2, pp. 555–571, 1957.

Newman, J. and Thomas-Alyea, K.E., *Electrochemical Systems*, Hoboken, NJ: Wiley-Interscience, 2004.

Nguyen, V.P., Stroeven, M., and Sluys, L.J., Multiscale Continuous and Discontinuous Modeling of Heterogeneous Materials: A Review on Recent Developments, *J. Multiscale Modell.*, vol. **3**, no. 4, pp. 229–270, 2011.

Oancea, V., Dalrymple, T., Ji, H., Bi, J., Tripathy, S., Wescott, J., and Todd, S., Multi-Scale Simulations for Material Modeling, in *Proc. of SPE Automotive Composites Conf. & Exhibition (ACCE)*, Novi, MI, June 20, 2016.

Oancea, V., Dalrymple, T., Ji, H., Bi, J., Tripathy, S., Wescott, J., and Todd, S., Bridging between Molecular to Component Scales in Multiscale Material Modeling, in *Proc. of NAFEMS Multiscale and Multiphysics Modeling & Simulation*, Columbus, OH, March, 2017.

Okuno, Y., Ushirogata, K., Sodeyama, K., and Tateyama, Y., Decomposition of the Fluoroethylene Carbonate Additive and the Glue Effect of Lithium Fluoride Products for the Solid Electrolyte Interphase: An Ab Initio Study, *Phys. Chem. Chem. Phys.*, vol. **18**, p. 8643, 2016.

Omairey, S.L., Dunning, P.D., and Sriramula, S., Development of an Abaqus Plugin Tool for Periodic RVE Homogenization, *Eng. Comput.*, vol. **35**, no. 2, pp. 567–577, 2019.

OpenPhase Microstructure Simulation, from http://openphase-solutions.com/, 2021.

Oskay, C. and Fish, J., Eigendeformation-Based Reduced Order Homogenization for Failure Analysis of Heterogeneous Materials, *Comput. Methods Appl. Mech. Eng.*, vol. **196**, no. 7, pp. 1216–1243, 2007.

Oskay, C. and Fish, J., On Calibration and Validation of Eigendeformation-Based Multiscale Models for Failure Analysis of Heterogeneous Systems, *Comput. Mech.*, vol. **42**, no. 2, pp. 181–195, 2008.

Otomo, H., Chen, H., and Zhang, R., An Under-Resolved-Simulation Approach for Multi-Component Fluid Flows in Multi-Scale Porous Structures (to be published), 2021.

Park, H., Choi, J., Kim, B., and Cho, M., Temperature-Accelerated Molecular Dynamics Simulations of Quasi-Static Yield Stress of Epoxy Polymers, in *Proc. of 2018 AIAA/ASCE/AHS/ASC Structures, Structural Dynamics, and Materials Conference*, 2018.

Park, H. and Cho, M., Multiscale Constitutive Model Using Data-Driven Yield Function, *Composites, Part B*, vol. **216**, p. 108831, 2021.

Perdew, J.P. and Schmidt, K., Jacob's Ladder of Density Functional Approximations for the Exchange-Correlation Energy, *AIP Conf. Proc.*, vol. **577**, p. 1, 2001.

Phelan, D., Reid, M., and Dippenaar, R., Kinetics of the Peritectic Reaction in an Fe–C Alloy, *Mater. Sci. Eng.: A*, vol. **477**, nos. 1-2, pp. 226–232, 2008.

Pinho, S.T., Darvizeh, R., Robinson, P., Schuecker, C., and Camanho, P.P., Material and Structural Response of Polymer-Matrix Fiber-Reinforced Composites, *J. Compos. Mater.*, vol. **46**, nos. 19-20, pp. 2313–2341, 2012.

Qi, H.J. and Boyce, M.C., Constitutive Model for Stretch-Induced Softening of the Stress–Stretch Behavior of Elastomeric Materials, *J. Mech. Phys. Solids*, vol. **52**, no. 10, pp. 2187–2205, 2004.

Qi, H.J. and Boyce, M.C., Stress-Strain Behavior of Thermoplastic Polyurethanes, *Mech. Mater.*, vol. **37**, no. 8, pp. 817–839, 2005.

Qin, S., McLendon, R., Oancea, V., and Beese, A., Micromechanics of Multiaxial Plasticity of DP600: Experiments and Microstructural Deformation Modeling, *Mater. Sci. Eng., A*, vol. **721**, pp. 168–178, 2018.

Reuss, A., Berechnung der Fließgrenze von Mischkristallen auf Grund der Plastizitätsbedingung für Einkristalle, *J. Appl. Math. Mech.*, vol. **9**, no. 1, pp. 49–58, 1929.

Rocha, I., Kerfriden, P., and van der Meer, F., On-the-Fly Construction of Surrogate Constitutive Models for Concurrent Multiscale Mechanical Analysis through Probabilistic Machine Learning, *J. Comput. Phys.: X*, vol. **9**, p. 100083, 2021.

Saavedra Flores, E.I., Adhikari, S., Friswell, M.I., and Scarpa, F., Hyperelastic Finite Element Model for Single Wall Carbon Nanotubes in Tension, *Comput. Mater. Sci.*, vol. **50**, no. 3, pp. 1083–1087, 2011.

Sacks, M.S., Incorporation of Experimentally-Derived Fiber Orientation into a Structural Constitutive Model for Planar Collagenous Tissues, *J. Biomech. Eng.*, vol. **125**, no. 2, pp. 280–287, 2003.

Saeb, S., Steinmann, P., and Javili, A., Aspects of Computational Homogenization at Finite Deformations: A Unifying Review from Reuss' to Voigt's Bound, *Appl. Mech. Rev.*, vol. **68**, no. 5, p. 050801, 2016.

Sahli Costabal, F., Yao, J., and Kuhl, E., Predicting Drug-Induced Arrhythmias by Multiscale Modeling, *Int. J. Numer. Methods Biomed. Eng.*, vol. **34**, no. 5, p. e2964, 2018.

Schrader, S., Modeling Thermoplastic Vulcanizate Seals with Abaqus, Abaqus Users Conference, May 2005.

Schwöbel, J.A.H. and Klamt, A., Mechanistic Skin Penetration Model by the COSMOperm Method: Routes of Permeation, Vehicle Effects and Skin Variations in the Healthy and Compromised Skin, *Comput. Toxicol.*, vol. **11**, pp. 50–64, 2019.

Schwöbel, J.A.H., Ebert, A., Bittermann, K., Huniar, U., Goss, K.U., and Klamt, A., COSMOperm: Mechanistic Prediction of Passive Membrane Permeability for Neutral Compounds and Ions and Its pH Dependence, *J. Phys. Chem. B*, vol. **124**, no. 16, pp. 3343–3354, 2020.

Shlepnev, Y. and McMorrow, S., Nickel Characterization for Interconnect Analysis, in *Proc. of 2011 IEEE Int. Symp. on Electromagnetic Compatability*, pp. 524–529, 2011.

Shi, M.X., Li, Q.M., Liu, B., Feng, X.Q., and Huang, Y., Atomic-Scale Finite Element Analysis of Vibration Mode Transformation in Carbon Nanorings and Single-Walled Carbon Nanotubes, *Int. J. Solids Struct.*, vol. **46**, nos. 25-26, pp. 4342–4360, 2009.

Skylaris, C.K., Mostofi, A.A., Haynes, P.D., Dieguez, O., and Payne, M.C., Nonorthogonal Generalized Wannier Function Pseudopotential Plane-Wave Method, *Phys. Rev. B*, vol. **66**, p. 035119, 2002.

Sokolinsky, V.S., Indermuehle, K.C., and Hurtado, J.A., Numerical Simulation of the Crushing Process of a Corrugated Composite Plate, *Composites, Part A*, vol. **42**, no. 9, pp. 1119–1126, 2011.

Souza, P.C.T., Alessandri, R., Barnoud, J., Thallmair, S., Faustino, I., Grünewald, F., Patmanidis, I., Abdizadeh, H., Bruininks, B.M.H., Wassenaar, T.A., Kroon, P.C., Melcr, J., Nieto, V., Corradi, V., Khan, H.M., Domañski, J., Javanainen, M., Martinez-Seara, H., Reuter, N., Best, R.B., Vattulainen, I., Monticelli, L., Periole, X., Tieleman, D.P., de Vries, A.H., and Marrink, S.J., Martini 3: A General Purpose Force Field for Coarse-Grained Molecular Dynamics, *Nat. Methods*, vol. **18**, pp. 382–388, 2021.

Steinbach, I. and Apel, M., Multi Phase Field Model for Solid State Transformation with Elastic Strain, *Phys. D (Amsterdam, Neth.)*, vol. **217**, no. 2, pp. 153–160, 2006.

Sun, H., Jin, Z., Yang, C., Akkermans, R.L.C., Robertson, S.H., Spenley, N.A., Miller, S., and Todd, S.M., COMPASS II: Extended Coverage for Polymer and Drug-Like Molecule Databases, *J. Mol. Model.*, vol. **22** , p. 47, 2016.

Sun, W., Guan, Z., Li, Z., Zhang, M., and Huang, Y., Compressive Failure Analysis of Unidirectional Carbon/Epoxy Composite Based on Micro-Mechanical Models., *Chin. J. Aeronaut.*, vol. **30**, no. 6, pp. 1907–1918, 2017.

Svensson, C. and Dermer, G.H., Time Domain Modeling of Lossy Interconnects, *IEEE Trans. Adv. Packag.*, vol. **24**, no. 2, pp. 191–196, May 2001.

Tao, Y. and Scharf, F., Revisit Nickel Characterization Effect on High-Speed Interconnect Performance, in *Proc. of 2015 IEEE MTT-S Int. Conf. on Numerical Electromagnetic and Multiphysics Modeling and Optimization (NEMO)*, pp. 1–3, 2015.

Taylor, G.I., Plastic Strain in Metals, *J. Inst. Met.*, vol. **62**, pp. 307–324, 1938.

Tiaden, J., Phase Field Simulations of the Peritectic Solidification of Fe–C, *J. Cryst. Growth*, vols. **198–199**, no. 2, pp. 1275–1280, 1999.

Tian, Y., Xu, B., and Zhao, Z., Microscopic Theory of Hardness and Design of Novel Superhard Crystals, *Int. J. Refract. Met. Hard Mater.*, vol. **33**, pp. 93–106, 2012.

TURBOMOLE V7.5, A Development of University of Karlsruhe and Forschungszentrum Karlsruhe GmbH, 1989–2007, TURBOMOLE GmbH, since 2007, from https://www.turbomole.org and https://www.3ds.com, 2020.

van de Walle, A., Asta, M., and Ceder, G., The Alloy Theoretic Automated Toolkit: A User Guide, *CALPHAD: Comput. Coupling Phase Diagrams Thermochem.*, vol. **26**, no. 4, pp. 539–553, 2002a.

van de Walle, A. and Ceder, G., Automating First-Principles Phase Diagram Calculations, *J. Phase Equilib.*, vol. **23**, no. 348, 2002b.

van de Walle, A., Sun, R., Hong, Q.J., and Kadkhodaei, S., Software Tools for High-Throughput CALPHAD from First-Principles Data, *CALPHAD: Comput. Coupling Phase Diagrams Thermochem.*, vol. **58**, pp. 70–81, 2017.

Vlassis, N.N. and Sun, W.C., Sobolev Training of Thermodynamic-Informed Neural Networks for Interpretable Elasto-Plasticity Models with Level Set Hardening, *Comput. Methods Appl. Mech. Eng.*, vol. **377**, p. 113695, 2021.

Voigt, W., *Lehrbuch der Krystallphysik*, Leipzig, Germany: Teubner, 1928.

Waldman, S.D., Sacks, M.S., and Lee, J.M., Boundary Conditions during Biaxial Testing of Planar Connective Tissues. Part II. Fiber Orientation, *J. Mater. Sci. Lett.*, vol. **21**, no. 15, pp. 1215–1221, 2002.

Wang, Y. and McDowell, D.L., *Uncertainty Quantification in Multiscale Materials Modeling*, Cambridge: Woodhead Publishing, 2020.

Whelan, G. and McDowell, D.L., Uncertainty Quantification in ICME Workflows for Fatigue Critical Computational Modeling, *Eng. Fract. Mech.*, vol. **220**, p. 106673, 2019.

Yan, H., Li, X., Chandra, B., Tulevski, G., Wu, Y., Freitag, M., Zhu, W., Avouris, P., and Xia, F., Tunable Infrared Plasmonic Devices Using Graphene/Insulator Stacks, *Nat. Nanotechnol.*, vol. **7**, pp. 330–334, 2012.

Yi, J., Boyce, M.C., Lee, G.F., and Balizer, E., Large Deformation Rate-Dependent Stress–Strain Behavior of Polyurea and Polyurethanes, *Polymer*, vol. **47**, no. 1, pp. 319–329, 2006.

Yuan, Z. and Fish, J., Are the Cohesive Zone Models Necessary for Delamination Analysis?, *Comput. Methods Appl. Mech. Eng.*, vol. **310**, pp. 567–604, 2016.

Zhang, J., Tuguldur, B., and van der Spoel, D., Force Field Benchmark of Organic Liquids. 2. Gibbs Energy of Solvation, *J. Chem. Inf. Model.*, vol. **55**, no. 6, pp. 1192–1201, 2015.

Zhang, Q., Xie, J., Gao, Z., London, T., Griffiths, D., and Oancea, V., A Metallurgical Phase Transformation Framework Applied to SLM Additive Manufacturing Processes, *Mater. Des.*, vol. **166**, p. 107618, 2019a.

Zhang, Q., Xie, J., London, T., Griffiths, D., Bhamji, I., and Oancea, V., Estimates of the Mechanical Properties of Laser Powder Bed Fusion Ti-6Al-4V Parts Using Finite Element Models, *Mater. Des.*, vol. **169**, p. 107678, 2019b.

Zhang, M., Salazar-Tio, R., Fager, A., and Crouse, B., A Multiscale Digital Rock Workflow for Shale Matrix Permeability Prediction, in *Proc. of Unconventional Resources Technology Conference (URTeC)*, 2020.